Fabrication and Characterisation of III-Nitride based Nanostructure Devices using Nanosphere Lithography Techniques

Modestos Athanasiou

A Thesis Submitted for the Degree of Doctor of Philosophy (Ph.D.) in the Department of Electronic and Electrical Engineering

Abstract

In this work, fabrication and characterisation of nanostructure devices has been performed on InGaN/GaN multiple quantum wells (MQW) grown on either c-plane sapphire or (111) silicon substrates. A cost effective nanosphere lithography technique has been employed for the fabrication of a number of nano structures such as nanorod arrays, nanoholes arrays; and single micro-disk lasers. Photonic crystal structures based on nanohole arrays have been designed and then fabricated on InGaN/GaN MQWs with an emission wavelength of 500 nm grown on c-plane sapphire by means of a nanosphere lithography technique, demonstrating a clear photonic crystal effect.

Significant suppression of spontaneous emission has been observed when the emission is within the photonic bandgap. Angular dependent measurements show a change in the far-field pattern when the emission lies outside the photonic bandgap compared with the emission which lies inside the photonic bandgap.

A coherent nanocavity a two-dimensional (2D) periodic array of nanodisks, was designed and fabricated on an InGaN/GaN MQW structure with an emission wavelength at 510 nm, leading to a significant enhancement in the internal quantum efficiency (IQE) as a result of enhanced spontaneous emission rate. Finite-difference time-domain (FDTD) analysis has performed for the structure design. The coherent nanocavity effect has been confirmed using means of time-resolved photoluminescence measurements, showing a clear enhancement in spontaneous emission rate. Finally, an improvement in IQE of 88 times at 510 nm has been achieved.

Optically pumped green lasing has been achieved with thresholds as low as 1 kW/cm^2, using an InGaN/GaN based micro-disk with an undercut structure on silicon substrates. The micro-disks with a diameter of around 1 µm were fabricated by means of a combination of a cost-effective silica micro-sphere

approach, dry-etching and subsequent a wet-etching. The combination of these techniques both minimises the roughness of the sidewalls of the micro-disks and also produces excellent circular geometry. Utilizing this fabrication process, lasing has been achieved at room temperature under optical pumping from a continuous-wave laser diode. Time–resolved micro-photoluminescence (PL) and confocal PL measurements have been performed in order to further confirm the lasing action in whispering gallery modes and also investigate the excitonic recombination dynamics of the lasing.

Acknowledgements

I would like to take this opportunity to thank the many people who have helped me in completing my project. First of all, I would like to thank my supervisor Professor Tao Wang for giving me the opportunity to explore the world of III-Nitrides and for his support and guidance throughout my Ph.D. Secondly, I am very grateful to Dr Jie Bai for teaching me how to use the equipment to fabricate my devices in the initial stages of my Ph.D.

Additionally, I would like to thank Dr Taeki Kim, with whom I spent many hours with in the cleanroom trying to optimise silica nanosphere deposition. Also I am very grateful to Dr Richard Smith and Dr Bin Liu, with whom I spent many hours in the optical characterisation lab and in the office discussing and designing optical experiments. Furthermore, I would like to thank all of the members of our research group: Dr Yipin Gong, Mr Kun Xing, Mr Yu Xiang, Mr Benbo Xu and Mr Jonathan Benton for their help and for the discussions we had during my Ph.D. Additionally I would to thank all of the technical staff of National Centre, especially: Dr Ken Kennedy, Mr Saurabh Kumar and Dr Rob Airey. I would especially like to thank Mr Paul Haines and Mr Jon Milner for making sure that everything was working in the cleanroom

Finally, I would like to thank my family - Andri, Stelios and Katerina for their constant support, and also my girlfriend Nasia, for always being there to support me.

List of Publications

Journal Publications

1. **M. Athanasiou, T. K. Kim, B. Liu, R. Smith and T. Wang,** 'Fabrication of two-dimensional InGaN/GaN photonic crystal structure using a modified nanosphere lithography technique', *Appl. Phys. Lett.* 102, 191108 (2013).
2. **M. Athanasiou, R. Smith, B. Liu, T. Wang, '**Room temperature continuous-wave green lasing on silicon', *Sci. Rep.* 4, 7250 (2014).
3. **T. Kim, B. Liu, R. Smith, M. Athanasiou, Y. Gong and T. Wang,** 'Coherent nanocavity structures for enhancement in internal quantum efficiency of III-nitride multiple quantum wells', *Appl. Phys. Lett.* 104, 161108 (2014).
4. **J. Bai, C. C. Yang, M. Athanasiou and T. Wang,** 'Efficiency enhancement of InGaN/GaN solar cells with nanostructures', *Appl. Phys. Lett.* 104, 051129 (2014)**.**
5. **B. Liu, R. Smith, M. Athanasiou, X. Yu and T. Wang**, 'Temporally and spatially resolved photoluminescence investigation of (11-22) semi-polar InGaN / GaN grown on nanorod templates', *Appl. Phys. Lett*. 105, 261103 (2014).

Conference Contributions

1. **T. Kim, M. Athanasiou and T. Wang** ,'Fabrication of an ordered monolayer of silica nanospheres on InGaN/GaN MQWs structure by a spin coating method for application to GaN-based optical emitter', UK Nitrides Consortium Sheffield July 2012.
2. **M. Athanasiou, T. Kim, R. Smith and T. Wang**, 'A simple approach to fabrication of 2-D InGaN / GaN photonic band crystal structure', UK Nitrides Consortium, Cardiff January 2013.
3. **T. Kim, B. Liu, R. Smith, M. Athanasiou and T. Wang**, '88-fold enhancement in internal quantum efficiency of InGaN/GaN nanodisks due to a coherent nanocavity effect', UK Nitrides Consortium, Cardiff January 2013.

4. **M. Athanasiou, T. Kim, B. Liu, R. Smith and T. Wang,** '2nd generation in fabrication of a two dimensional III-nitride based Photonic band Crystal Structure using a novel lift-off technique ', UK Nitrides Consortium Sheffield July 2013.
5. **M. Athanasiou, T. Kim, B. Liu, R. Smith and T. Wang,** 'Fabrication of two-dimensional InGaN/GaN photonic crystal structures using a novel lift-off technique', International Conference on Nitride Semiconductors, Washington D.C. Aug. 2013.
6. **M. Athanasiou, B. Liu, R. Smith and T. Wang,** 'Blue lasing from an InGaN/GaN MQWs micro-disk on Si with a record low threshold', UK Nitrides Consortium Bristol January 2014.
7. **M. Athanasiou, B. Liu, R. Smith and T. Wang,** 'Recombination dynamics investigation at room temperature of a green emission lasing from an InGaN/GaN Based microdisk on Si Substrates', UK Nitrides Consortium Sheffield July 2014.
8. **M. Athanasiou, B. Liu, R. Smith and T. Wang,** 'Room Temperature Green Lasing of an InGaN/GaN MQWs Microdisk on Si Substrate', International Conference on Nitride Semiconductors Wroclaw, Poland. Aug. 2014.

Table of Contents

List of Figures

List of Tables

CHAPTER 1

Introduction

1.1 Introduction

In this chapter the context of the thesis and the motivation and potential applications for III-nitride based optoelectronics devices will be introduced. This thesis is focused on the fabrication of nanostructure devices that enhance the optical properties of III-nitrides. A nanosphere lithography technique was extensively used in order to overcome lithography resolution restrictions.

1.2 Aims and Motivation

The 'greenhouse effect', the major factor for causing climate change over the years as shown in Fig. 1.1, drives a number of scientists worldwide to look for suitable means of reducing decreasing carbon emissions. In nowadays electricity is mainly generated from non-environmentally friendly sources such as oil, coal and gas, and thus is one of the main sources of carbon emissions. In order to reduce carbon emissions 15 European Union (EC) member countries including the UK signed the Kyoto Protocol in 1997. The Kyoto Protocol states that the overall greenhouse emissions will have to be reduced by 20% compared to the levels in 1990 by 2020, and reduced by 85-90% by 2050 [1].

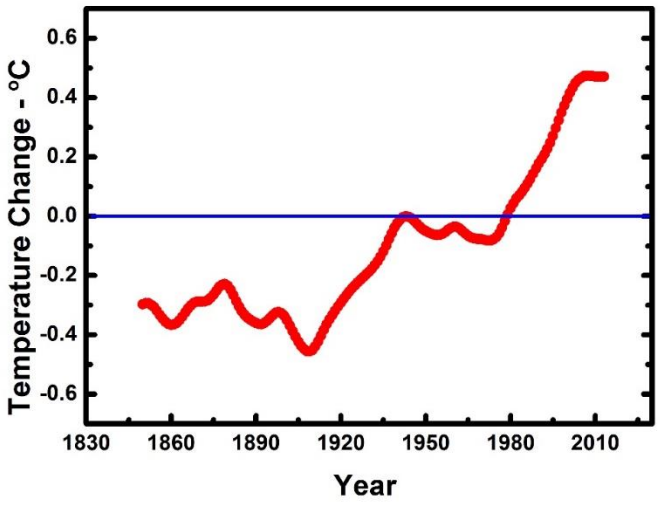

Figure 1.1 Temperature change over the years.

In order for the EU countries to reach the challenging targets, it is crucial to develop new technologies for sustainable and green energy, such as wind or solar energy, which help to reduce carbon emission. Additionally, a decrease in energy utilisation for general illumination is required through developing energy efficiency lighting sources.

1.3 Light Sources

Lighting accounts for 29% of global electricity consumption is used for lighting purposes annually [2]. Therefore, it would significantly save energy and reduce carbon emissions if energy efficient lighting sources could replace the present incandescent bulbs and fluorescent tubes. Solid state Light emitting diodes (LED) are an ideal candidate for this replacement, as LEDs are >10 times more efficient than conventional lighting sources in theory. Figure 1.2 illustrates the luminous efficacy of different light sources (Lumens per Watt) over the last 60 years, demonstrating the major advantage of white LEDs, mainly based on III-nitride semiconductors [3].

A step forward in reducing energy consumption for general illumination has been taken in the Europe through the legislation of prohibiting the sale of 100-Watt incandescent light bulbs set by the European Union on 1st September 2009,

requiring that the sale of all incandescent bulbs has to be phased out completely from supermarket by 1st September 2012.

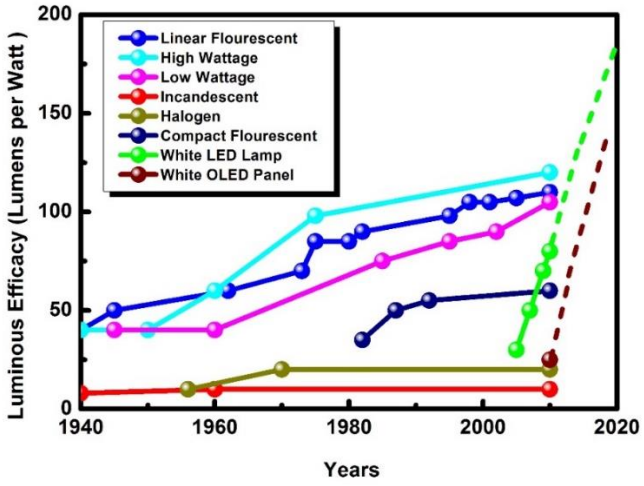

Figure 1.2 Luminous efficacy for various lighting technologies plotted over the years of their development [4].

The compact size, long life-time (up to 50,000 hours) and low energy consumption of LEDs make them attractive for utilisation of general illumination. LED devices have not only been used in solid state lighting but also for example in LED TV backlighting, traffic lights and automotive lighting. However, currently white LEDs based on III-nitrides is still far from the theoretical limit in respect of converting the injected electrical energy to optical energy and thus cannot replace the conventional lighting source. Consequently, further development is still required to improve their luminous efficacy of the LEDs.

1.4 History of III-Nitrides LEDs

The first LEDs emitting in the red spectral region demonstrated by Holonyak Jr. and Bevacqua [5] was based on GaAsP. Considerable effort has been devoted to further extending into the visible region with shorter wavelength, for example, increasing phosphorus composition in GaAsP. Unfortunately, GaAsP exhibits indirect band structure if phosphorus concentration is higher than 44%. As a result the efficiency drops approximately to 0.005% [6]. Therefore, this makes it an

unsuitable way to produce light at shorter wavelengths. Isoelectronic doping of GaP with nitrogen in 1968 resulted in yellow to green (550 nm) emission LEDs.

The last two decades have seen major achievements in the field of III-nitride semiconductor materials and optoelectronics, leading to three Nobel Prize Winners in Physics for the year 2014 who have made revolutionary contributions to III-nitride epitaxial growth. Figure 1.3 shows that III-nitrides have direct bandgaps across their entire composition range, covering the complete visible spectrum and a major part of the ultraviolet (UV) (from 0.7 eV for InN, through 3.5 eV for GaN, to 6.2 eV for AlN), and therefore can find a wide range of applications, such as solid state lighting, high definition displays, visible light communication, environmental protection, solar energy applications and healthcare etc.

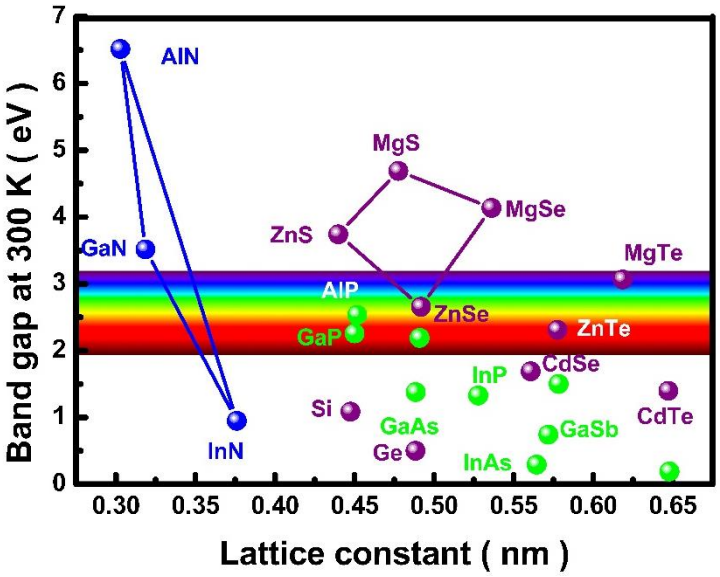

Figure 1.3 Bandgap energies of semiconductors versus their lattice constant [7].

In 1968 Herbert Maruska reported GaN films grown by HVPE on sapphire. This approach results in 16% lattice mismatch, giving rise to unintentional n doping [8]. The great challenge is growth of p-type GaN films which are crucial for the formation of a p-n junction. Based on previous experience in growing p-GaAs and p-GaP, he started doping Zn into GaN. The consequence was extremely

disappointing. The film quality was poor and had high resistivity making it unusable for the formation of p-n junctions. Zn-doped GaN was semi-insulating and also had a reddish colour due to high density of defects.

Subsequently, Maruska and Pankove determined the bandgap of GaN by optical investigation in 1970, which is 3.4 eV at room temperature [9]. In 1971 the first electroluminescence (EL) measurements by Pankove and his co-workers [10] were performed on unintentionally n-type doped GaN film/Zn-doped GaN structure with metal as contacts. The peak detected was at 2.6eV. Despite that the EL emission was observed from the device, I-V characteristics were very poor as a result of the semi-insulating Zn-doped GaN layer. Maruska also tried to dope Mg into GaN in 1972 in order to obtain p-GaN. Although p-type GaN was still not obtained, the first violet emission device was observed in 1973 and was bright enough to observe the emitted light in a well-lit room [11]. The emission was coming from the Mg dopants.

Meanwhile, rapid progress in III-nitrides drew a lot of attention from a number of scientists as they realise that GaN has great potential to achieve high performance LEDs for solid state lighting. The initial research was mainly focused on improving the crystal quality of GaN films due to the, large lattice mismatch between GaN and sapphire substrate used. In 1986 Amano and Akasaki invented so-called two step growth approach which has become a standard method for the growth of GaN on sapphire using a metal organic vapour deposition (MOCVD) technique, namely, an initial AlN nucleation with a thin was deposited at a low temperature on sapphire in order to compensate the large strain as a result of the lattice-mismatch before the growth of GaN layer at a high temperature. The two-step approach represents a major breakthrough in the growth of GaN, leading to significant improvement in crystal quality of GaN and also for the first time achieving an atomically flat surface [12, 13]. The p-type doping problem was overcome in 1989 by Amano and Akasaki et al. [14], through using low energy electron beam to activate Mg doped GaN. This led to the realisation of the first LED based on a GaN p-n junction by Amano and Akasaki in 1992 [15], emitting in

the UV-region of the spectrum. Finally, in 1993, Nakamura working at Nichia Industries in Japan demonstrated thermal activation of the Mg doped dopants by annealing the p-type film under nitrogen ambient, which was another major breakthrough required for industrial mass-production. The first blue, green and yellow electrically injected LED devices based on an InGaN/AlGaN quantum well (QW) system were reported by Shuji Nakamura in 1994, with efficiencies of 7.3%, 2.1% and 1.2% respectively [16]. Due to their revolutionary contribution to development of GaN-based LEDs, the 2014 Nobel Prize for Physics was awarded to Professors Isamu Akasaki, Hiroshi Amano and Shuji Nakamura.

1.5 Challenges to Overcome in III-Nitrides

As mentioned previously in section 1.3, research in III-nitride semiconductors increased rapidly over the following years after the pioneering work by Professors Isamu Akasaki, Hiroshi Amano and Shuji Nakamura, evidenced by Fig. 1.4, demonstrating a significant increase in number of publication, starting in late 1980s and early 1990s.

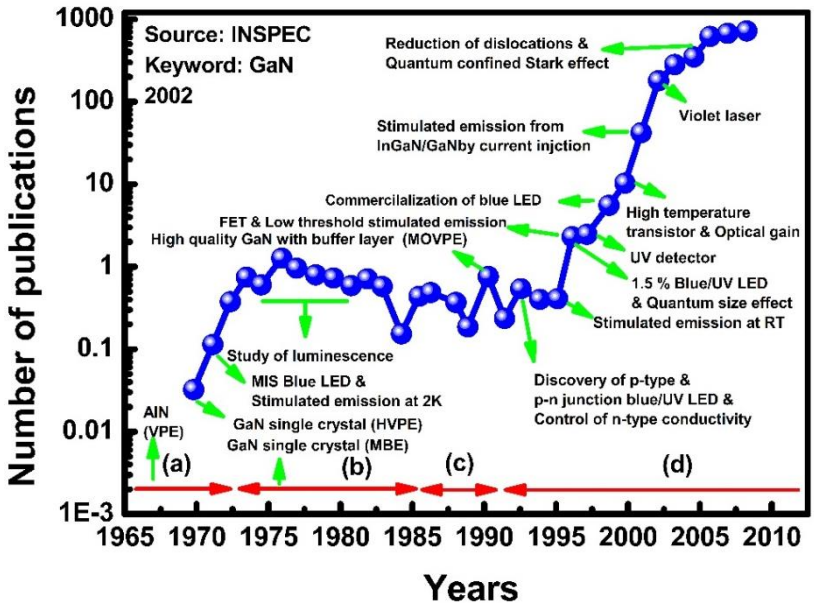

Figure 1.4 Number of publications related to III-Nitrides from 1965 up to 2000 [17].

1.5.1 The 'Green Gap' Phenomenon

One of the main advantages of InGaN/GaN quantum well technology is that the emission wavelength can be tuned from deep UV to near infrared region by changing the concentration of indium, which can cover the entire visible spectrum. However, by increasing the indium composition of InGaN the efficiency of the device dramatically decreases. The problem becomes more prominent when the wavelength moves toward green and yellow spectral regions with increasing indium composition. For yellow emission GaP incorporated with nitrogen could be used for the fabrication of yellow emitters. However, extending the GaP: N system to shorter wavelengths by reducing the concentration of nitrogen will lead to an indirect bandgap, and consequently a low optical efficiency is expected as discussed in section 1.4.

This phenomenon, as demonstrated in Fig. 1.5, is so-called 'Green/yellow Gap', where the efficiency drops off rapidly in this specific region of the spectrum.

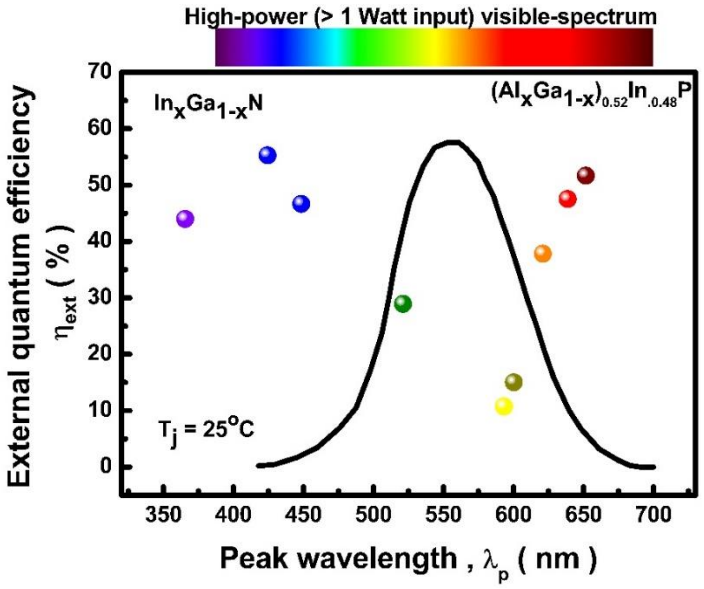

Figure 1.5 External Quantum efficiency of LEDs emitting in the visible region of the spectrum at room temperature. V (λ) corresponds to the human eye response [18].

The ultimate white light LED is based on Red-Green-Blue (RGB) technology, meaning that utilisation of the three primary colours of the visible spectrum (red/green/blue) to generate any colour, which includes white. Therefore, it is necessary to first solve the 'green gap' problem.

1.5.2 Quantum Confined Stark Effect (QCSE)

Due to the Wurtzite crystal structure of III-nitrides (see Chapter 2) a spontaneous polarization is expected to be along the c-direction [19]. The lattice mismatch between AlN, GaN and InGaN leads to a piezoelectric field in forming heterstructures. The induced piezoelectric field's exhibit pronounced importance in InGaN/GaN based quantum well structures as a result of compressive strain which InGaN layer suffers. As a result electron-hole wave functions will be pulled apart, thus reducing the overlap between them. This is so-called quantum confined Stark effect (QCSE). A further increase in the indium composition, to achieve longer wavelength emission, will result in an increased lattice mismatch between InGaN and underlying GaN. A stronger piezoelectric field will therefore be induced in the QWs and cause further reduction in the overlap of the electron-hole wave functions. QCSE is therefore the major reason for the limit in further improving optical performance of current III-nitride based emitters. This becomes more severe with increasing emission wavelength one of the major reasons for causing "green/yellow" gap. Figure 1.6(a) illustrates the ideal scenario for the quantum wells, where there is no piezoelectric fields induced.

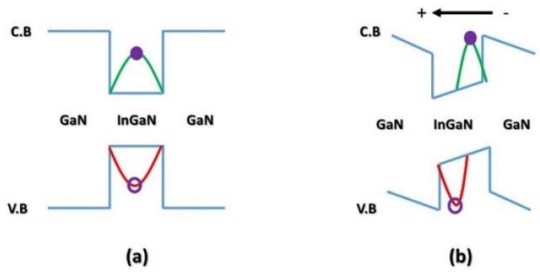

Figure 1.6 (a) An ideal case of InGaN / GaN QWs without any induced piezoelectric field (b) InGaN / GaN under strong piezoelectric fields.

In a contrast, the band diagram for an InGaN/GaN quantum well structure grown on c-direction (0001) is illustrated in Fig. 1.6 (b), where the electron–hole wave functions are clearly separated as a result of the lattice-mismatch induced piezoelectric fields. This reduction in the overlap of the electron–hole wave functions leads to a decrease in oscillator strength, and thus optical quantum efficiency. The presence of QCSE in the quantum wells also reduces the effective band gap of the structure and leads to a decrease in the energy of the emitted photons, which causes redshift in emission wavelength.

Several methods have been proposed in order to reduce the lattice-mismatch induced piezoelectric fields. The growth of III-nitrides in different orientation such as non-polar or semi-polar can help eliminate or reduce the piezoelectric fields [20-22]. However, due to unavailability of cost effective substrates for the growth of III-nitrides on non-polar or semipolar orientation, makes the commercialisation of this technology impossible for now. Another way of increasing the optical efficiency of III-nitride based heterostructures is by fabricating nanostructures using top-down methods. It has been shown that nanostructures can result in a strain relaxation across the quantum wells [23, 24]. Fabricating nanostructures through the InGaN/GaN quantum wells allows the crystal lattice to relax, resulting in an increase in the radiative efficiency of the device. This will cause the blue shift in emission wavelength. An additional advantage of fabricating nanostructures it provides an increase in the extraction efficiency, allowing more light generated to escape out of the devices [25, 26].

1.5.3 Efficiency Droop

Another major challenge is the so-called "efficiency droop", meaning a significant reduction in internal quantum efficiency (IQE) with increasing injection current, for example, the IQE can fall by up to 50% from its peak value at the drive currents required for practical applications. This problem becomes more severe as the emission wavelength shifts towards the green/yellow spectral region. This is also

a severe problem for fabrication of blue emitters with high output power for general illumination.

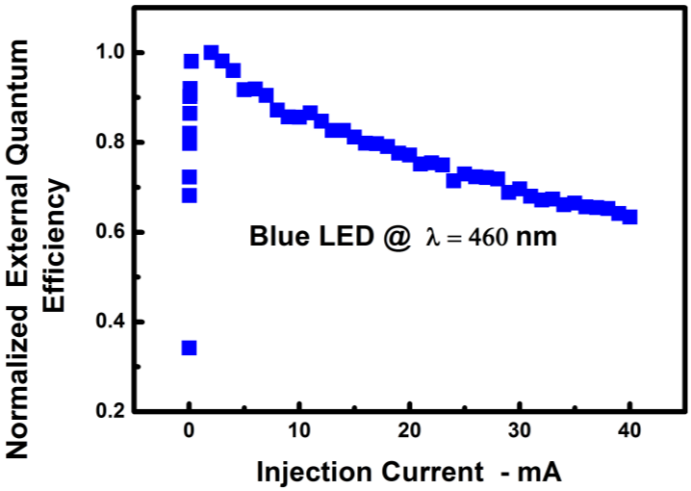

Figure 1.7 Normalised external quantum efficiency versus injection current for a blue LED device emitting at 460 nm.

Figure 1.7 shows a typical external quantum efficiency of a commercial blue LED, demonstrating efficiency droop starting even at a few mA injection current which is far from requirements for practical applications. There are intensive dates about the origins for the cause of the "efficiency droop", such as-Auger recombination [27] and leakage current [28].

Auger recombination is the non-radiative recombination of carriers, where the excess energy of recombination is reabsorbed by a third carrier, allowing it to be excited to a higher energy level [29], resulting in the decrease in quantum efficiency at higher injection currents where this event is most likely to happen.

Solving the “efficiency droop puzzle” that is the efficiency droop effect is vital to achieving high brightness LEDs for solid state lighting.

1.5.4 Light Extraction

The last two decades have seen major achievements since the pioneering work done by Amano, Akasaki in late 1980s and Nakamura in early 1990s. However, it is still necessary to further improve optical performance of blue LEDs in order to

replace currently conventional lighting sources. In addition to the requirements for further increasing IQE, extraction efficiency also needs to be increased. The major limit to extraction efficiency is due to the large contrast in refractive index between GaN and air. The optical performance of LEDs are limited because the majority of the light generated inside the device is trapped by total internal reflection (TIR); and is lost either by collisions with the crystal lattice, creating phonons, causing a temperature increase or by being reabsorbed by the quantum wells.

The light generated as a consequence of the recombination of electron-hole pairs that can travel in any direction. If the propagated light from the device hits the GaN/Air interface with angle ($\Theta_{ins.}$), and an incident angle is larger than the critical angle required for total internal reflection GaN ($\Theta_{ins.} > \Theta_c$), the light is totally reflected, as shown in Figure 1.8. On the other hand, if the propagated light hits the GaN/air interface with an angle smaller than the GaN critical angle then the light is extracted.

Unfortunately the large difference in refractive index between GaN and air results in a small GaN extraction angle (~24^0), and thus most of the generated light is reflected back into the device.

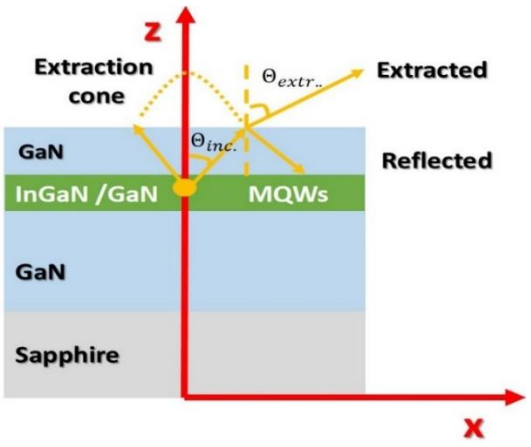

Figure 1.8 Description of the total internal reflection occurs in LED devices.

A number of approaches have been used to overcome this problem, such as incorporation of surface texturing [30, 31]; and in more complicated systems,

introduction of so-called photonic crystal structures [32, 33], where light trapped inside the device can be manipulated and directed by suppressing the light propagation in a slab mode and then enhancing it along a vertical mode. The fabrication of photonic crystals structures, can result in the formation of photonic bandgaps for certain energies in the xy-plane. This will prohibit the formation of slab modes, which tend to be stay trapped inside the device and redistributing their energy outside the device. Additionally, the fabrication of photonic crystal structures could result in controlling the directionality of the light and modification of the spontaneous emission rate (see Chapters 4 & 5).

1.5.5 Carrier Effective Mass and Lasing Threshold

III-Nitride semiconductors generally exhibit much heavier effective masses of carriers (both electrons and holes) than those of other III-V semiconductors, as seen in Table 1.1, where the fundamental material parameters of a number of typical III-V semiconductors have been provided.

In general, wide band gap semiconductors such as III-nitrides suffer from high thresholds for population inversion and lasing, typically in the kA/cm^2 range. This high J_{th} is to a large degree an intrinsic limitation due to the high carrier densities of states resulting from the high masses in wide band gap materials.

Material	E_g (eV)	Electron effective mass (m_e/m_0)	Hole effective mass (m_h/m_0)
GaAs	1.424	0.063	0.51
InP	1.34	0.08	0.6
GaN	3.4	0.2	0.8

Table 1.1 Energy bandgap and electron and hole effective masses of GaN and other III-V semiconductors. The free electron rest mass (m0) is 9.11x10-31 kg.

The current density for lasing threshold is directly related to carrier density required for meeting transparency conditions given by (1.1) [34].

$$I_{th} = \frac{eVn_{tr}}{\tau} \qquad (1.1)$$

Where V is the volume of the active region, n_{tr} is the threshold of carrier density for meeting transparency conditions, τ is the recombination lifetime of carriers and e is the magnitude of the electron charge. Several methods have been proposed to reduce the threshold for lasing in III-nitrides, including the use of quantum dots [35]. However, it is far from satisfactory, as the lasing threshold till tends to be in kA/cm^2 range due to the high carrier density required for transparency condition.

1.6 Substrates

The major problem of GaN is due to large lattice-mismatch epitaxial growth as a result of lack of suitable and affordable substrate. Free-standing GaN substrates are presently available, but are extremely expensive. Consequently, they are less attractive. Currently, the typical approach for fabrication of free-standing GaN substrates is to use a hydride vapour phase epitaxy (HVPE) technique. Free-standing GaN with a thickness of up to 300 µm can be obtained by means of a deposition of GaN using gallium chloride (GaCl) and ammonia (NH_3) on foreign substrates, typically, like sapphire [36] and subsequently removing the foreign substrates using laser-lift technique or others [37- 40].Bowing effects and cracking problems are typically experienced during the substrate removal process.

Sapphire is the most popular substrate for GaN growth [61], although the lattice mismatch and the difference in thermal expansion coefficient between sapphire and GaN are very large, 16% and 25.5% [41], repectively.

Silicon Carbide (SiC) as a substrate for GaN growth exhibits less lattice-match (3.4% for 6H-SiC) compared with sapphire. However, SiC is too expensive to be used for growth of blue LEDs. Typically, the price of 2 inch 6H-SiC is approximately $1000 [43], making SiC substrates unsuitable for mass production purposes.

Silicon faces even more severe challenges as a substrate for GaN. Silicon (Si) substrates are the least expensive in comparison to the other main competitors at $40 for an 8 inch wafer [44]. Additionally, the availability of silicon substrates in large sizes, up to 12 inch, and the well-established processing technology of such wafers make them commercially attractive for mass production as it can further reduce the overall cost of LEDs. Although there are a number of potential benefits that might be gained from using Si as foreign substrate, the lattice mismatch of Si to GaN epilayers is even larger (~17%) and the larger thermal expansion coefficient further causes serious problems in the growth of GaN epilayers. Therefore the usage of Si as a foreign substrate poses on its own several challenges that need to be overcome.

1.7 Nanoscale Lithography Techniques

III-nitride based nano devices potentially exhibit a number of major advantages as a result of strain relaxation, and thus are expected to lead to significant enhancement in optical performance and some novel properties which cannot be achieved by the devices with a standard size. However, fabricating of nano devices is severely limited by the resolution limitation of standard optical lithography techniques or the actual fabrication cost using other advanced techniques, which restrict them from mass production.

1.7.1 Fabrication of Self organised Nanorod arrays

Our team has developed so-called self-organised Ni nano-mask approach in last 5 years. In this method a thin layer of Ni is deposited on the top of a silicon dioxide layer which is initially prepared on the surface of the GaN epiwafer. The metal layer is then thermally annealed in order to form self-organised nickel nano-islands as a first nanomask for etching through the silicon oxide. The Ni/silicon oxide nano-islands serve as a second mask for further etching into GaN-based nano-rod array structure [45, 46]. It is a simple and cost-effective approach, making this type of fabrication be ideal for mass production. This approach has been widely applied in fabrication of nano-rod array LEDs with significantly

improved surface [62]. This approach also led to the demonstration of first room temperature III-nitride based nano-plasmonic lasing with an ultra-low threshold [56, 57]. It has also been applied in fabrication of III-nitride nano-devices for solar powered hydrogen generation with significantly improved efficiency [58-60]. This approach has also been extended for fabrication of nanorod array templates for further overgrowth of semipolar or non-polar GaN templates, leading to significant improvement in crystal quality.

Despite the advantage of this technique, the difficulty in accurately controlling size and shape due to the random formation of nano-islands, makes it inappropriate for the fabrication of periodic arrays or well defined cavities with a strict control.

1.7.2 Electron Beam Lithography

In electron beam lithography (EBL), the focused beam of electrons is used to write a nano patterned structure on a soft photoresist material for further device fabrication. A sub-10 nm resolution can be achieved, and any pattern can be designed and transferred to the soft photoresist [47, 46]. Despite the excellent properties of this technique is extremely timing-consuming and thus is limited to the fabrication of small size wafers. This prevents its use for mass-production.

1.7.3 Nano-Imprint Lithography

Nano-imprint lithography (NIL) technique is another method that can be used in the fabrication of nanostructures [49, 50]. Nanostructures are patterned on the surface of a thin polymer film which is initially deposited on epiwafers by pressing a rigid master, which contains surface relief features. The advantage of using NIL is that it does not require any sophisticated tools for masking and allows nanoscale designs. The rigid master is usually prepared by e-beam lithography. Imprinting the polymer film allows further etching that will transfer its pattern into the underlying epiwafers. This method is ideal for large scale fabrication, with a relatively low cost. The major drawback of NIL is that once the rigid mask is

written it cannot be changed. Moreover, the rigid master is expensive and has a limited lifetime. Normally, the rigid mask is written on Si wafers; unfortunately Si wafers are fragile, thus minimising the usage of the rigid mask to approximately 10 to 15 times.

1.7.4 Nanosphere Lithography

Nanosphere lithography is an inexpensive technique, and nano-mask patterning is obtained through coating dielectric nano-particles, which can be formed in a very regular manner [51]. These nano-particles can serve as a two [52] or three [53] dimensional mask for the fabrication of photonic crystal structures fabrication or micro-cavity lasers [5]. Using nanosphere lithography, nanostructures can be fabricated using simple equipment. The resolution of the resulting nanostructures is defined by the nanosphere size. The particles can be found in a large variety from tens of nanometres up to several microns.

Several techniques for deposition of nanoparticles have been studied and applied during the last few years. The lift–up deposition method requires that the device is immersed into a tank filled with nanoparticles diluted in a solution. When the device is lifted from the tank a film of self-aligned particles adheres to the wafer surface. This layer then serves as an etching mask. The lift-up deposition method is not used in this work.

Another technique, used in this work is a spin coating method where a solution containing silica nanospheres, is deposited on the samples. Such a deposition technique provides several advantages: it is fast, cost effective and has a high degree of reproducibility.

1.8 Conclusion

In this Chapter a brief introduction on the history of III-Nitrides was presented. The major challenges that needed to overcome for improving the performance of the GaN based LEDs are introduced; such as the green gap, the quantum confined stark effect, the efficiency droop , light extraction and the high lasing thresholds.

Finally, the typical nanostructure fabrication techniques were presented, as well as the introduction of our own cost effective fabrication technique using nanosphere lithography.

References

[1] EU greenhouse gas emissions and targets, http://ec.europa.eu/clima/policies/g-gas/index_en.htm [Accessed: 5th August 2014].

[2] Light goes out for incandescent bulbs, http://www.theguardian.com/environment/2012/aug/31/lightbulbs-incandescent-europe [Accessed: 5th August 2014].

[3] EU Directive on Eco-Design (ErP), http://www.osram.co.uk/osram_uk/news-and-knowledge/eu-directive-on-eco-design-erp/index.jsp [Accessed: 5th of August 2014].

[4] Lumens Per Watt: The Next Step of the White LED Revolution, http://www.topbulb.com/blog/lumens-per-watt-next-step-white-led-revolution/ [Accessed: 6th August 2014].

[5] S. F. Bevacqua and N. Holonyak, *Appl. Phys. Lett.* vol. **1**, p. 82 (1962).

[6] J. I. Pankove and H. P. Maruska., *Solid State Electron.* vol. **10**, p. 917 (1967).

[7] Compound semiconductors: Physics, technology and device concepts, http://www-opto.e-technik.uni-ulm.de/lehre/cs [Accessed: 10th August 2014].

[8] H. Maruska and J. Tietjen, *Appl. Phys. Lett.* vol. **15**, p. 327 (1969).

[9] J. Pankove, J. Berkeyheiser, H. Maruska and J. Wittke, *Solid State Commun.* vol. **8**, p. 1051 (1970).

[10] J. I. Pankove, E. A. Miller, D. Richman and J. E. Berkeyheiser, *J. Lumin.,* vol. **4**, p. 63 (1971).

[11] H. Maruska, W. Rhines and D. Stevenson, *Mater. Res. Bull.* vol. **7**, p. 777 (1972).

[12] H. M. Manasevit, F. M. Erdmann and W. I. Simpson, *J. Electrochem. Soc.* vol. **118**, p. 1864 (1971).

[13] K. Hiramatsu, S. Itoh, H. Amano and I. Akasaki, *J. Cryst. Growth* vol. **115**, p. 628 (1991).

[14] H. Amano et al., *Jpn. J. Appl. Phys.* vol. **28**, p. L2112 (1989).

[15] E. Schubert, *Light emitting diodes, 2nd ed.* (Cambridge University Press, 2003).

[16] S. Nakamura, M. Senoh, N. Iwasa and S. I. Nagahama, *Jpn. J. Appl. Phys.* vol. **34**, p. L797 (1995).

[17] K. Takahashi, A. Yoshikawa and A. Sandlu (Eds.), *Wide Bandgap Semiconductors,Fundamental Properties and Modern,* 1st ed. (Springer, 2007).

[18] M. R. Krames *et al.*, *J. Display Technol.* vol. **3**, p. 160 (2007).

[19] S. Nakamura and S. F. Chichibu*, Introduction to Nitride Semiconductor Blue Lasers and Light Emitting Diodes,* 1st ed. (New York and London: Taylor & Francis,2000).

[20] P. Waltereit *et al.*, *Nature,* vol. **406**, p. 865 (2000).

[21] Y. Zhao *et al.*, *Appl. Phys. Express.,* vol. **4**, p. 082104 (2011).

[22] M. Funato *et al., Jpn. J. Appl. Phys.* vol. **45**, p. L659 (2006).

[23] Q. Wang, J. Bai, Y. P. Gong and T. Wang, *J. Phys. D: Appl. Phys.* vol. **44**, p. 2661 (2011).

[24] B. Liu, R. Smith, J. Bai, Y. Gong and T. Wang, *Appl. Phys. Lett.* vol. **103**, p. 101108 (2013).

[25] S. H. Kim *et al.*, *Optics Expr.* vol. **21**, p. 7125 (2013).

[26] D. H. Joo, H. K. Lee and J. S. Yu, *Phot. Techn. Lett.* vol. **24**, p. 1381 (2012).

[27] Y. C. Shen *et al., Appl. Phys. Lett.* vol. **91**, p. 141101 (2007).

[28] M. F. Schubert, Q. Dai, J. K. Kim and E. F. Schubert, *Appl. Phys. Lett.* vol. **91**, p. 183597 (2007).

[29] E. Kioupakis, P. Rinke, K. T. Delaney and C. G. Van de Walle, *Appl. Phys. Lett.* vol. **91**, p. 181103 (2007).

[30] T.K.Kim *et.al., Jpn. J. Appl. Phys.* vol. **48**, p. 021002 (2009).

[31] T.K.Kim *et.al, Appl. Phys. Lett.* vol. **94**, p. 161107 (2009).

[32] A.David *et.al., Appl. Phys. Lett.* vol. **88**, p. 061124 (2006).

[33] K. McGroddy *et.al., Appl. Phys. Lett.* vol. **93**, p. 103502 (2008).

[34] J. Davies and A. Long, *Physics of Semiconductors 2002: Proceedings of the 26th International Conference* (Edinburgh: CRC Press, 2002).

[35] M. Zhang, A. Banerjee, C. S. Lee, J. M. Hinckley and P. Bhattacharya, *Appl. Phys. Lett.* vol. **98**, p. 221104 (2011).

[36] N. M. Nasser *et al., J. Microw. Optoelectron.* vol. **2**, p. 22 (2001).

[37] S. S. Park *et al*., *Jpn. J. Appl. Phys.* vol. **39**, p. L1141 (2000).

[38] M. K. Kelly *et al., Phys. Status Sol. (a),* vol. **159**, p. R3 (1997).

[39] K.Motoki *et al., Jpn. J. Appl. Phys.* vol. **40**, p. L140 (2001).

[40] Y. Oshima *et al., Jpn. J. Appl. Phys.* vol. **L1**, p. 42 (2003).

[41] Emerging markets to save sapphire substrates?, http://www.compoundsemiconductor.net/article/90333-emerging-

markets-to-save-sapphire-substrates.html [Accessed: 4th September 2014].

[42] M. O. Manasreh, *GaN and Related Materials-(Optoelectronic Properties Of Semiconductors And Superlattices),* 1st ed. (Amsterdam: Gordon and Breach Science Publishers, 1997).

[43] MTI coorparation, http://www.mtixtl.com/sic6h_1.aspx [Accessed: 4th September 2014].

[44] 12-inch wafer prices continue to fall, http://www.geek.com/chips/12-inch-wafer-prices-continue-to-fall-551410/ [Accessed: 6th September 2014].

[45] J. Bai, Q. Wang and T. Wang, *Phys.Status.Solidi.(a),* vol. **209**, p. 77 (2012).

[46] P. Renwick, H. Tang, J. Bai and T. Wang, *Appl. Phys. Lett.* vol. **100**, p. 182105 (2012).

[47] H. Altug, D. Englud and J. Vukovic, *Nat. Phys.* vol. **2**, p. 484 (2006).

[48] M. G. Scullion, T. F. Krauss and A. D. Falco, *IEEE Photon. J.* vol. **3**, p. 203 (2011).

[49] N. Okada *et al., Jpn. J. Appl.Phys.* vol. **52**, p. 11NG02 (2013).

[50] S. H. Kim, K. D. Lee, J. Y. Kim and M. K. Kwon, *Nanotech.* vol. **18**, p. 055306 (2007).

[51] K. Lee *et al., Microelectr. Eng.* vol. **96**,p. 45 (2012).

[52] M. Athanasiou, T. K. Kim, B. Liu, R. Smith and T. Wang, *Appl. Phys. Lett.* vol. **102**, p. 191108 (2013).

[53] A. Chiappini, C. Armellini, N. Bazzanella, G. Righini and M. Ferrari, *Opt. and Photon. J.* vol. **2**, p. 206 (2012).

[54] Y. Zhang, Z. Ma, X. Zhang, T. Wang and H. W. Choi, *Appl. Phys. Lett.* vol. **104**, p. 25598738 (2014).

[55] S. M. Yang, S. G.Jang, D. G. Choi, S. Kim and H. K. Yu, *Small* vol. **2**, p. 458 (2006).

[56] Y. Hou, P. Renwick, B. Liu, J. Bai and T. Wang, *Sc. Rep.* vol. **4**, p. 5014 (2014).

[57] Y. J. Lu *et al., Science* vol. **37**, p. 450 (2013).

[58] J. Benton, J. Bai and T. Wang, *Appl. Phys. Lett.* vol. **102**, p. 173905 (2013).

[59] J. Benton, J. Bai and T. Wang, *Appl. Phys. Lett.* vol. **103**, p. 133904 (2013).

[60] J. Benton, J. Bai and T. Wang, *Appl. Phys. Lett.* vol. **105**, p. 223902 (2014).

[61] Sapphire Substrate to Dominate LED Market in 2014, http://www.ledinside.com/outlook/2013/12/sapphire_substrate_to_dominate_led_market_in_2014 [Accessed: 30th March 2015].

[62] J. Bai, Y. P. Gong, K. Xing, X. Yu, and T. Wang , *Appl. Phys. Lett.* vol. **102**, p. 101906 (2013)

CHAPTER 2

Background

2.1 Semiconductors

Materials are separated into three main categories related to their electrical properties, which are conducting, insulating and semiconducting. A conductive material has the ability to easily allow the flow of electrically charged carriers through it (e.g. metals), while the materials that do not allow electrically charged carriers to flow are called insulators (e.g. glass). Semiconductors are a material with the ability to conduct better than insulators but less than conductors [1, 2].In metals the resistivity was found in the order of few times 10^{-8} Ωcm [69], where in semiconductors is in the order of 10^{4} Ωcm for GaN [70]. On the other hand the resistivity of glass which is an insulator, was found to be in the order of 10^{14} Ωcm [69]. The conductivity of semiconductors can be tuned through doping a small amount of certain impurities with different levels. For n-type doped semiconductors extra electron energy levels are introduced in the forbidden gap below the conduction band. In a p-type doped semiconductor extra hole energy levels are introduced above the valence band.

III-Nitride semiconductors are the ideal candidates for optical devices because of their direct bandgap properties. Additionally, they can cover a wide range of energies that extends from 6.2 eV (AlN) to 0.7 eV (InN) [3], which covers from

deep ultraviolet (UV) to near infrared spectral region. In this study, nanostructures were fabricated in order to enhance the optical properties of InGaN/GaN multiple quantum well (MQW) based devices emitting in the visible spectral region.

2.2 Crystal Structures

Gallium nitride and its related alloys are attractive materials due to their direct and wide band structure, thermal and chemical stability. The crystal structure of III-nitrides is defined by the way the atoms are stacked together, leading to three different configurations which are defined as zincblende, rock-salt and hexagonal wurtzite structures [4], as shown in Figure 2.1

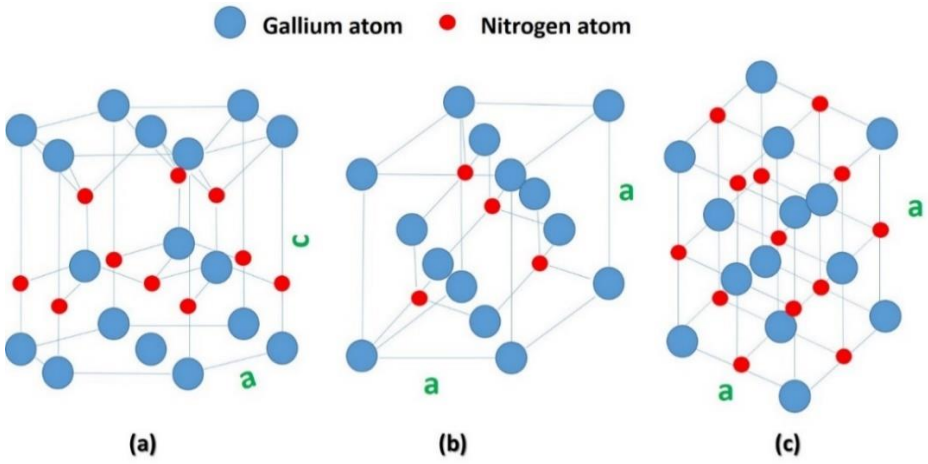

Figure 2.1 Three types of GaN crystal structure (a) wurtzite structure, (b) zincblende structure, and (c) rock-salt structure. [5]

The most common is the hexagonal wurtzite crystal structure as it is the most thermodynamically stable under ambient conditions. In a wurtzite crystal structure the atoms are stacked in a hexagonal closed packed plane (HCP) along (0001) direction (c-plane). The wurtzite crystal structure has two lattice parameters labelled as "*a*" and "*c*". In Fig. 2.1 (a) an inter-atomic distance along the in-plane direction is defined as lattice constant "*a*", while an inter-atomic distance in the out of plane direction (perpendicular to the in-plane) is lattice constant "*c*" [6].

In a zincblende structures which is typical of Si, MgO and GaAs [7], the crystal has a cubic unit cell, as shown in Fig. 2.1(b), described with a single lattice constant "*a*". Wurtzite and zincblende crystal structures are similar but their main differences are due to the bond angle with their second nearest atom. In the zincblende structures there is a 60^{o} rotation, where as in the wurtzite structure there is no rotation between the stacking orders of the atoms [6, 7].

III-nitrides with a rock-salt crystal structures can only be formed through placing a wurtzite structure under very high pressure [8], and cannot be produced by any epitaxial growth technique. The pressure required for this phase transition is approximately 50 GPa [9] for GaN, approximately 20GPa for AlN [10] and approximately 12 GPa for InN [11], respectively.

2.3 Chemical and Electrical Properties of III-Nitrides

2.3.1 Chemical Properties of III-Nitrides

The excellent chemical and thermal stability of III-Nitrides makes them attractive in a number of different applications such as power electronics and optoelectronics. Table 2.1 below shows the material parameters of III-Nitrides.

Material	Bandgap (eV)	Permittivity (F/m)	Refractive Index (η_x)	Lattice Constant (Å)	Melting Point (^{o}C)
ALN	6.2	8.5	2.18	a=3.112, c=4.982	3000
GaN	3.39	8.9	2.49	a=3.189, c=5.186	2500
InN	0.65	15.3	2.9	a=3.553, c=5.693	2146

Table 2.1 Material parameters of AlN, GaN and InN and refractive indices at 450 nm [12-15].

Generally, III-nitrides exhibit high resistance to chemical solution and high melting temperature, and consequently III-nitride based devices can be used in a harsh

environments. However, some chemical solutions, such as KOH or NaOH, can attack GaN through defects under certain conditions, such as wet-etching at elevated temperatures or photo-electrochemical etching technique.

2.3.2 Electrical properties of III-Nitrides

The electrical properties of GaN compared to other III-V semiconductors are listed below in Table 2.2.The wide bandgap, high breakdown voltage and high temperature stability make GaN ideal for the fabrication of electronics devices for high frequency and high temperature applications. Currently, unintentional doped GaN exhibits n-type as a result of defects such as Ga vacancies or dislocations.

Material	Bandgap (eV) at 300 *K*	Electron Mobility *(cm^2/Vs)*	Thermal Conductivity *(W/cm^0C)*	Breakdown Field *(MV/cm)*
GaAs	1.42	8500	0.4	0.4
GaN	**3.39**	**1000**	**2.3**	**5**
InP	1.34	5400	0.68	0.5
SiC	3.26	700	3.6	2

Table 2.2 Electrical characteristics of GaN compared against other III-V semiconductor materials [13, 16 -18].

Silicon is a typical dopant for achieving n-type GaN with an accurate control in electron density and electron mobility, and its activation energy is ~25 meV [19]. Therefore, basically, all doped silicon can be thermally activated at room temperature.

Mg is a typical p-dopant and p-type GaN can be obtained through high-temperature activation of Mg-doped GaN under nitrogen ambient. It is necessary

to heavily doped Mg into GaN in order to obtain p-type GaN, as the typical activation energy for p-GaN is very high, up to 150 meV [20].

2.4 Optical Properties of III-Nitrides

Figure 2.2 presents recombination mechanisms after electrons are excited from valence band to conduction in a semiconductor. The electron-hole recombination can be either radiative or non-radiative.

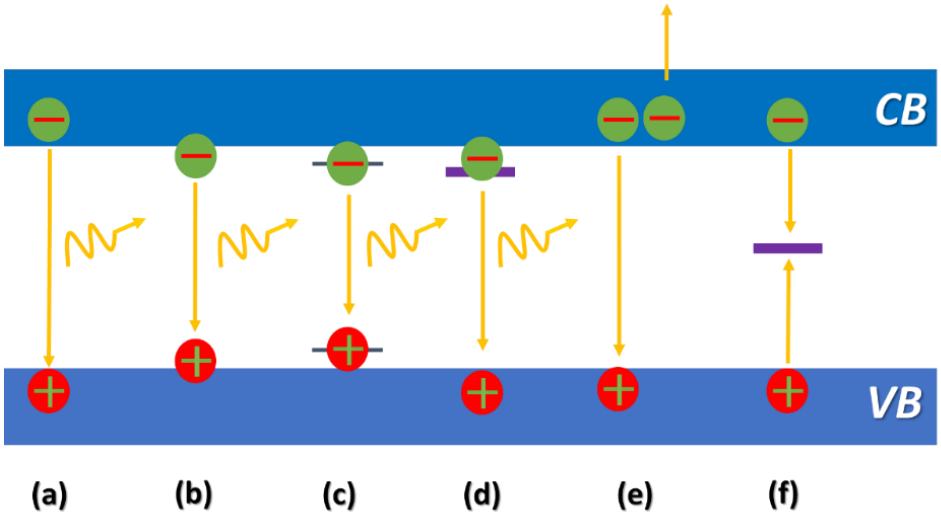

Figure 2.2 Recombination mechanisms for the excited carriers in III-Nitrides.

In the case of radiative recombination an electron in the conduction band loses its energy through recombination with a hole in the valence band, leading to the generation of a photon. The resulting photon energy from this process is equal to the bandgap ($E_g = \frac{hc}{\lambda}$) of the material. This process is illustrated schematically in Figure 2.2(a) [21].

Figure 2.5(b), illustrates the excitonic recombination mechanism. After being excited optically or electrically, two kinds of charged carriers, negatively charged electrons and positively charged holes, will form excitons due to Coulomb potential. This increases the probability of radiative recombination. An exciton is a neutrally charged particle, and could be either free exciton or bound exciton, which are also called the Wannier-Mott and Frenkel exciton respectively. In

semiconductors a free exciton is more likely to occur, where a tightly bound exciton is more likely to occur in an insulator crystal. The free electron binding energy is small due to the large separation between holes and electrons. Applying the Bohr model the exciton binding energy can be estimated by (2.1) below.

$$E_n = -\frac{\mu}{m_0}\frac{1}{\varepsilon_r^2}\frac{R_H}{n^2} \qquad (2.1)$$

Where R_H is the Rydberg constant for a hydrogen atom (13.61 eV), and ε_r is the dielectric constant of the material. The excitonic binding energy in GaN is approximately 26 meV, which is similar to the thermal energy at room temperature [22]. Excitonic recombination will have slightly lower emission energy than band edge emission due to the subtraction of the exciton binding energy ($E_G - E_{exciton}$).

Figure 2.2(c), illustrates a schematic of donor-acceptor recombination process. When a semiconductor material is doped with either n-type or p-type impurities new energy levels can be introduced, and will be below the conduction band or above the valence band, respectively. This recombination mechanism will result in emission energy less than the material energy bandgap.

Recombination of carriers that occurs within the bandgap of a material as result of impurities is presented in Fig. 2.2(d). This type of recombination mechanism results in the emission of photons with a reduced energy. The so-called yellow band emission often observed in GaN, in particular, silicon-doped GaN, is due to this kind of recombination mechanism [23, 24].

The Auger recombination mechanism is illustrated schematically in Fig. 2.2(e), where a third carrier is involved. In such a process the excess energy created from electron and hole recombination is absorbed by a third carrier in either the conduction band or valence band, and the third carrier is excited to a higher energy state. Normally, Auger recombination takes place when the density of excited carriers is high [71].

Figure 2.2(f) describes non-radiative recombination schematically. In this situation when an electron and hole recombine their energy is lost due to phonon involvement, either as heat or lattice vibrations, as a result of defects or impurities.

2.5 Low Dimensional Structures

A low dimensional system is defined as a system with confinement along at least one of the 3- dimensions (x, y, and z). Due to advanced epitaxial growth or post fabrication techniques, a device with a confined region on the order of a few angstroms to a few of nanometres can be achieved. Such well-defined structures enhance the confinement along at least one direction [25]. In quantum mechanics quantum confinement states will be generated when at least one dimension is comparable to the magnitude of the de Broglie wavelength of the carriers, the energy level of such carriers becomes quantized in that direction. The de Broglie wavelength is given by (2.2).

$$\lambda \approx \frac{h}{\sqrt{m_e^* k_B T}} \qquad (2.2)$$

Where h corresponds to Planck's constant, m_e^* is the electron effective mass and k_B is the Boltzmann constant$(1.38 \times 10^{-23}\ \mathrm{m^2 kg s^{-2} K^{-1}})$.

If the confinement occurs along one direction, it is labelled as a quantum well structure. A quantum wire structure means that there is a confinement along two directions. Quantum dots have confinement along all three dimensions.

2.6 Density of States (DoS)

The density of states (DoS) in a semiconductor is defined as the number of available states per interval of energy at each energy level that electrons can occupy per unit volume [26]. Figure 2.3 below shows the DoS as a function of dimensionality: (a) bulk semiconductor without any confinement, which is called as three dimensional system (3D); (b) quantum wells with confinement along one direction, which is called a two-dimensional system (2D); (c) quantum wires with

confinement along two directions, which is defined as a one dimensional system (1D); and (d) quantum dot with a confinement along all three directions, which we call zero dimensional system (0D). Figure 2.3 demonstrates that the DoS increases with reducing dimension in a quantum well.

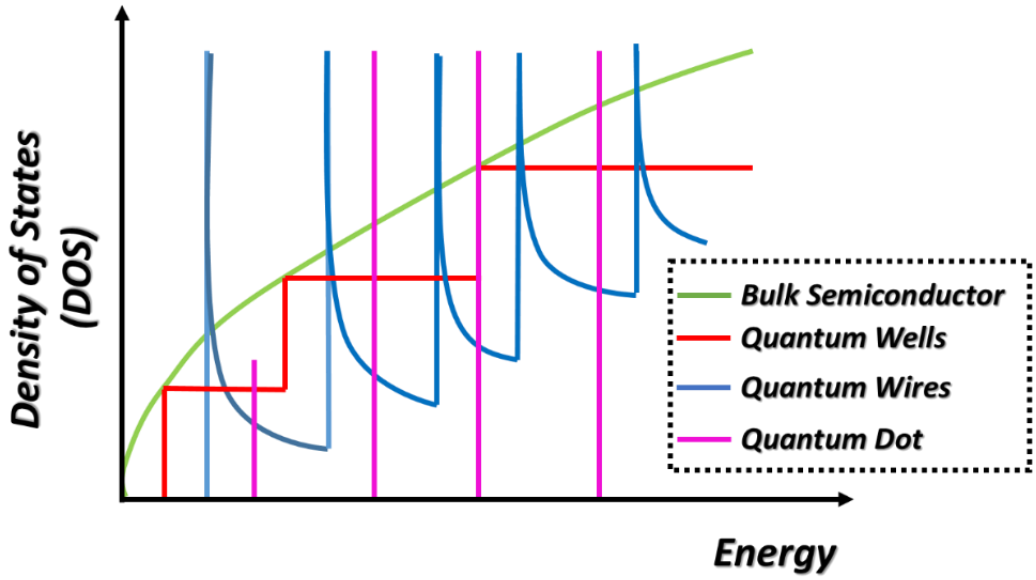

Figure 2.3 DoS as a function of dimensionality.

2.7 Carrier Localisation Effect

Exciton localisation in InGaN alloys is generally generated due to a low miscibility between InN and GaN, leading to indium segregation when indium composition is beyond a certain value. In some cases, a fluctuation in the thickness of InGaN quantum well [27] may also cause the exciton localisation effect. Localisation centres will have slightly lower bandgap energy as a result of higher indium composition [28, 29]. The effects of exciton localisation play a crucial role in the emission mechanism for III-Nitrides semiconductors. Despite the high defect density that InGaN based emitters suffers,such emitters exhibit high optical efficiency [72].This can be attributed to the effect of carrier localisation. The carriers are trapped inside the deep localisation centers prohibiting them to diffuse across the material and non-radiatively recombine with defects.

2.8 Photonic Crystals

Photonic crystal structures have been widely used, for controlling the directionality of the emitted light, for high extraction efficiency devices, optical fibers and nanocavities laser [42, 74, 75]. PhC effect occurs when the refractive index is periodically varied in at least one dimension. The concept of PhC structures was first introduced by Lord Rayleigh in 1888, when one-dimensional (1D) structures were investigated [75]. In 1987, Yablonovitch introduced the concept of two-dimensional (2D) PhC structures, which would help to control the photon densities of states (DoS). Controlling the photon DoS means that spontaneous emission can be controlled [30-37]. Numerous challenges needed to be overcome in order to fabricate 2D PhC structure in the visible spectral region. The main challenge is due to the difficulty of fabricating sub-micron periodic arrays. In 1996, Krauss et al., demonstrated the first 2D PhC structure, fabricated using electron beam lithography on an AlGaAs semiconductor, showing a clear photonic bandgap in the near-infrared region [38, 39].

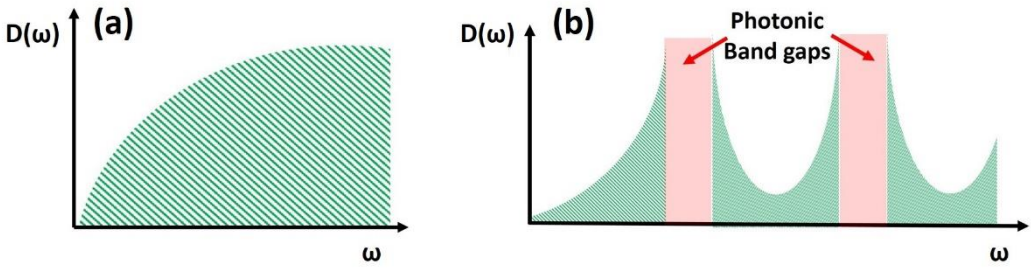

Figure 2.4 Schematic illustration of the photonic density of states (D (ω)) for (a) a homogeneous material and (b) with a photonic crystal.

Similar to electronic states, photons have a density of states (DoS).Figure 2.4 (a) illustrates the photonic density of states for a homogeneous medium, while Fig. 2.4 (b) shows photonic density of states for a PhC. For the optical modes, the density of states describes the allowed number of states per frequency (ω). Fig. 2.4 (b) shows that the numbers of available photonic DoS at a number of particular frequencies (ω) are zero, thus implying a photonic bandgap at these

specific frequencies. This means there are no optical modes allowed over these frequency ranges [40].

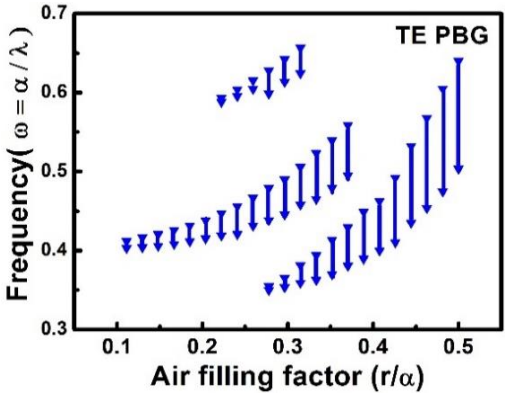

Figure 2.5 Band gap map of two dimensional PhC of nanoholes in Transverse electric (TE) modes.

Figure 2.5 shows a TE photonic bandgap map as a function of the air-filling factor for a hexagonal array, where the PhC lattice is 270 nm and the refractive index is assumed to be 2.5 for the case of GaN. The blue regions on the graph correspond to the photonic bandgaps, where the photonic DoS is zero for these certain frequencies. The filling factor and the photonic bandgap can be tuned by changing the nanohole size. The photonic bandgap map plotted in Fig. 2.5, is crucial for the design of PhC structures, as it allows to choose the appropriate structural parameters (i.e. nanohole diameter) in order to match the emission from sample to the PBG, see Chapter 4.

Photonic crystals are periodic arrays of nanostructures that can affect light propagation in a device. In a photonic crystal the refractive index varies periodically in at least one direction. The light propagating inside the device can interact with PhC, along the direction(s) where the refractive index is varying. Similar to the bandgaps in semiconductors, PhC can form forbidden bandgaps for certain wavelengths across the direction where refractive index is varying, thus prohibiting their propagation.

Spontaneous emission can be substantially reduced by using a photonic crystal structure to introduce photonic bandgaps [41]. The photonic crystal effectively

makes propagation of wavelengths within the phtonic 'forbidden gap' impossible. It was predicted that the PhC effect could lead to the inhibition of spontaneous emission in undesired directions and then allow redistribution of this emission in a direction required. In 2005, Noda's group observed inhibition of the optical modes along the 2D slab-plane direction (i.e. slab modes) and redistribution of the spontaneous emission to the direction normal to the slab (i.e. vertical modes) in a 2D GaAsInP semiconductor PhC slab [42]. The emission in slab modes is effectively suppressed when the emission wavelength lies within the PhC bandgap, while the emission in vertical modes is significantly enhanced. This can lead to a major improvement in the extraction efficiency and directionality of spontaneous emission.

Similarly to semiconductors, a PhC structure is also subject to quantum mechanical confinement effects. Figure 2.6 depicts schematics of 1D, 2D and 3D PhC structures, respectively. A 1D PhC means the refractive index is periodically varied only along one dimension (for example, the z-direction in Fig. 2.6 a), the difference in refractive indices is proportional to the size of the photonic band-gap. The 1D PhC has been widely used in fabrication of advanced opto-electronics, such as vertical cavity surface emitting lasers (VCSEL). Figure 2.6 (b) illustrates 2D PhC structure, where the refractive index is periodically varied in two dimensions (e.g. x-y dimensions).

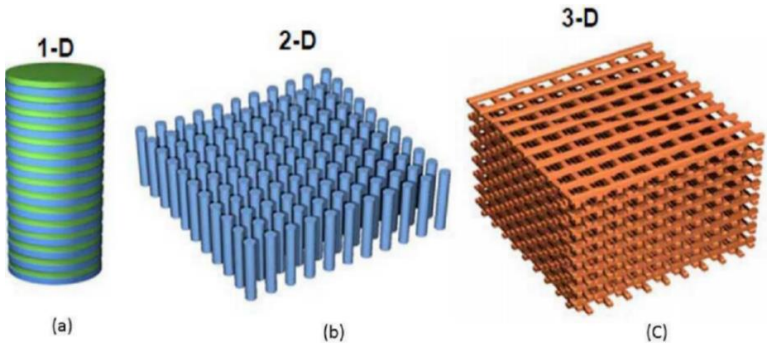

Figure 2.6 (a) One-dimensional photonic crystal structure, (b) two-dimensional photonic crystal structure, and (c) three-dimensional photonic crystal structure [43].

The photonic bandgap will inhibit the propagation of the specific wavelengths in the direction of the variation in refractive index. If a defect is intentionally introduced along the periodicity of the array, will cause the formation of high photonic DoS for certain wavelengths. In this way PhC cavity lasers can be designed by deliberately introducing defects to the array.

Figure 2.6(c) shows a more complex 3D PhC structure, where the refractive index is periodically changed in all three directions (x-y-z). Although the first 3D PhC was demonstrated in 1999 [44], unfortunately such structures pose a number of challenges in difficulties in fabrication, as the pattern have to be defined into all three dimensions. This would imply, an accurate control of the lithography and etching techniques used to define and transfer the pattern into the material. Especially for III-Nitrides, the etching techniques used, either dry or wet chemical are difficult to control in all three-dimensions.

2.9 Microcavities

The control of light interactions allows for a wide range of applications in optical communications, digital displays and thresholdless lasers. In semiconductor lasers coherent photon emission results when the emitting dipole is in resonance with the optical cavity modes. Therefore it is vital to understand how to tune the cavities resonance in order to match the emission wavelength for achieving low-loss optical cavities.

Ideally confinement of light in an optical cavity would not incur any loss. In optical microcavities the number of cavity resonances that overlaps with the spontaneous emission spectrum of the active region strongly depends on the size of the cavity. Reducing the size of the cavity allows control over the number of cavity resonances that overlap with the emission spectrum. The two key factors responsible for achieving high quality microcavities is the Q-factor and the effective mode volume.

Figure 2.7(a) – (d) shows a number of different types of semiconductor optical microcavities schematically. Figure 2.7(a) shows a schematic representation of a single micropillar cavity based on a Fabry-Perot cavity [45, 46]. In such a microcavity the light confinement is achieved in an area stacked between two sets of Bragg reflectors, which consist of alternating layers of materials with different refractive indices. The thickness of the cavity region (the area 'sandwiched' between the regions) is typically in the order of a few emission wavelengths. The arrow indicates the emission direction of the cavity.

In Fig. 2.7(b) a microdisk cavity is illustrated. This type of microcavity differs from standard Fabry-Perot cavities as light confinement is achieved under total internal reflection (TIR) conditions [48, 49]. The light circulates at the periphery of the disk forming whispering gallery resonances in the same manner in which sound waves travel in St. Paul's Cathedral in London, UK. The 3D confinement of light, due to air that surrounds the disk, can result in higher Q-values by comparison to standard Fabry-Perot cavity.

In Fig. 2.7(c) illustrates a hybrid plasmonic laser. This type of cavity confines light using surface plasmon coupling which gives confinement in a very small area [50 - 52]. Such a cavity is also known simply as a hybrid cavity. This because it combines both a plasmonic cavity and Fabry-Perot cavity, where light bounces between the two flat facets of the nanorods. A thin SiO_2 layer (approximately 5nm) is deposited on top of a silver (Ag) film and nanorods are laid on top of the SiO_2 layer. The light is confined in the SiO_2 layer along the direction perpendicular to the metal/dielectric interface. Due to the small effective mode volume plasmonic lasers suffer from considerable propagation loss.

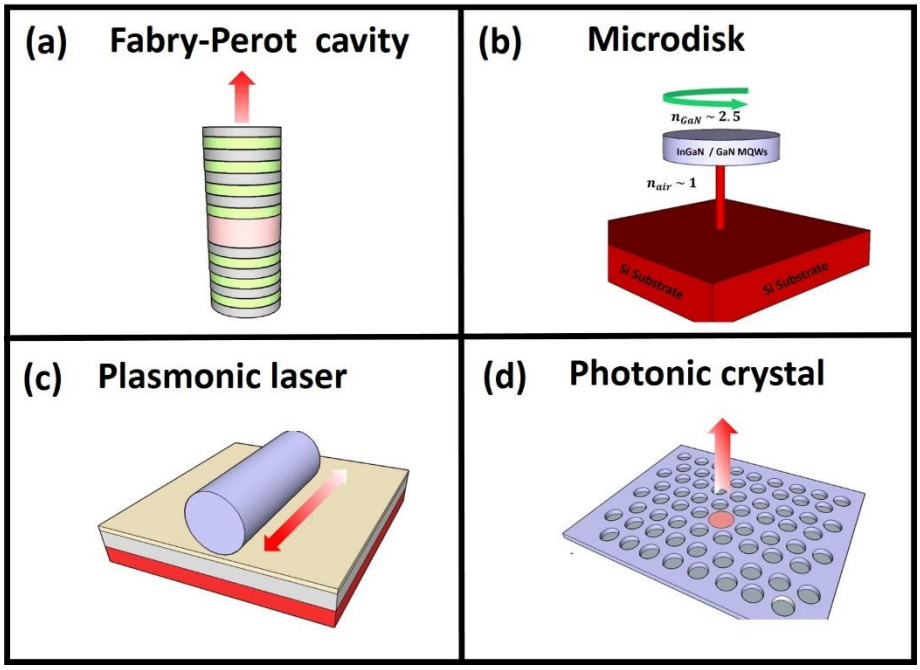

Figure 2.7 Types of semiconductor optical microcavities: (a) Fabry-Perot microcavity; (b) microdisk cavity; (c) plasmonic nanolaser; and (d) phonic crystal nanocavity laser.

Finally Fig. 2.7 (d) shows a photonic crystal nanocavity [52-54]. In these cavities the periodicity of the array of nanoholes offers a Bragg reflection in the xy-plane. Intentional hole is inserted in the centre of the array introduces a defect, which allows defect modes to be formed, by localising the light in small areas. This results in the rapid increase in the DoS for certain wavelengths. Despite their excellent optical performance in terms of lasing threshold and minimising the size of the cavity, compared to standard Fabry Perrot lasers [76 - 78], such structures poses several difficulties in terms of fabrication. EBL technique is often used to define such structures, which prohibits the realisation of this type of lasers for commercial purposes. Additionally sacrificial layers or Bragg reflectors need to be grown prior the membrane structure, for increasing the light confinement along the vertical direction [77, 78].

When an emitter is placed in a special environment, such as in a micro cavity, spontaneous emission can be enhanced as the dipole can radiate much faster if the dipole is in resonance with the cavity mode. This phenomenon is observed as

the number of DoS for certain energies seen by the dipole are increased and the dipole decay rate increased. The photons are emitted in the cavity mode. On the other hand, if the dipole is not in resonance with the cavity mode, then the available DoS seen by the dipole are decreased [55], thus decreasing the recombination rate of dipole. Figure 2.8, demonstrates a dipole placed in cavity, where the light is confined between the two mirrors. If the dipole is in resonance with the cavity mode then the decay rate (Γ) of the dipole increased.

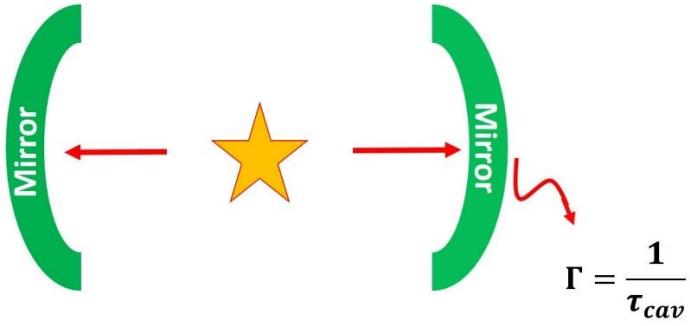

Figure 2.8 A Dipole placed in a cavity with the light bouncing between the mirrors.

The existence of this phenomenon was first theorised by Purcell in 1946 and described by (2.3).

$$F_p = \frac{\Gamma_{cav}}{\Gamma_0} = \frac{3}{4\pi^2}\left(\frac{\lambda_c}{n}\right)^3\left(\frac{Q}{V_{eff}}\right) \qquad (2.3)$$

Where Γ_{cav} and Γ_0 the emission rate in a system with and without an optical cavity, respectively; λ_c is the cavity emission wavelength, n is the refractive index, V_{eff} is the effective mode volume and Q is the quality factor of the cavity. From (2.3) Purcell spontaneous enhancement is dependent on the ratio of the Q-factor and effective mode volume (V_{eff}). Therefore, a large Q factor and small effective mode volumes are required in order to obtain large spontaneous emission enhancement. In order to achieve enhanced spontaneous emission (i.e., high Purcell factor) the emitter must be in resonance with the cavity, meaning that the cavity mode wavelength (λ_c) must match the emission wavelength of the emitter used (λ_e). One important requirement that needs to be fulfilled to have a

high coupling efficiency between the emitter photon and cavity resonance is that the linewidth of emitter dipoles are narrower than the cavity resonance [57].

Time-resolved spectroscopy is normally used to measure the Purcell enhancement. When the dipole (exciton) is in resonance with the cavity mode the photon density of states increases allowing the dipole to radiate faster compared to a vacuum, and thus enhancing the spontaneous emission rate [58].

The Purcell effect also can approximated using equation 2.4.

$$F_p \approx \frac{\beta}{1-\beta} \tag{2.4}$$

Where β is the spontaneous emission coupling factor, which can be estimated experimentally using a log-log plot of integrated intensity against optical excitation pumping. The spontaneous emission coupling factor is defined as the fraction of the total spontaneous emission from the emitter dipole, coupled into a cavity mode; estimated from the ratio of output intensities below and above the lasing threshold [59, 60]. Spontaneous emission of a cavity can be controlled by designing a cavity where dipole and cavity modes operate in a strong coupling regime. The lasing threshold can also be reduced as described by Goy, 1983 [61]. Goy continued working on the problem and, around 1998, used InAs quantum dots in micropillars and microdisk cavities to obtain a reduced lasing threshold.

In order to achieve high β the number of modes supported by the cavity that overlap with the emission spectrum must be minimised. The number of modes that overlap with the emission spectrum for a microdisk cavity, which is of particular interest in this study, can be estimated using the free spectral range (FSR) equation, given below in (2.5).

$$\Delta\lambda_{WG} = \frac{\lambda_{cav}^2}{2\pi Rn} \tag{2.5}$$

Where λ_{cav} is the whispering gallery mode (WG) mode wavelength, R is the microdisk radius and n is the refractive index. From the FSR equation an obvious dependence of the mode separation is observed. As the disk radius increases the mode separation decreases, and thus the number of modes that overlap with the

emission spectrum increases. Also because microdisk cavities are three-dimensional their thickness must be controlled in order to suppress the formation of any vertical modes. The thickness criterion is given below by (2.6).

$$T < \frac{\lambda}{2n_{GaN}} \tag{2.6}$$

Where λ is emission wavelength of the dipole and η is the refractive index. The relationship of the spontaneous emission coupling factor (β) to the number of modes, which overlap with the gain region, is given by (2.7).

$$\beta = \frac{1}{2N} \tag{2.7}$$

Where N is the number of modes which overlap with the gain region [62]. A higher β value corresponds to a lower laser threshold, as more spontaneous emission is coupled to the lasing mode. A lower number of modes overlapping the gain region is desirable because it leads to a high beta. This is a result of the direct relationship between the number of modes and the spontaneous emission coupling factor. A high beta is desirable because it yields a low lasing threshold. Therefore microdisk cavities with a smaller diameter and thin disk regions are preferable in order to reduce the number of modes that overlap the emission spectrum.

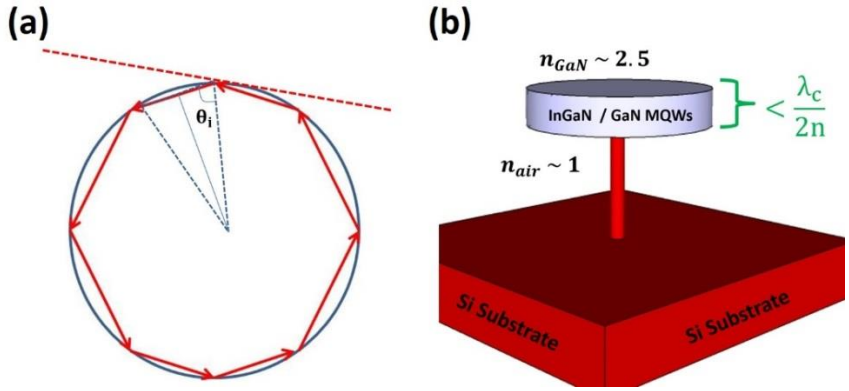

Figure 2.9 Schematic diagram of (a) the light in a microdisk circulating under TIR conditions; and (b) an InGaN/GaN MQWs microdisk on silicon substrate surrounded by air as an example.

Although WGM are optical modes that circulate the periphery of the microdisk, striking the sidewalls at an angle θ_i, as shown in Fig. 2.8(a), actual fabrication of

small microdisks results in an increased probability of the mode escaping. This is due to the fact that the angle the mode hits the cavity sidewalls is close to the GaN critical angle (approximately 24.6^{o}).

2.9.1 Whispering Gallery Mode Microdisk

The concept of whispering gallery mode (WGM) was first observed by Lord Rayleigh in 1878. He was examining a phenomenon whereby a whisper against the 32 m circular wall of the Whispering Gallery of St. Paul's Cathedral, UK, was audible to anyone with their ear to the wall [63],giving WGMs their name. In 1910, Lord Rayleigh developed his theory about sound waves in a circular setting by stating that sound could only exist at certain nodes. These patterns are called modes [64]. Taking into consideration that light has a wave-like behaviour, WGMs were observed in different types of cavities with circular geometries including microdisks, microrings and spheres. These types of cavities can be used in applications for lasing [66] and biosensors [67].

2.9.2 Quality Factor (Q) of the Cavity

One of the main factors to describe the performance of any optical resonator is the quality factor (Q). The cavity Q factor, (2.8) is defined as the ratio of the resonance wavelength and the full width at half maximum (FWHM) bandwidth of the resonance.

$$Q = \frac{\lambda_c}{\Delta\lambda} \tag{2.8}$$

Where λ_c corresponds to the cavity wavelength and $\Delta\lambda$ is the full width at half maximum of the resonant peak. Spontaneous emission enhancement, according to Purcell, is proportional to the ratio of the Q-factor and effective mode volume ($F_p \propto \frac{Q}{V_{eff}}$) .High values of Q are required for spontaneous emission enhancement.

2.9.3 Loss Mechanisms in a Microdisk Cavity

Loss mechanisms in the microdisk cavity can have a deleterious effect on the lasing properties of the cavity. Loss can be represented by a lowering of the cavity Q factor. The key loss mechanisms in a microdisk cavity are:

- Scattering loss ($Q_{scatt.}$)
- Absorption loss ($Q_{abs.}$)
- Radiation loss ($Q_{rad.}$)

The scattering losses are proportional to the surface roughness. As III-Nitrides materials are difficult to process, dry etching techniques are often applied to transfer nanostructures into the material. Unfortunately, the ion bombardment by the plasma dry etch method used to etch III-Nitrides, can cause severe damage on the sidewall of the microdisk cavity. Additionally, due to the growth of III-Nitrides on foreign substrates such as silicon or sapphire, high density of defects are introduced in the grown epilayers. Such defects can act as a scattering traps for the optical modes. Both factors can lead to the increase of the scattering losses in cavity, which then lowers the Q-factor of the resonator [68].

Absorption losses are a consequence of the intrinsic material properties given by (2.8) below.

$$Q_{abs} = \frac{2\pi n}{\alpha_{material}\lambda} \qquad (2.8)$$

Where n is the refractive index of the material, λ is the emission wavelength and α is the material absorption coefficient. When lasing threshold is reached, the material is said to be at optical transparency, thus making α material equals to zero. Therefore the losses due to material absorption are negligible compared to scattering losses.

Radiation losses are mainly the vertical radiation losses, induced by the mode coupling between the WGM and vertical radiation mode in the pedestal.The overall loss mechanism in microdisk laser is given by (2.9) below which is a sum up of the losses describe above.

$$\frac{1}{Q} = \frac{1}{Q_{abs.}} + \frac{1}{Q_{scatt.}} + \frac{1}{Q_{rad.}} \qquad (2.9)$$

As the scattering losses are major loss for a microdisk laser; minimising them could result in a high – Q factor lasers with low lasing threshold.

2.10 Conclusion

In this chapter, we address the theoretical background on III-Nitrides semiconductors. The electrical, chemical and optical properties of III-Nitrides were introduced. The concept of low dimensional structures, electronic density of states and the effect of carrier localisation in III-Nitrides was explained in detail. Additionally, the photonic crystals concept and their properties has been explained in detail. Finally, the theoretical background on microdisk resonator was introduced.

References

[1] Ben. G. Streetman and S. Banerjie, *Solid State Electronic Devices* ,7th ed. (Prentice Hall, 2014).

[2] M. Grundmann, *The Physics of Semiconductors, An Introduction Including Devices and Nanophysics,* 1st ed. (Springer, 2006).

[3] T. Onuma *et.al*., *J. Appl. Phys. Lett.* vol. **95**, p. 2495 (2004).

[4] S. Nakamura, S. J. Pearton and G. Fasol, *The blue laser diode,* 1st ed. (Berlin: Springer, 2000).

[5] F. Shi, *GaN Nanowires Fabricated by Magnetron Sputtering Deposition*, (Nanowires - Fundamental Research, 2011).

[6] H. MorkoS, *Nitrides Semiconductors and devices,* 1st ed. (*New York: Springer*, 1999).

[7] S. N. Mohammad and H. Morkoc , *Prog. Quant. Electr.* vol. **20**, p. 361 (1996).

[8] I. Gorczyca, N. Christensen, P. Perlin and I. Grzegory, *Solid State Commun.* vol. **79**, p. 1033 (1991).

[9] M. P.Halsall, P.Harmer P.J.Parbrook, and S.Hennerley *Phys.Rev.(B)* vol. **69**, p. 235207 (2004).

[10] F. J. Manjon *et al.*, *Phy. Rev.(B)* vol. **77**, p. 205204 (2008).

[11] H. Morkoç, *Handbook of Nitride Semiconductors and Devices,* 1st ed. (*Willey- VCH*, 2008).

[12] Aluminum nitride, http://www.webelements.com/compounds/aluminium/aluminium_nitride.html [Accessed: 25th September2014].

[13] Gallium Nitride, http://www.ioffe.rssi.ru/SVA/NSM/Semicond/GaN/thermal.html [Accesed: 26th September 2014].

[14] M. E. Levinshtein, S. L. Rumyantsev and M. S. Shur, *Properties of Advanced Semiconductor Materials: GaN, AIN, InN, BN, SiC, SiGe*, 1st ed. (John *Willey & Sons* ,2001).

[15] Indium Nitride, http://www.ioffe.ru/SVA/NSM/Semicond/InN/basic.html [Accessed:3rd September 2014].

[16] Properties of Gallium Arsenide, http://cnx.org/content/m22970/latest/ [Accessed: 5th October 2014].

[17] Indium Phosphide, http://www.ioffe.ru/SVA/NSM/Semicond/InP/electric.html [Accessed: 5th October 2014].

[18] SiC Ceramic Properties, http://accuratus.com/silicar.html [Accessed: 6th October 2014].

[19] S. Nakamura, T. Mukai and M. Senoh, *Jpn. J. Appl. Phys.* vol. **32**, p. L16 (1993).

[20] I. Akasaki, H. Amano, M. Kito and K. Hiramatsu ,*J. Lumin*. vol. **48**, no. 2, p. 666 (1991).

[21] M. Fox, *Optical Properties of Solids,* 2nd ed. (New York: Oxford University Press, 2010).

[22] S. J. Pearton, *GaN and Related Materials,* 1st ed. (CRC Press, 1997).

[23] M. Reshchikova and H.Morkoç, *J. App. Phys.* vol. **97**, p. 061301 (2005).

[24] X. Li, P. W. Bohn and J. J. Coleman, *Appl. Phys. Lett.* vol. **75**, p. 4049 (1999).

[25] H. Unlu , Norman J. M. Horing, *Low Dimensional Semiconductor Structures: Characterization, Modeling and Applications,* 1st ed. (Springer Science & Business Media, 2013).

[26] C. Hamaguchi, *Basic Semiconductor Physics,* 1st ed. (Springer Science & Business Media, 2009).

[27] I. Akasaki, H. Amano, M. Kito and K. Hiramatsu , *J. Lumin*. vol. **48**, p. 666 (1991).

[28] D. Watson-Parris *et al., Phys. Rev.(B) vol.* **83**, p. 115321 (2011).

[29] Y. Narukawa *et al., Phys. Rev. (B)* vol. **55**, p. R1938(R) (1997).

[30] E. Rangel *et al., Appl.Phys. Lett.* vol. **98**, p. 081104 (2011).

[31] A. David, H.Benisty and C. Weisbuch, *J. Display Technol.,* vol. **3**, p. 133 (2007).

[32] J. J. Wierer, A. David and M. M. Megens, *Nat. Photonics.* vol. **3**, p. 163 (2009).

[33] E. Matioli *et al., Appl. Phys. Lett.* vol. **98**, p. 251112 (2011).

[34] A.David *et al., Appl. Phys. Lett.* vol. **87**, p. 101107 (2005).

[35] T. K. Kim *et.al., Appl. Phys. Lett.* vol. **94**, p. 161107 (2009).

[36] C. J. Lewins *et al., J. Display Technol*. vol. **9**, p. 333 (2013).

[37] E. Matioli *et al., Appl. Phys. Lett.* vol. **98**, p. 251112 (2011).

[38] E. Yablonovitch, *Phys. Rev. Lett.* vol. **58**, p. 2059 (1987).

[39] T. F. Krauss, R. l. Rue and S.Brandi, *Nature* vol. **383**, p. 699 (1996).

[40] P. D. Fornel, J. M. Lourtioz, D. Pagnoux, H. Benisty, V. Berger, J.-M. Gerard, D. Maystre and A. Tchelnokov,*Photonic Crystals: Towards Nanoscale Photonic Devices,* 2nd ed. (Springer Science & Business Media, 2008).

[41] S. Fan, P. R. Villeneuve and J. D. Joannopoulos, *Phys. Rev. Lett.* vol. **78**, p. 3294 (1997).

[42] M. Fujita, S. Takahashi, Y. Tanaka, T. Asano and S. Noda, *Science***,** vol. **308**, p. 1296 (2005).

[43] S. Robinson and R. Nakkeeran, *Photonic Crystal Ring Resonator Based Optical Filters* (InTech, 2013).

[44] S . Kawaami *et al., Electron. Comm. Jpn. 2,* vol. **82**, p. 573 (1999).

[45] J. Gerard and B. Gayral, *J. Lightw. Technol.* vol. **17**, p. 2089 (1999).

[46] T. Tawara, H. Gotoh, T. AkasakI, N. Kobayashi and T. Saitoh, *Appl. Phys. Lett.* vol. **83**, p. 830 (2003).

[48] C. Adele *et.al., Nat.Photon.* vol. **1**, p. 61 (2007).

[49] I. Aharonovich *et al., Appl. Phys. Lett.* vol. **103**, p. 021112 (2013).

[50] Y. Hou, P. Renwick, B. Liu, J. Bai and T. Wang, *Scient. Rep.* vol. **4**, p. 5014 (2014).

[51] C. Y. Wu *et al., Nano. Lett.* vol. **11**, p. 4256 (2011).

[52] Y J.Lu *et.al., Science* vol. **337**, p. 450 (2012).

[52] C. Meier *et al., Appl. Phys. Lett.* vol. **88**, p. 031111 (2006).

[53] N. V. Triviño *et al., Appl. Phys. Lett.* vol. **100**, p. 071103 (2012).

[54] C. H. Lin, J. Y. Wang, C. Y. Chen, K. C. Shen and C. C. Yang, *Nanotech.* vol. **22**, p. 025201 (2011).

[55] E. J. R. Vesseur, F. J. G. d. Abajo and A. Polman, *Phys. Rev. (B)* vol. **82**, p. 165419 (2010).

[56] E. M. Purcell, *Phys. Rev.* vol. **69**, p. 681 (1946).

[57] S. Reitzenstein *et al., Appl. Phys. Lett.* vol. **89**, p. 051107 (2006).

[58] A. Kavokin, J. J. Baumberg, G. Malpuech and F. P. Laussy, *Microcavities*, 1st ed. (New York: Oxford University Press, 2007).

[59] K. H. Li, Z. Ma and H. W. Choi, *Appl. Phys. Lett.* vol. **98**, p. 071106 (2011).

[60] H. Takashima, H. Fujiwara, S. Takeuchi, K. Sasaki and M. Takahashi, *Appl. Phys. Lett.* vol. **92**, p. 071115 (2008).

[61] P. Goy, J. M. Haimond, M. Gross and S. Haroche, *Phys. Rev. Lett.* vol. **50**, p. 1903 (1983).

[62] D. Dragoman and M. Dragoman, *Advanced Optoelectronic Devices*, 1st ed. (Germany: Springer Science & Business Media, 1999).

[63] J. W. S. Rayleigh, *The theory of sound,* 1st ed. (London: Dover Publications, 1878).

[64] L. Rayleigh, *Philos. Mag.* vol. **20***,* p. 1001 (1910).

[65] U. Mohideen, W. S. Hobson, S. J. Pearton, F. Ren and R. E. Slusher, *Appl. Phys. Lett.* vol. **64**, p. 1911 (1994).

[67] F. Vollmer and S. Arnold, *Nature Meth.* vol. **5**, p. 591 (2008).

[68] A. W. Choi, *Handbook of Optical Microcavities,* 1st ed. (New York: CRC Press, 2014).

[69] Resistivities for common metals, http://www.cleanroom.byu.edu/Resistivities.phtml [Accessed: 30th March 2015].

[70] A. P. Grzegorczyk *et al., Phys. Stat. Sol. (c)* vol. **2**, p. 2113 (2005).

[71] F. Romer and B. Witzigmann, Opt. Express vol. **22**, p. A1440 (2014).

[72] T. Yu Edward, *III-V Nitride Semiconductors: Applications and Devices*, 1st ed. (CRC Press, 2002).

[73] Y. W. Cheng *et al., Opt. Express*, vol. **36** , p. 1611 (2011).

[74] A.David *et al., Appl. Phys. Lett.* vol. **88**, p. 061124 (2006).

[75] L. Rayleigh, *Phil. Mag* vol. **24**, p. 145 (1887).

[76] S. Nakamura *et al., Appl. Phys. Lett.* vol. **69**, p. 1568 (1996).

[77] S. W. Chen, T. C. Lu and T. T. Kao, *IEEE J. Sel. Top.* vol. **15**, p. 885 (2009).

[78] C. H. Lin *etl al., Nanotechnoly,* vol. **22,** p. 025201 (2011).

CHAPTER 3

Experimental Techniques

3.1 Introduction

In this Chapter the experimental techniques used during this study in to order to investigate and characterise the emitters based on an InGaN / GaN QWs are explained in detail. Optical characterisation techniques such as photoluminescence (PL) spectroscopy, confocal PL, micro – PL, angle dependent PL and time-resolved PL are presented. Additionally, the fabrication techniques used for the processing of III-Nitrides based devices are explained.

3.2 Optical Characterisation

3.2.1 Photoluminescence Spectroscopy

One of the most powerful and widely used optical characterisation techniques is photoluminescence (PL) spectroscopy. Electrons in a semiconductor are excited by an external lighting source whose emission energy is greater than or equal to the band edge of the material. Several pieces of information about the materials properties can be gathered using this technique such as the material bandgap, stress, and alloy composition [1]. Choice of an appropriate excitation light source emission energy allows excitation of a specific area on the heterostructure to be selectively excited and investigated.

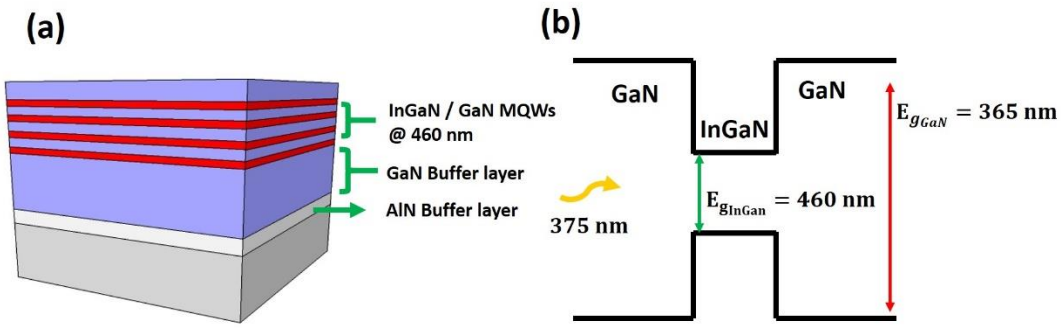

Figure 3.1 A schematic diagram of an InGaN / GaN MQWs heterostructure emitting at 460 nm (b) selective excitation of InGan QWs only by a 375 nm laser by photon absorption mechanism.

For example, only the InGaN / GaN MQWs in the heterostructure illustrated in Fig. 3.1 (a) would be excited, if the excitation source used, is a 375 nm laser. This is because the 375 nm photons from the excitation source will be invisible to the underlying GaN, whose cut-off wavelength is approximately 365nm, as Fig. 3.1 (b) shows. The main advantage of this technique over than electrically injected excitation is to provide a quick feedback, in terms of indium content in the QWs or the efficiency of device without requiring the effort of device fabrication.

Fig. 3.2 show a schematic diagram of our PL system used throughout this study. The system consists of a 375 nm continuous wave (CW) diode laser, which is used as an excitation source. The laser is reflected by an aluminium (Al) mirror with a reflectivity of > 99%, and the laser beam is then focused using a lens on to the sample.

The beam size is approximately 200 µm in a diameter. The samples are held in a helium closed-circuit cryostat in the temperature range from 10 K to room temperature. The luminescence was dispersed using a 0.5m monochromator and detected using a thermoelectrically (TE) cooled CCD detector which can be cooled down to -70˚C.

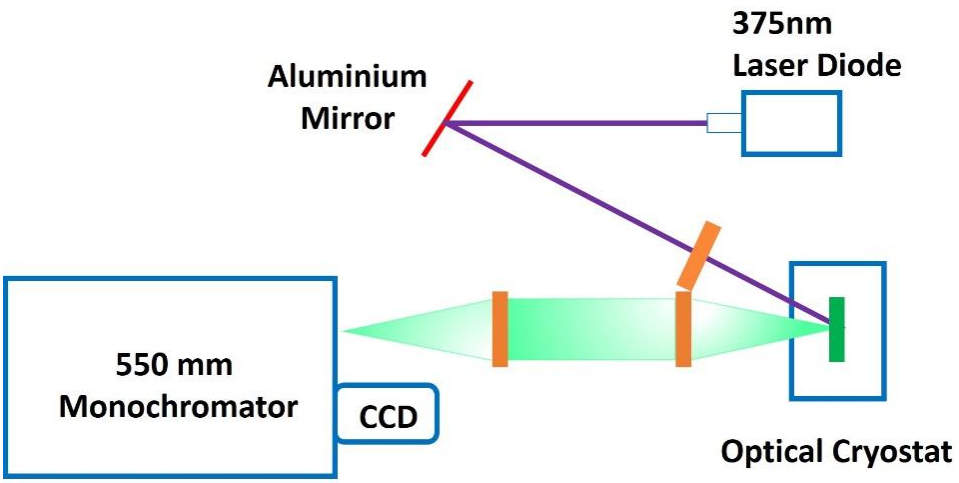

Figure 3.2 A schematic diagram of the Photoluminescence (PL) excitation system.

3.1.2 Time-Resolved Photoluminescence System

Time resolved PL (TRPL) has been used to study the excitonic dynamics of our InGaN/GaN samples PL decay time (τ_{PL}) is measured after an optical excitation with a single short pulse a sample. The spontaneous emission PL decay time consists of both the radiative and non-radiative decay components of PL emission from samples the as described shown by (3.1) [2].

$$\tau_{\mathrm{PL}} = \tau_{\mathrm{rad.}} + \tau_{\mathrm{non-rad.}} \qquad (3.1)$$

At low temperature (such as 6.5 K) it is reasonable to assume that non-radiative recombination mechanisms can be safely neglected, since non-radiative centres are frozen. Consequently it has been widely accepted [11, 12] that IQE can be assumed 100% for simplicity. This will allow extraction of the radiative and non-radiative recombination lifetimes from TRPL measurements.

Figure 3.3 presents a schematic diagram of our TRPL system, a time correlated single photon counting system. A 375 nm pulsed laser diode with a pulse width of 83 ps and an average output of 0.1 mW at a repetition rate of 10 MHz is used as an excitation source.

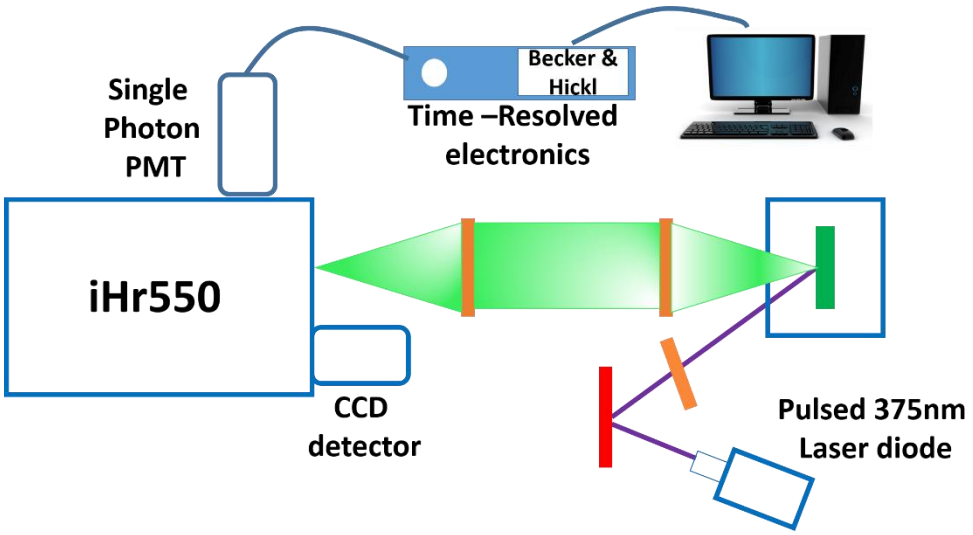

Figure 3.3 Schematic diagram of our TRPL system.

A hybrid PMT supplied by Becker & Hickl with a response of approximately 120 ps is used as a detector. Both the detector and the pulsed diode laser are synchronised using a time correlated single photon counting system (TCSPC) card with a FWHM of 6.5 ps, also supplied by Becker & Hickl. The electronics card is then connected to a computer to allow analysis of the data. The instrument response function (IRF) of the system is approximately 150 ps, described by (3.2).

$$\mathrm{IRF} = \sqrt{(\mathrm{FWHM}_{\mathrm{Laser}})^2 + (\mathrm{FWHM}_{\mathrm{Detector}})^2 + (\mathrm{FWHM}_{\mathrm{TCSPC}})^2} \qquad (3.2)$$

The measured decay lifetimes are a combination of both the IRF and the actual decay time of the semiconductor material. A deconvolution process is performed after the measurement of time decay races, using FluoFit software provided from PicoQuant.

Figure 3.4 provides a typical example of the time decay race of one of InGaN/GaN MQW sample, where the system IRF and fitted curve are also provided. The decay profile for c-plane InGaN MQWs is typically a bi-exponential decay [3, 4], which can be fitted by a bi-exponential component model given below

$$\mathrm{I(t)} = \mathrm{A_1 e^{-\frac{t}{\tau_1}}} + \mathrm{A_2 e^{-\frac{t}{\tau_2}}} \qquad (3.3)$$

Where A_1 and A_2 correspond to the fast and slow decay coefficients, respectively; and τ_1 and τ_2 are the fast and slow decay components, respectively.

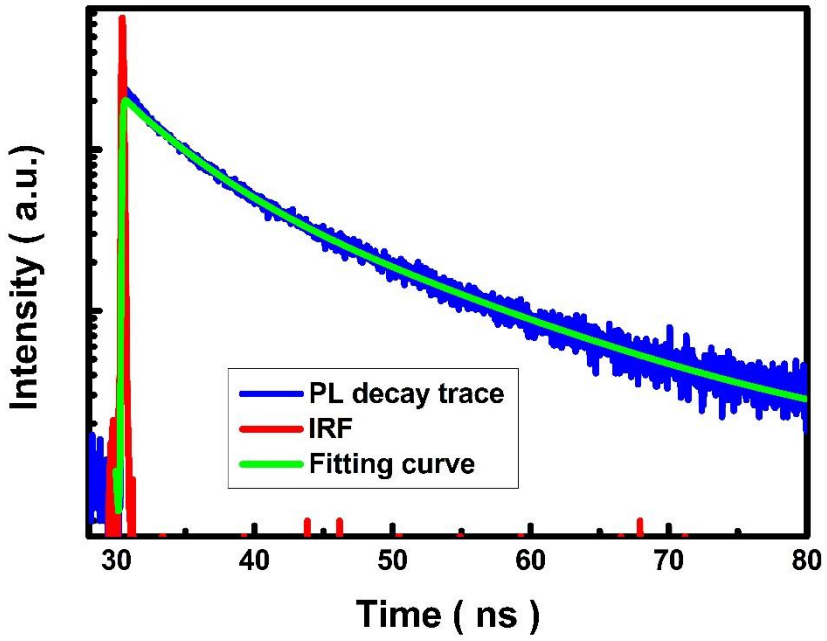

Figure 3.4 An example of a PL decay (blue colour) trace of an InGaN/GaN MQW plotted with the instrument response (red colour) and fitted curve based on a bi-exponential decay model (green colour).

3.1.3 Micro-photoluminescence system

A micro-photoluminescence (μ-PL) system provides spatially resolved photoluminescence. Additionally, a high magnification objective (50x) has been installed in the system, allowing the focussing of the excitation laser into a small spot (approximately 2 μm). Thus resulting in high excitation power densities to be achieved. The excitation power density can be varied either by changing the power of the excitation laser or by using absorptive filters in front of the laser beam path. Thus making the system ideal for studying lasing emission mechanism.

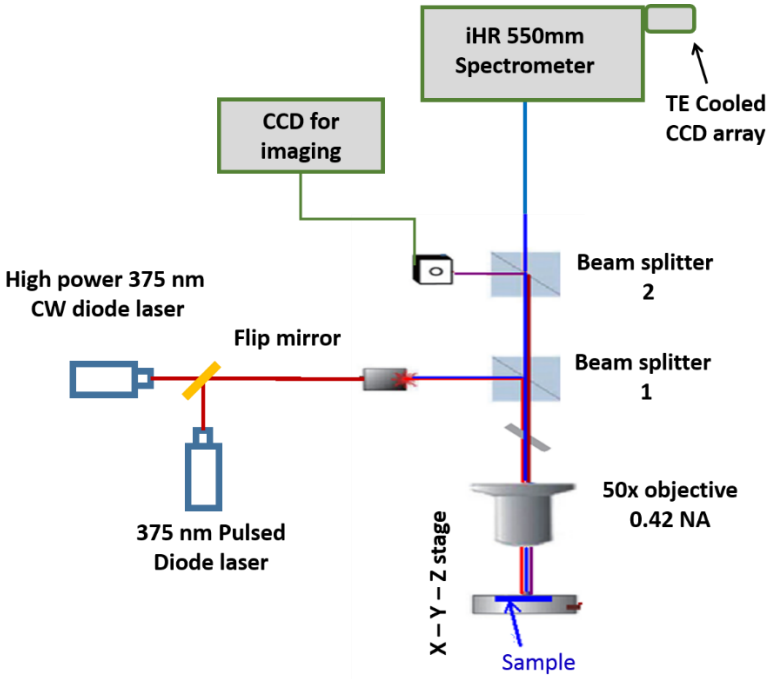

Figure 3.5 Schematic diagram of the micro-photoluminescence system.

Figure 3.5 is a schematic of the µ-PL system. This µ-PL system is also connected to the TRPL system. Therefore, our system could also allow us to perform optical measurements in both spatial and time resolved modes simultaneously. Two kinds of diode lasers are used for this, a 375 nm CW diode laser with an adjustable power of up to 60 mW; and another pulsed 375 nm diode laser with an average power of 1 mW and a pulse width of 50 ps. Switching between the two lasers is achieved by using a flip mirror placed in the lasers beam path. The imaging CCD installed on the system, is used to ensure that the two laser spots are focused on the same position. The laser beam passes through an attenuator which can be continuously changed from ND0 to ND3 in 0.1 intervals, providing a wide range of excitation power densities required. Beam splitter 1 is first used to reflect the laser beam 90˚ through an objective (50x magnification, and 0.42 numerical aperture (NA)). The reflectivity of beam splitter 1 is above 99% at a wavelength of < 412 nm, which minimises the loss of excitation power from the laser. The laser beam can be focussed down to 1.5 µm spot size, which can be estimated using (3.4).

$$d_{spot} = 1.22 \cdot \left(\frac{\lambda_{excit.}}{NA}\right) \quad (3.4)$$

Where NA is the numerical aperture of the objective, and λ is the laser wavelength as an excitation source [5]. In order to further decrease the spot size, a higher magnification objective with higher NA can be used.

The sample is mounted within a Janis microscopy cryostat ST500, which has a continuous liquid nitrogen (or helium) flow. For safety reasons only liquid nitrogen is available, limiting the temperature range from 77 K to 300 K. This type of cryostat can offer vibration isolation on a nanometre scale, which is crucial for the characterisation of nanostructure devices.

The cryostat position is controlled by high resolution X-Y-Z positioners that allow to move the sample position on the order of sub-micro scale.

The luminescence is collected through the same objective and transmitted through beam splitter 1. A second 50-50 power ratio beam splitter (beam splitter 2) is placed in the emission beam path. The first 50% of the transmitted light is directed to a CCD imaging camera to monitor the sample surface. The remaining 50% of the light is coupled to an optical fibre bundle which leads to a 0.55 m long iHR spectrometer to disperse the light. For light detection a -70^{o}C TE cooled CCD array detector is used.

3.1.4 Angular Dependent Photoluminescence System

An angular Dependent PL system is used to measure far-field optical pattern of photonic crystal structure. A schematic diagram of the measurement system used is illustrated in Fig. 3.6. In this system the sample is placed on an XYZ stage which is manually controlled, this allows fine tuning and focusing of sample's position. A cw 405 nm diode laser is used as an excitation source, mounted at a fixed excitation angle.

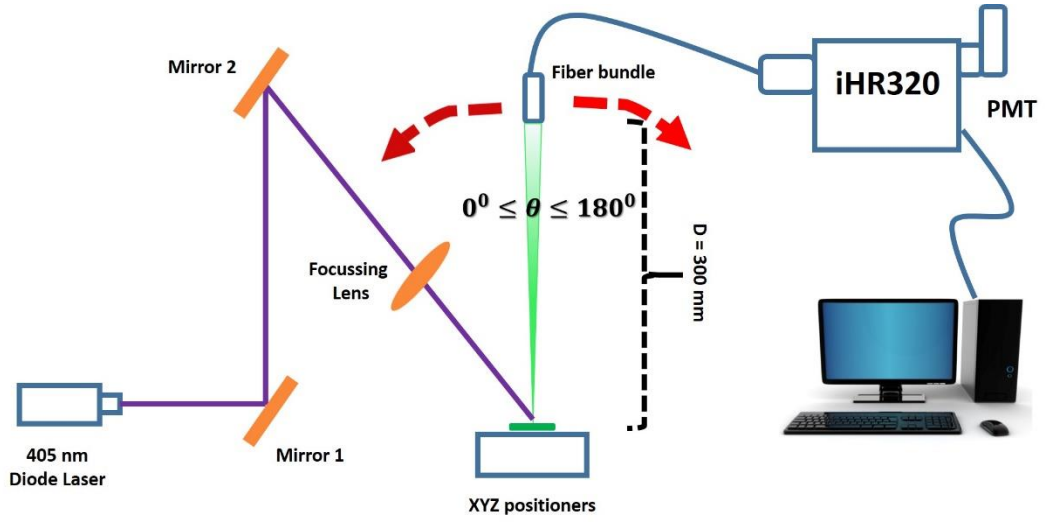

Figure 3.6 Schematic diagram of the angular-resolved photoluminescence system.

The laser beam is reflected through mirror 1 to mirror 2, and mirror 2 then reflects the laser beam on the sample surface. The use of the two mirrors helps to minimise the excitation angle of the laser, thus reducing the stretching effects in the excitation laser spot. A lens is placed in the optical path after mirror 2 in order to focus the laser to an approximate 200 µm spot on samples surface.

The luminescence is collected a 1 mm diameter fibre bundle, which is 300 mm away from samples. The fibre bundle is then attached to a high resolution (0.01°) motorised rotation stage, which will precisely control the collection angle.

The luminescence is then dispersed by a Jobin Yvon monochromator, and detected by a photomultiplier (PMT) detector. The angular resolution of the system is defined by the diameter of the collection fibre and its distance from the sample.

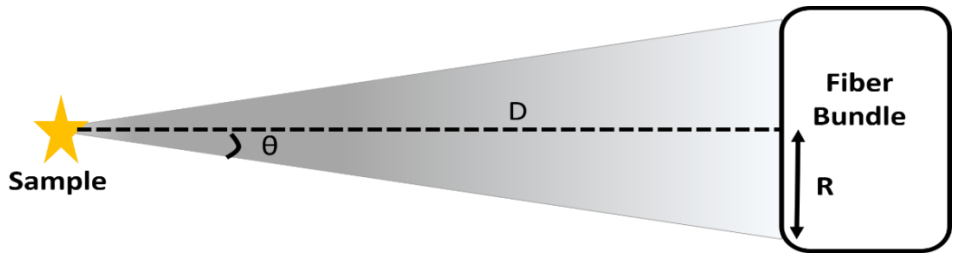

Figure 3.7 Schematic diagram of the angular resolution.

The schematic diagram in Fig. 3.7 illustrates how the angular resolution of the system is determined. In order to resolve fine features in the far-field measurements from the diffracted modes of the PhC arrays, a high angular resolution must be achieved. Using simple trigonometry, based on Pythagoras's theorem, angular resolution is defined as below,

$$\theta = \sin^{-1}\left(\frac{1}{\sqrt{1+\frac{D^2}{R^2}}}\right) \qquad (3.5)$$

Where D corresponds to the distance of the fibre bundle from the sample, and R is the radius of the fibre bundle. Therefore in this system the angular resolution (θ) can be calculated to 0.01°. Unfortunately due to the limitations of the PMT detector measurements are instead performed in steps of 0.5°.

3.1.5 Confocal PL system

In a confocal PL system, the emission collected from the sample is focussed through a pinhole. Any emission from the sample which is not focused on the pinhole is not received by the detector, therefore eliminating any unwanted background emission [6].

A CW 375 nm laser diode coupled on a single mode fibre 2 µm core is used to excite the sample. The single mode fibre acts as the pinhole for the excitation source, which eliminates any unintended light emission and any uniformity problems of the actual laser diode beam profile. The laser is then focused on to the sample through a 100x magnification objective with 0.95 NA. The emission from the sample is then collected through the same objective and focused on to a multi-mode PhC optical fiber with a 10 µm core diameter. The Fibre will again act as a pinhole for the emitted light from the sample. Any light not focused on the fibres aperture will be rejected. The emitted light is then dispersed by a 300 mm Princeton Instruments monochromator, where it is detected by a -60°C TE cooled CCD array detector. The sample is mounted on a XYZ piezoelectric stage with a resolution of approximately 2 nm.

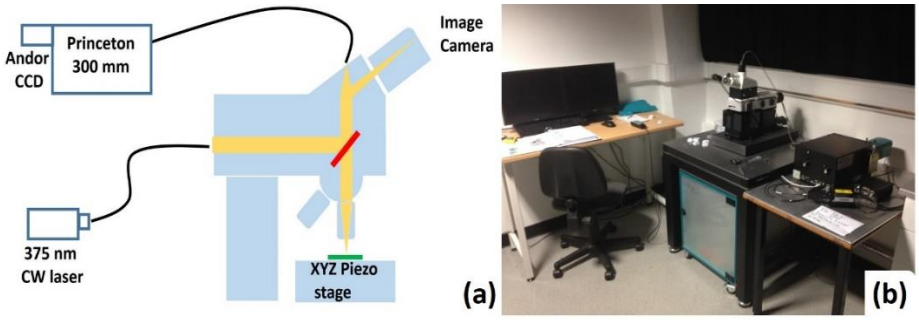

Figure 3.8 (a) Schematic diagram of the confocal system (b) image of a confocal PL system

In Fig. 3.8(a) a schematic diagram of the confocal microscope is illustrated, where a photograph of a confocal system is shown in Fig. 3.8(b). The spatial resolution of the system is given by (3.6) and (3.7) [7] below.

$$\mathrm{FWHM}_{\mathrm{spatial}} = 0.37 \cdot \frac{\lambda'}{\mathrm{NA}} \tag{3.6}$$

$$\lambda' = \sqrt{2} \cdot \frac{\lambda_{\mathrm{excit.}} \cdot \lambda_{\mathrm{emiss.}}}{\sqrt{\lambda_{\mathrm{excit.}}{}^2 + \lambda_{\mathrm{emiss.}}{}^2}} \tag{3.7}$$

Where $\mathrm{FWHM}_{\mathrm{spatial}}$ is the full width half maximum of the system's spatial resolution, λ' is the mean wavelength, $\lambda_{\mathrm{excit.}}$ is wavelength of the excitation source and $\lambda_{\mathrm{emiss.}}$ is the emission wavelength. As can been seen from (3.6) and (3.7) the spatial resolution of the system depends on both the excitation and emission wavelengths. Taking into consideration that the laser used to excite the sample is fixed (375 nm CW) and the emission from the sample is typically around 460 nm, this would give a spatial resolution of approximately 160 nm. Therefore a spatially-resolved PL map could be built up using control software provided by Witec, where a PL spectrum is used spatially every 160 nm. Further processing of the measured data is also applicable, such as the calculation for the FWHM at each step.

3.2 Device Fabrication

The samples used in this study are InGaN/GaN MQWs grown on either (0001) sapphire or (111) silicon by MOCVD and all post fabrication was performed in a high class cleanroom area.

3.2.1 Metal Thin Film Deposition

Metal deposition is performed using an Edwards thermal evaporation system under high vacuum (approximately 10^{-6} mTorr).In such a system a large range of metals can be deposited such as Ni, Au, Ag and Ti. The deposition rate and thickness of the metals can be controlled using a quartz crystal monitor.

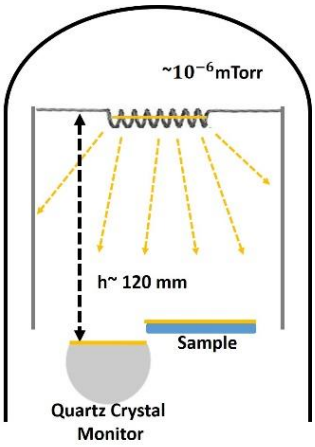

Figure 3.9 Schematic diagram of an Edwards thermal evaporator.

The metals are placed in a tungsten coil at a fixed distance of approximately 120 mm from the quartz crystal monitor. The large distance between the sample and the coil prevents any damage to the sample mask, as the high temperatures of tungsten coil may cause an increase in the temperature of the sample. A high current, normally in the range of tens Amps, is used to heat the tungsten coil, leading the metal to melt and then evaporate.

3.2.2 Dielectric Material Deposition

For the deposition of dielectric materials, such as SiO_2 and SiN, two different techniques have been heavily used in this study, described below.

3.2.2.1 Electron Beam Evaporation

In electron beam evaporation the evaporation of a SiO_2 layer is deposited under high vacuum (approximately 10^{-6} mTorr). An electron beam is focused on a carrier crucible, which contains the dielectric material (SiO_2). The crucible then heats up, which in turn melts the contained SiO_2 for deposition.

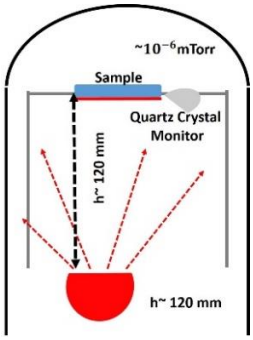

Figure 3.10 Schematic diagram of an Edwards electron beam evaporator.

This system deposits the SiO2 vertically. Vertical deposition has certain advantages when producing nanohole arrays, which will be discussed in Chapter 4.

3.2.2.2 Plasma-Enhanced Chemical Vapour Deposition (PECVD)

Plasma-enhanced chemical vapour deposition (PECVD) is used to deposit dielectric materials such as SiN or SiO_2. The deposition of these materials can be useful for masking purposes in the fabrication of nanostructure devices.

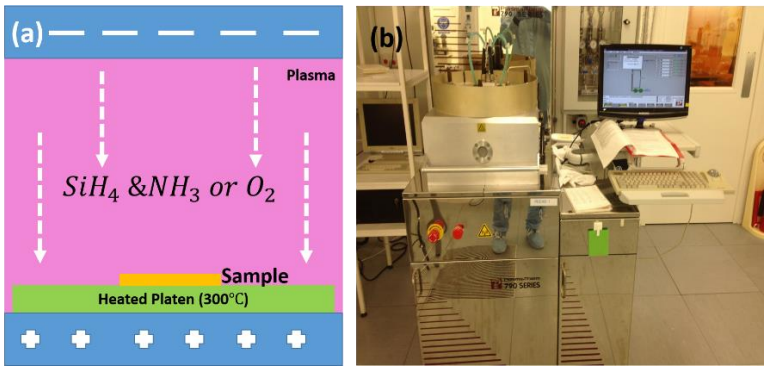

Figure 3.11 (a) Schematic diagram of the PECVD process during deposition of SiN or SiO2 layers; and (b) Image of a Plasma Therm PECVD system.

In order to deposit dielectric materials such as SiO_2 or SiN an appropriate mixture of gases must first be chosen for the process. The sample is placed on a heated plate at 300°C as shown in Fig. 3.11 (a). The deposition of the dielectric materials is conducted by plasma generated using RF power. The deposition rate and thickness can be accurately monitored using ellipsometry. For the system used, the deposition rate for SiN and SiO_2 layers on a flat surface are approximately 10 nm/min and 40 nm/min, respectively. Materials deposited using this technique are normally atomically smooth and robust which can serve as an excellent mask for further processing of our samples.

3.2.3 Dry Etching Techniques

3.2.3.1 Reactive-Ion Etching (RIE)

Due to the resistance of III-Nitrides to wet chemical etching techniques, dry etching methods are often used. The resulting etched surface is highly anisotropic. This is preferable for the post-fabrication of nanostructure devices on as-grown wafers because this can allow the selective etching of the areas required and protection of others [13].

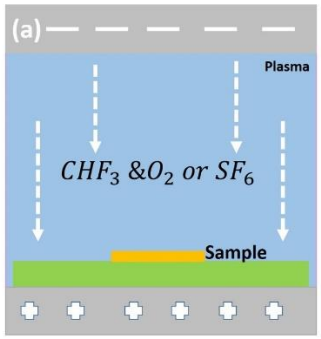

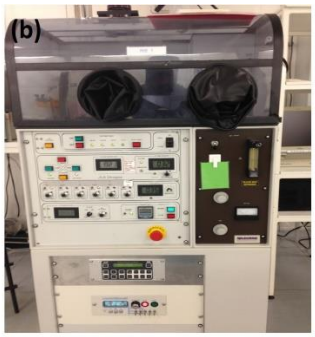

(c)

Etching material	Gasses mixture	Gas flow (sccm)	RF power (W)	Etch rate (nm/min)
SiO_2 or SiN	CHF_3 & SF_6 or O_2	30/10 or 35/5	80	20
Photoresist	O_2	50	150	45

Figure 3.12 (a) schematic diagram of a RIE process; (b) RIE system used in this study; and (c) recipes used for the RIE etching of different materials.

Reactive-ion etching (RIE) is a technique developed to etch through soft materials such as SiO_2, SiN and photoresist. During this process a mixture of etchant gases are used in conjunction with an electromagnetic field that generates plasma. Reactive-ions within the plasma can remove unwanted materials through ion bombardment. Normally the high selectivity of different materials (such as Ni and SiO_2) results in the fabrication of a secondary mask which can act as intermediate step in the post-fabrication of nanostructures. The etching recipes used for different materials are shown in a table in Fig. 3.12(c). By varying the RF power in the recipe the etching rate can be tuned, for example, if a RF power of 150 W is used, the etching rate of SiO_2 can be doubled shown in Table 3.12(c).

3.2.3.2 Inductively Coupled Plasma (ICP) Reactive-Ion Etching

Since III-nitrides are a difficult materials to etch an inductively coupled plasma etching method is also used. In such techniques a higher plasma density can be generated by comparing to standard RIE processing discussed earlier. The ion bombardment generated by the plasma can again removes excess material and etches through GaN layers.

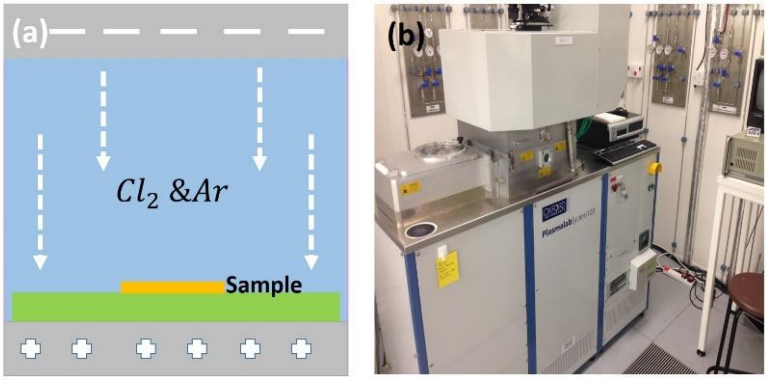

(c)

Etching material	Gasses mixture	Gas flow (sccm)	RF power (W)	Etch rate (nm /min)
GaN	Cl_2 & Ar	45 / 12	50(450 ICP power)	110

Figure 3.13 (a) Schematic diagram of the ICP etching process; (b) Oxford PlasmaPro etching system used; and (c) ICP etching recipe for GaN.

In order to etch through GaN a mixture of Cl_2 and Ar gases are used, as depicted in Fig. 3.13(a). Typically, such etching process is highly selective using dielectric materials as a mask, such as SiO_2, meaning only GaN which is not protected by the masks can be etched away. The etching rate can be precisely controlled by varying the RF applied. Increasing the RF would result in straighter sidewalls as a result of an increase in etching rate, although the ion bombardment itself could result in damage to the exposed InGaN/GaN MQWs active regions [8].

3.2.4 Scanning Electron Microscopy

Fabrication of nanostructure devices requires continuous monitoring of each step to ensure the quality of the sample. A scanning electron microscope (SEM) was used to examine each of the processing steps. The advantages of SEM over traditional optical microscopes are its higher magnification and resolution, which allows us the observation of small features on the samples down to a resolution of 1 nm. It can be considered as one of the most powerful tools in the post-fabrication of nanostructure devices.

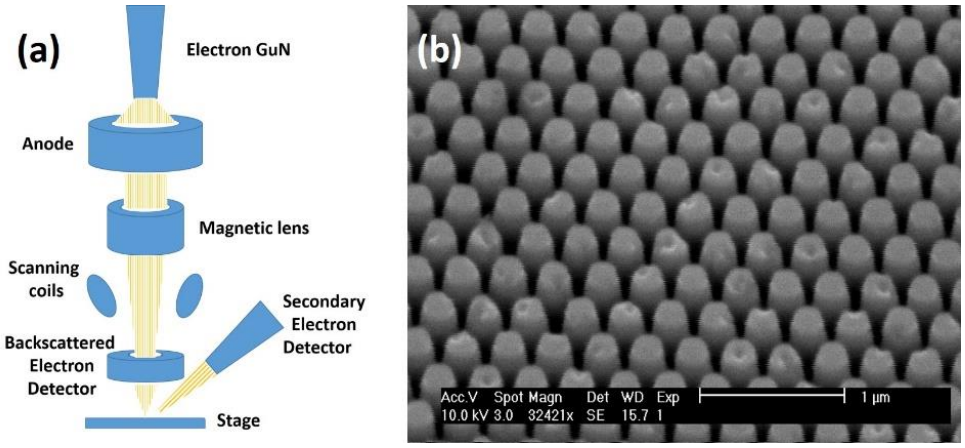

Figure 3.14 (a) Schematic diagram of a SEM [9]; and (b) SEM image of a nanorod array taken with a Philips XL30 FEGSEM.

A schematic illustration of the SEM is given in Fig. 3.14(a). In a SEM an electron beam is generated by an electron gun. Under vacuum, the electron beam travels

in a vertical direction inside the SEM, passing through electromagnetic fields and lenses used to focus the beam onto the sample. When the beam hits the sample electrons, backscattered electrons and X-Rays are generated by the sample due to the interaction of the sample atoms with the electron beam. A secondary electron detector is used to collect this data, which is then translated into signals to generate an image [9]. An example image of a nanorod array fabricated for this study is presented in Fig. 3.14(b), which was taken using a Philips FEGSEM XL30.

3.2.5 Spin Coating Technique

Spin coating is a method of depositing thin films on a sample. In this method a droplet of the desired material is dropped on to the samples surface using a micro-pipette. Centripetal acceleration of the sample stage will cause the solution to be uniformly spread across the sample. Figure 3.15 (a) is a schematic diagram illustrating the spin coating deposition technique of a monolayer of silica nanoparticles; where Fig. 3.15 (b) shows an image taken during the deposition of the same nanoparticles. Silica nanoparticles are employed as a mask for the fabrication of nanostructures in Chapters 4, 5 & 6.

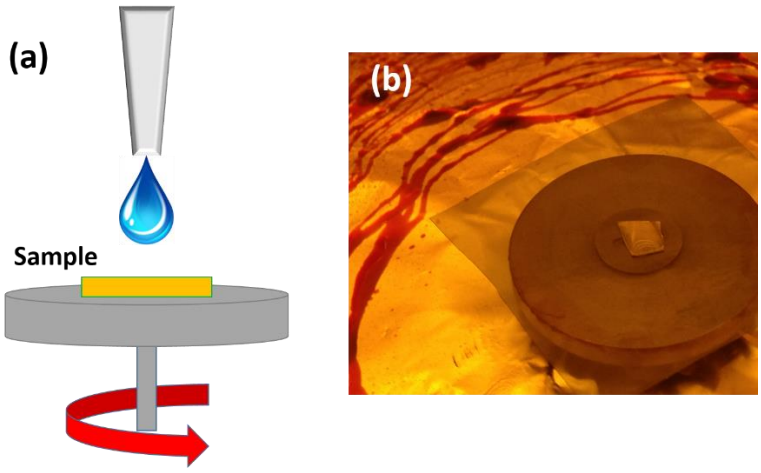

Figure 3.15 (a) Schematic diagram of the spin coating technique (b) image taken of the sample ready to spin during the deposition of Silica nano-particles.

The deposition of the thin film can be modified by variation of spin speed, acceleration and viscosity of the solution used [10]. The simplicity of this technique makes it attractive for thin film applications. In this work the spin coating method has been extensively used for the deposition of monolayers of Silica nanoparticles.

References

[1] S. Perkowitz, *Optical Characterization of Semiconductors,* 1st ed. (London: Academy Press Harcourt Brace&Company, 1993).

[2] N. V. Tkachenko, *Optical Spectroscopy: Methods and Instrumentations*, 1st ed. (Amsterdam: Elsevier B.V., 2006).

[3] S. Chichibu *et al., Phys.Stat. Sol (B)* vol. **234**, p. 746 (2002).

[4] B. Liu, J. Bai, R. Smith, Y. Gong and T. Wang, *Appl. Phys. Lett.,* vol. **103**, p. 101108 (2013).

[5] Pupil Diameter and Beam Spot Diameter of Objective Lens, http://www.olympusims.com/en/microscope/terms/luminous_flux/ [Accessed: 20th October 2014].

[6] Laser scanning confocal microscopy, http://www.olympusconfocal.com/theory/LSCMIntro.pdf [Accessed: 20th October 2014].

[7] S. Wilhelm, B. Gröbler, M. Gluch and H. Heinz, *Confocal Laser Scanning Microscopy*, http://zeiss-campus.magnet.fsu.edu/referencelibrary/pdfs/ZeissConfocalPrinciples.pdf [Accessed: 21st October 2014].

[8] H. Morkoç, *Handbook of Nitride Semiconductors and Devices,Electronic and Optical Processes in Nitrides* , 1st ed. (John Wiley & Sons, 2009).

[9] Scanning Electron Microscope, http://www.purdue.edu/ehps/rem/rs/sem.htm [Accessed: 21st October 2014].

[10] T. Ogi, L. B. Modesto-Lopez, F. Iskandar and K. Okuyama, *Colloids Surf. (A)* vol. **297**, p. 71 (2007).

[11] Z. Wan-Ru *et al., Chin. Phys. Lett.* vol. **31**, p. 114205 (2014).

[12] Y. H. Cho *et al., Appl. Phys. Lett.* vol. **73**, p. 1370 (1998).

[13] I. Adesida *et al., MRS. Symp. Proc.* vol. **537**, p. G1.4 (1998).

CHAPTER 4

Fabrication of Two-Dimensional InGaN/GaN Photonic Crystal Structures Using a Modified Nanosphere Lithography Technique

By means of combining a very cost-effective lift-off process and a nanosphere lithography technique [1-4], we have fabricated two dimensional (2D) photonic crystal (PhC) structures on an InGaN/GaN multiple quantum well structure [5]. Significant enhancement in photoluminescence (PL) intensity has been observed when the emission wavelength is within the photonic bandgap. Time-resolved PL measurements have shown that the spontaneous emission rate is strongly reduced by a factor of 4 due to the PhC effect. As a consequence, the emission intensity along 2D PhC slab-plane directions is effectively suppressed and redistributed to the direction normal to the 2D PhC slab-plane simultaneously. Temperature-dependent PL measurements have confirmed that the enhanced PL intensity is due to an increase in extraction efficiency as a result of the PhC effect.

4.1 Introduction

One of the major problem that GaN based LED devices suffer, is the low extraction efficiency of light generated by the recombination of electron-hole pairs as is being trapped inside the device. This phenomenon occurs due to large refractive index difference of GaN (n_{GaN}=2.5) and air (n_{air}=1) .A number of techniques such as making the surface of the sample rough [6, 7], textured surface [8, 9] and tuneable shape devices [10] have been proposed in order to increase extraction

efficiency. However, there is a major drawback to these approaches as a result of lack of accurate control over the directionality of the light emitted from the LEDs [6-10].

Recently photonic crystal structures (PhC) have been employed on III-Ntirdes based LEDs, for increasing the extraction efficiency [11-14]. PhC are periodic arrays of nanostructures, where the refractive index is varied at least in one direction. One of the major benefits of PhC structures is they can control the directionality of the light [11], as well as controlling the spontaneous emission in a device. The spontaneous emission can be control by the modification of photonic density of state (DoS), by the introduction of photonic bandgaps, as discussed in earlier Chapter 2 [12-14]. Two-dimensional (2D) PhC structures have been utilized in the fabrication of advanced III-nitride based LEDs, leading to a significant improvement in light extraction due to the PhC effect [15].

In order for the optical modes to be efficiently extracted out of the device the physical period of the PhC structure must be on the order of half a wavelength. For example, a PBG for wavelengths in the blue spectrum region (450 nm) can be introduced, when the PhC lattice has period of approximately 220 nm. As a result of that, the fabrication of PhC structures in the visible range of the electromagnetic spectrum can be considered as a major constrain. This is due to limited resolution (approximately 1 μm) of standard optical lithography technique. Electron beam lithography (EBL) techniques remain the most popular approach in the fabrication of PhC structures [14]. However, EBL is very time-consuming and so is not cost-effective, using EBL only PhC structures with small areas (typically a few microns) can be normally fabricated, which is not attractive to industry. Alternate methods have also been developed, such as nano-imprint lithography [15]. In nano-imprinting lithography technique, EBL is used to write the required pattern on Si wafers which will be then used as the rigid mask for patterning the wafers. Unfortunately the limited lifetime of Si mask (approximately 10 to 15 times), as it tends to be fragile and the initial cost of the

mask renders the use of this technique inappropriate. Therefore it is desirable to develop a cost-effective method of fabricating PhC structures.

4.2 Characterisation of the As-Grown Sample

A standard five periods of InGaN/GaN multiple quantum well (MQW) sample was used to fabricate PhC structures. The sample was grown on c-plane (0001) sapphire by MOCVD using a high temperature AlN buffer technology, which leads to enhanced crystal quality compared with the widely used two-step growth approach [16]. The detailed structure of the sample is schematically illustrated in Fig 4.1(a).

Before the growth of the InGaN/GaN MQWs a high temperature 0.5 µm atomically flat AlN buffer layer was grown directly on sapphire, followed by a 1.2 µm thick GaN buffer layer. Afterwards, MQWs with a 10 nm capping layer were grown.

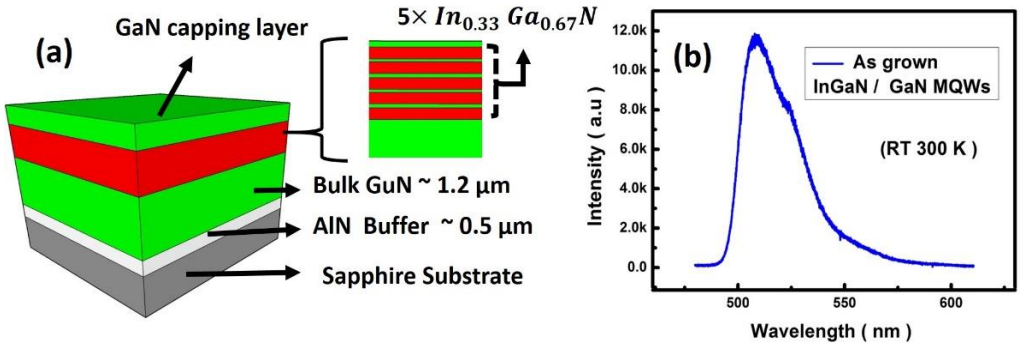

Figure 4.1 (a) Structure of the as-grown sample (b) Room temperature PL of the as-grown sample used for this work.

Figure 4.1(b) shows the PL spectrum of the as-grown sample measured at room temperature using a CW 375 nm diode laser as an excitation source, displaying a peak emission at 510 nm. The surface morphology was examined by atomic force microscopy (AFM) as shown in Fig. 4.2.

The AFM image of the InGaN/GaN MQWs as-grown sample shows a number of "v" pits, which are the typical features for InGaN structures with a high indium composition. The "v-pits", appears due to the lattice mismatch between the

InGaN QWs with the underlying GaN layers. The problem becomes even worse when the In composition increase, hence the lattice mismatch increases as well [27].

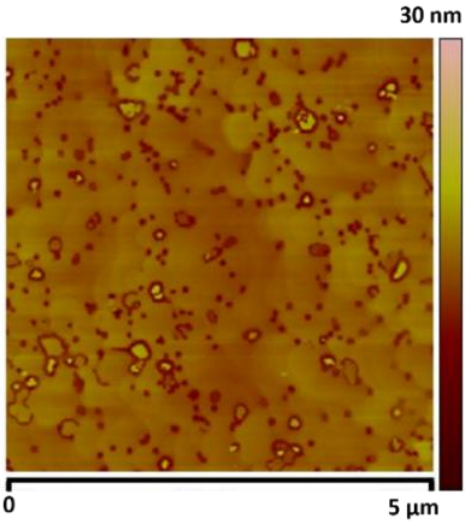

Figure 4.2 AFM images of the InGaN/GaN MQW as-grown sample

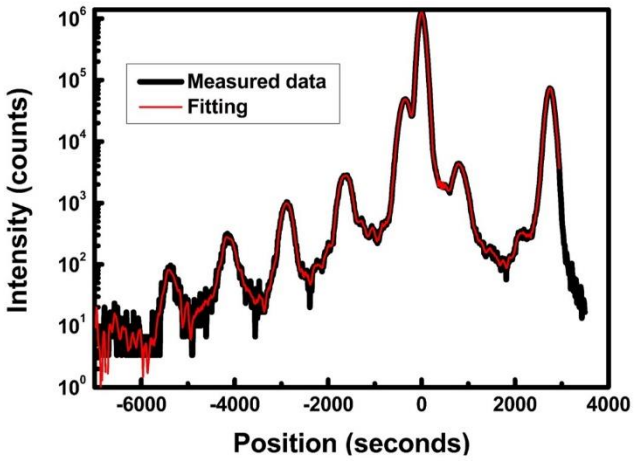

Figure 4.3 XRD spectrum of the as-grown sample scanned in a ω - 2Θ mode: black lines are the measured curve, and the red lines are the fitted data.

Material	InN mole fraction	Thickness (nm)	Period
InGaN Quantum Well	33 %	2	5
GaN Quantum barrier	0	11.2	5

Table 4.1 Simulation data used to model XRD ω – 2θ scan.

X-ray diffraction measurements have been performed in a ω - 2Θ mode in order to estimate the indium composition, quantum well and barrier thicknesses by using the fitting data. Figure 4.3 shows the XRD spectrum scanned in a typical ω - 2Θ mode and the fitted data, in black and red respectively, indicating the indium composition of 33% for the quantum wells. The thickness of quantum well and barriers are 2 nm and 11.2 nm, respectively.

4.3 Fabrication of Nanohole Photonic Crystal Arrays

A schematic diagram of the fabrication procedure is presented in Fig. 4.4.

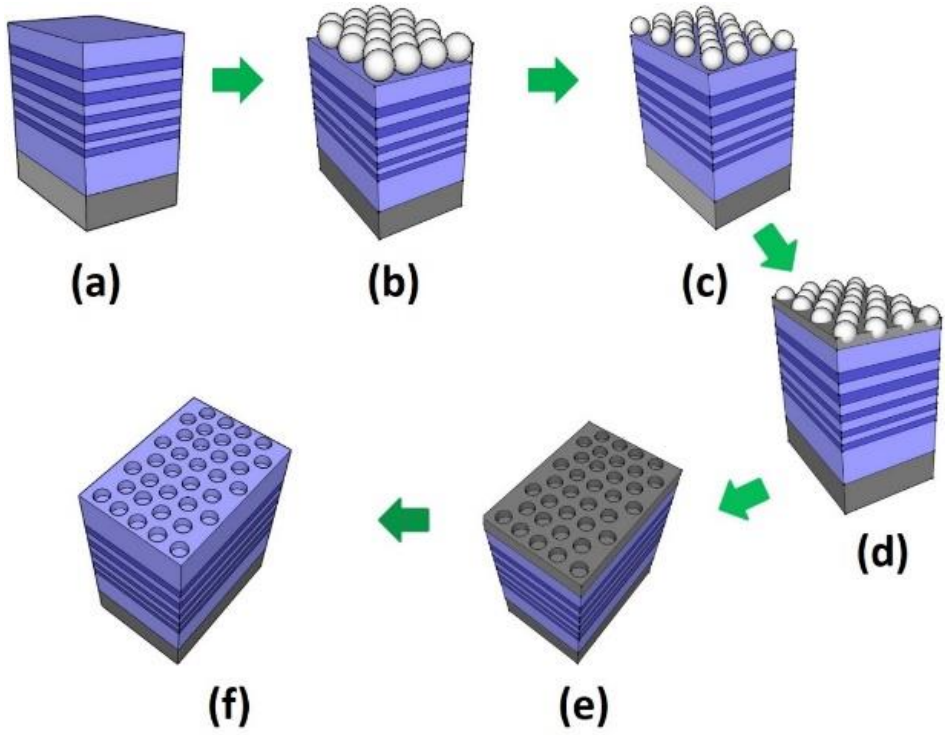

Figure 4.4 Schematic diagram presentation the fabrication of PhC nanohole arrays using nanosphere lithography.

The samples were first cleaned sequentially using n-butyl acetate, acetone and IPA in order to degrease and remove any unwanted dust particles on the sample. The as-grown sample was then subjected to a chemical surface treatment for 20 minutes using hydrogen peroxide (H_2O_2) and sulphuric acid (H_2SO_4) with a 1:1

volume concentration. This causes the GaN surface to become hydrophilic. This will help the silica nanosphere uniformly distribute across the surface [17].

Silica nanospheres with a diameter of 270 nm diluted in de-ionized (DI) water were then spin-coated on the surface of the InGaN/GaN MQW sample in order to form a monolayer of silica nanospheres, as schematically illustrated in Fig. 4.4(b). Subsequently the monolayer of silica nanospheres undergoes a selective etching process (etching the silica nanospheres but not the GaN underneath) to set both the separation between nanospheres and diameter of the silica nanospheres as in Fig. 4.4(c). This will act as the first mask in the fabrication of the PhC structure. Controlling the size of the nanospheres allows the photonic bandgap of the designed PhC structure to match the emission wavelength of the InGaN/GaN MQWs.

Then, taking advantage of the vertical deposition of the e-beam evaporator as the SiO_2 can only be deposited on GaN surface in the gaps between the spheres. A thin silicon dioxide layer (60-70 nm) is deposited, as shown in Fig. 4.4(d). Then by using a low adhesive tape, the silica nanospheres are simply lifted off; leaving intact the silicon dioxide layer in the gaps of the silica nanospheres on the samples surface, see Fig. 4.5(e). Finally, this remaining silicon dioxide layer then acts as a mask for further etching of the InGaN/GaN MQW sample that ultimately gives a hexagonal 2D PhC structure, as in Fig. 4.4(f). The residues of silicon dioxide are removed by immersing the sample in hydrofluoric acid (HF).

In Fig. 4.5 SEM images show each step in the fabrication of the final 2D PhC InGaN/GaN MQW structure, as detailed above. The samples have been etched down through the whole InGaN/GaN MQW region, where the depth of the fabricated nanoholes is approximately 200 nm.

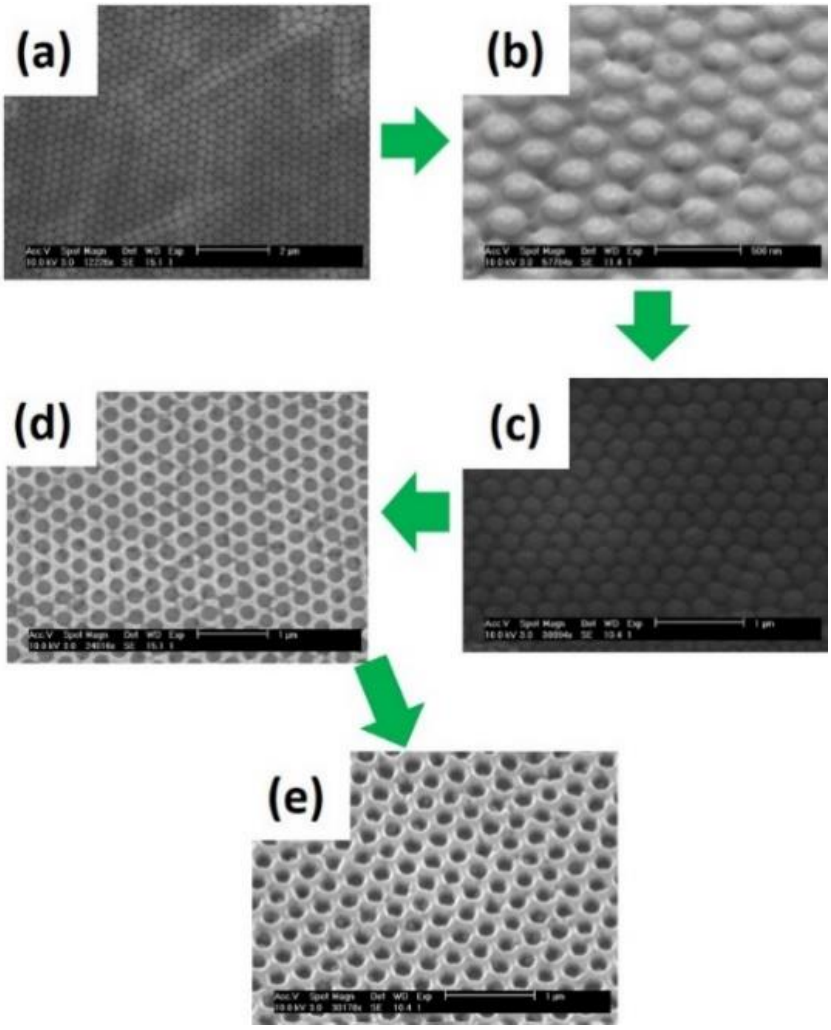

Figure 4.5 SEM images of each individual step of the fabrication procedure as detailed in the corresponding schematic diagram depicted in Fig. 4.4.

4.3.1 Nanosphere Deposition

4.3.1.1 Spin Speed Optimisation

For the deposition of 270nm diameter nanospheres, the silica particles were diluted in de-ionised water (DI) with a 10 % concentration of silica particles to DI water. The solution was then placed in an ultrasonic bath for approximately 1 hour to mix the particles in the DI water and avoid to form clustering of particles on the samples surface.

In Fig. 4.6, the rotation speed of the spin-coating was varied in order to optimise the spin speed conditions. At low speeds (such as 1500 rpm), as shown in

Figure 4.6(a) the sample was covered by a multilayer of the silica nanospheres. The speed was then further increased to 2300 rpm, as shown in Fig. 4.6(b) a monolayer of closely packed hexagonal array particles were formed on the surface of the InGaN/GaN MQWs.

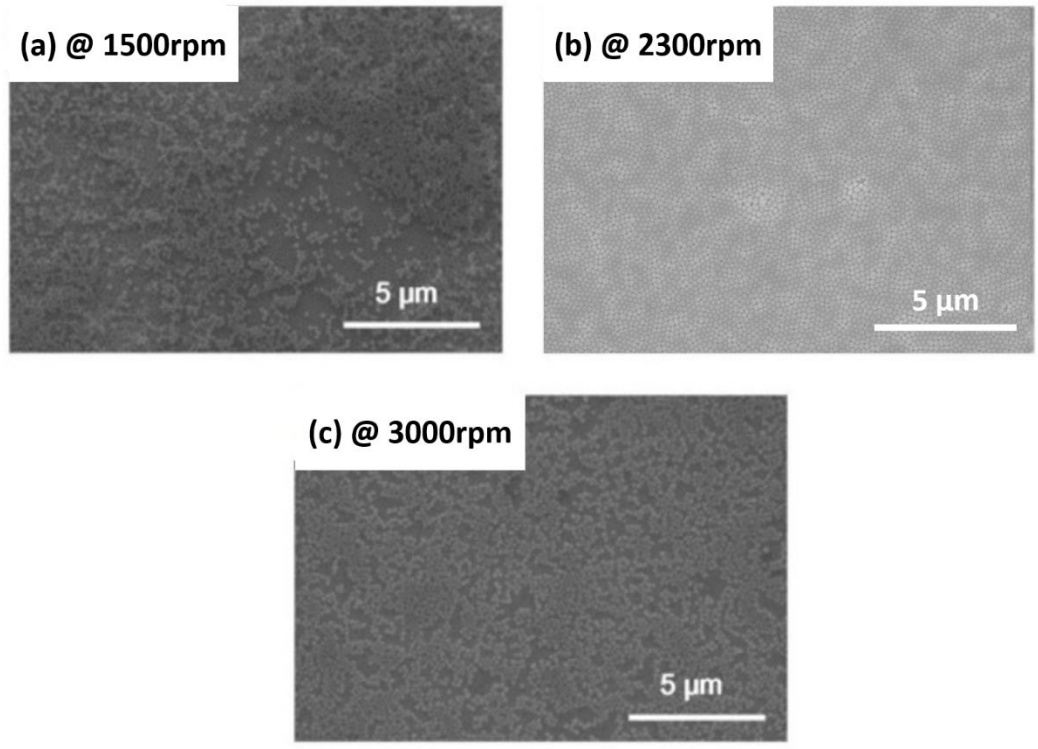

Figure 4.6 SEM images of silica nanospheres deposited on InGaN /Gan MQWs at (a) 1500rpm, (b) 2300 rpm and (c) 3000 rpm.

Further increasing to 3000 rpm leads to a disordered array with gaps as shown Fig. 4.6(c). The optimum spinning speed was therefore found to be 2300 rpm.

4.3.1.2 Sodium Dodecyl Sulphate (SDS) Conditions Optimisation

In order to reduce the molecular adsorption between the nanospheres and the sample surface, sodium dodecyl sulphate (SDS) was mixed with the 10% Silica in DI water. Figure 4.7 shows top down SEM images, demonstrating the effects of the SDS as a surfactant. The deposition on both samples was performed under identical spinning conditions (2300 rpm).

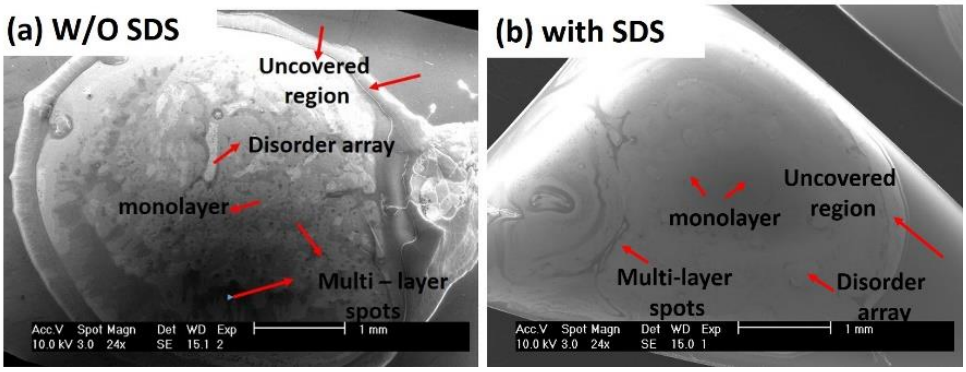

Figure 4.7 Large scale top view SEM images illustrating coverage (a) without SDS surfactant and (b) with SDS surfactant.

The SEM in Fig. 4.7 (a) shows a mixed image of the sample prepared without SDS, indicating close-packed monolayers (grey), disorder (light grey) and multilayer areas (dark spots). The use of the SDS solution leads to achieving a monolayer in a large area, as observed in Fig. 4.7(b). Some dark spots observed near the edge of the sample can be attributed to an edge effect. Edge effects are normally observed, as the silica solution flows uniformly outward the sample during the spin coating process, but it forms droplets at the edges of the sample in order to be flung off. Thus depending on the surface tension, viscosity, rotation rate etc. [26].

The optimisation of the SDS concentration with respect to the silica solution was carried out and the results are presented in Fig. 4.8. The SEM image in Fig. 4.8(a) shows a top down view of the sample with the ratio of SDS to silica and DI water solution at a 1:10. Under these conditions a dispersed monolayer of nanoparticles is formed with large gaps. Decreasing the quantity of SDS solution to the silica solution to a ratio of 1:50 a monolayer of nanospheres was achieved, as shown in Fig. 4.8(b). Despite the dramatic decrease in uncovered areas, some small gaps can still be observed. The optimum condition was found to be a 1:100 concentration of SDS to Silica solution. The resulting monolayer of closely packed nanoparticles is presented in Fig. 4.8(c).

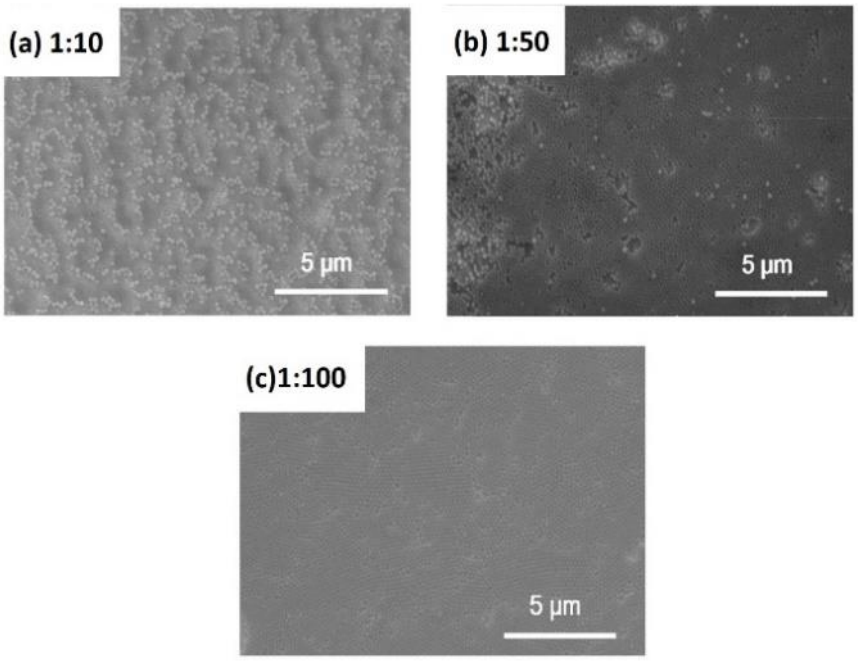

Figure 4.8 SEM images of nanospheres spin coated on InGaN/GaN MQWs at 2300 rpm under different ratios of SDS solution to Silica nanospheres (a) 1:10, (b) 1:50 and (c) 1:100.

4.3.2 RIE Etching Optimisation

In order to select the diameter to match the photonic bandgap required for the emission wavelength studied, reactive-ion etching (RIE) techniques were employed. The ability to selectively etch the silica nanospheres is examined by tuning the etching time. Figure 4.9(a)-(c) shows the SEM images for silica particles, undergoing RIE etching for 4, 5 and 7 minutes respectively. The measured diameters of the nanoshperes were found to be approximately 210, 180 and 160 nm respectively. Therefore the lateral etching rate for the silica nanospheres is roughly estimated to be 12 nm/minute. Because of the spherical geometry of nanospheres the etching rate of the particles differs in the lateral and vertical direction.

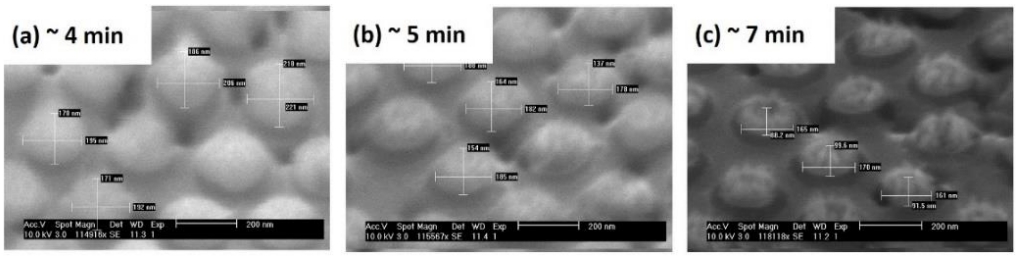

Material to etch	Gasses (sccm)	RF power (W)	Vertical etch rate (nm / min)	Lateral etch rate (nm /min)
Silica spheres	$CHF_3 : O_2\ (35:5)$	80	18-20	12

Figure 4.9 SEM images at a 30° tilt angle, varying the etching time between (a) 4 minutes, (b) 5 minutes and (c) 7 minutes.

The etch rate was found to be approximately 20nm/min in the vertical direction and 12nm/min in the lateral direction.

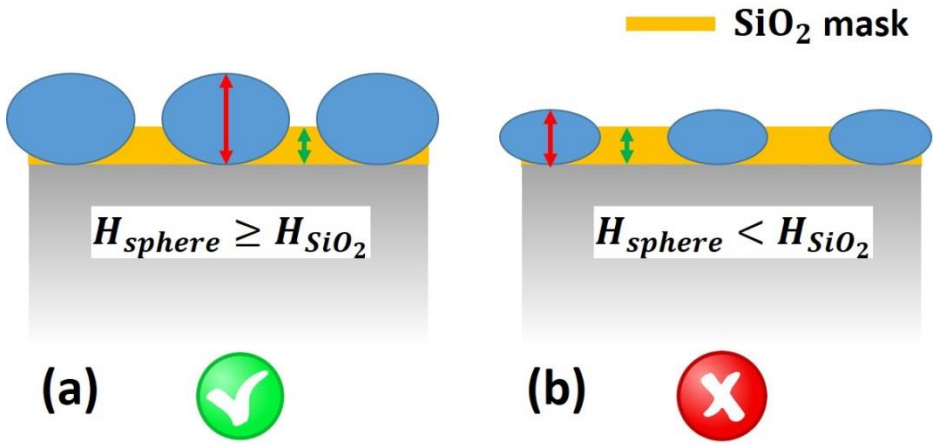

Figure 4.10 Schematic representation of (a) silica particles that are not trapped under SiO2 mask and (b) silica particles trapped under the SiO2 layer deposited on top. Red arrows represents the height of the spheres and green arrows represent the thickness of the spheres and green arrows represent the thickness of the SiO2 mask.

Increasing the etching time causes the diameter of the particles to decrease (more-so in the vertical direction than the horizontal). Particles can become trapped under the silicon dioxide (SiO_2) mask. Therefore, there exist a limit on further reducing the diameter using this RIE etching method. The "trapping" mechanism of nanospheres under the SiO_2 layer, can be observed when the

height of sphere (red arrows) is smaller than the height of the SiO_2 spheres (green arrows), as Fig. 4.10 schematically illustrates.

4.3.3 Lift-off and SiO_2 Deposition Optimisatio

The next step in the fabrication of the nanohole array as a PhC was the deposition of silicon dioxide, followed by the lift-off of the nanospheres. After selecting the size of the spheres using the RIE etching, a thin silicon dioxide layer (approximately 60 - 70 nm) was deposited covering the nanospheres and filling the gaps between them.

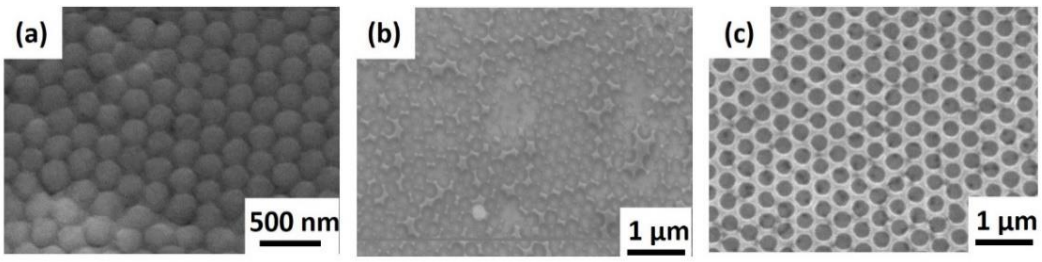

Figure 4.11 SEM images after (a) SiO2 deposition (b) lift-off using ultrasonic bath (c) lift-off with blue tape.

Figure 4.11(a) is an SEM image of the InGaN/GaN MQWs sample after the SiO_2 deposition. Depositing SiO_2 on the top of the spheres is one of the most critical steps during the fabrication procedure. The SiO_2 layer will act as a secondary mask for further etching through the MQWs. Therefore a thick layer is desirable in order to withstand the ICP dry etching process and protect the underlying heterostructure. However, depositing a layer with a thickness exceeding 100 nm (for the 140 nm nanospheres) would result in trapping the spheres under the SiO_2 layer, as they cannot be lifted-off. The optimal thickness of the secondary mask was found to be approximately 60 - 70 nm.

The nanosphere lift-off process was achieved with the use of a standard blue tape. Figure 4.11 (b) and (c) shows the nanosphere lift-off process using an ultrasonic bath and a standard blue tape, respectively. The use of the ultrasonic bath cause severe damage the nanomask due to the strong vibrations, causing the mask left to be completely destroyed. In this case, simply using a low adhesive tape and

applying a slight pressure down on the sample surface, was sufficient to adhere the nano-spheres to the tape and allowing lift-off. This left behind an excellent hexagonal PhC arrao of SiO_2 nano-holes.

4.3.4 ICP Dry Etching Optimisation

The thin SiO_2 secondary mask is used to selectively etch into the PhC nanohole. Optimisation of the ICP dry etching conditions is the next step in the transferring the 2D PhC mask into the InGaN MQW sample.

Figure 4.12 (a)–(c) shows top down SEM images after ICP dry etching through the InGaN/GaN MQWs with different RF powers at 100, 50 and 30 W respectively. Although there is good etching selectivity between GaN/SiO_2, the bombardment of Ar ions can cause sputtering of the SiO_2 mask. RF powers of 100 W and 50 W, as seen in Fig. 4.12 (a) and (b), tend to be catastrophic as the mask cannot withstand the etching for long time and therefore cannot protect the underlying GaN layer.

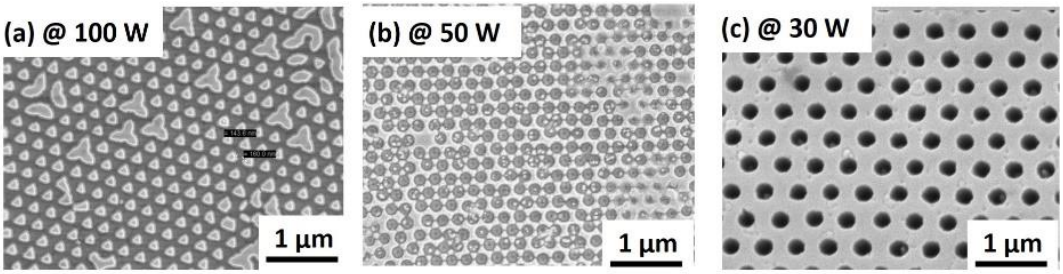

Material to etch	Gasses (sccm)	RF power (W)	Etching rate (nm/min)	Mask Condition
InGaN / GaN MQWs	$Cl_2 : Ar\ (45 : 12\ )$	100	-	×
InGaN / GaN MQWs	$Cl_2 : Ar\ (45 : 12\ )$	50	-	×
InGaN / GaN MQWs	$Cl_2 : Ar\ (45 : 12\ )$	30	80	√

Figure 4.12 ICP optimisation of etching conditions by varying the RF power (a) 100 W (b) 50 W and (c) 30 W; the table presents the ICP recipes used in the etching process.

Decreasing the RF power to 30 W results in significant improvement, as observed in Fig. 4.12 (c).

4.4 Mode Extraction

This study concentrates mainly on the effects of two-dimensional photonic crystals structures created using simplified fabrication techniques. A schematic illustration of an unpatterned sample and a 2D-PhC are shown Fig. 4.13(a) and (b), respectively. Due to the refractive index difference at the GaN / air interface, an unpatterned structure shown in Fig. 4.13 (a), can support the formation of slab modes [17-20]. Since guided modes behave like waves, each wave therefore appears to have an in-plane wave vector(k_{II}).

Figure 4.13(b) shows the propagation of low-order (k_{II1}) and high-order (k_{II2}) guided mode. The guided modes will interact with the photonic crystal and eventually their propagation in the x-y plane will be suppressed before being redirected in the vertical direction, where they can escape into air [18].

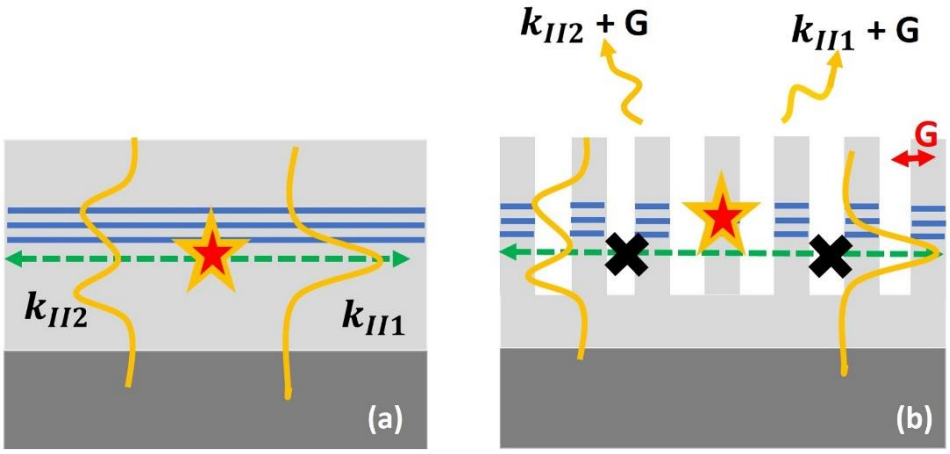

Figure 4.13 Slab wave guiding model illustrating the (a) formation and propagation of slab modes in an unpatterned sample and (b) inhibition and redistribution of the slab modes in the vertical direction of a 2D PhC array [18, 19].

The in-plane wave vector of each guided mode, is given by (4.1) below.

$$k_{II,m} = (\frac{2\pi}{\lambda})n_{GaN}\sin(\theta_m) \approx \sqrt{[\left(\frac{2\pi}{\lambda}n_{GaN}\right)^2 - \left(\frac{m\pi}{L}\right)^2]} \qquad (4.1)$$

Where n_{GaN} is the refractive index of GaN; m is the mode number, which is an integer; λ is the wavelength of the light propagating in the PhC; and L is the thickness of the GaN epilayer [18].

Any periodic structure like 2D photonic crystals can be described by the reciprocal lattice whose vectors (G) couple harmonics of the light propagating through the photonic crystal. Photonic crystals couple the guided modes, therefore the guided modes are now becoming Bloch modes which are also known as leaky modes as they leak outside the device into the air [18, 19]. The wave vector of each guided mode are now coupled to the reciprocal lattice vectors as shown in (4.2).

$$k_{II} + G \tag{4.2}$$

Where G is the reciprocal lattice vector. According to Bragg's law the guided modes are diffracted to air if the condition in (4.3) is satisfied.

$$|k_{II} + pG_0| < \frac{2\pi}{\lambda} \tag{4.3}$$

Where p is an integer that determines the harmonic responsible for the diffraction of the guided mode into air.

$$G_0 = \frac{2\pi}{\alpha} \tag{4.4}$$

Where α is the photonic crystal lattice constant. In the case where the magnitude of the in-plane wave vector (k_{II}) of the mode is larger than the in-plane projection of the air-cone then the mode remains trapped inside the device [18, 19]. The in-plane projection of the air-cone is defined as a circle of radius ($k_0 = \frac{2\pi}{\lambda}$). The mode is then either lost through a collision within the crystal or reabsorbed within the quantum wells [18, 19].

After coupling to the photonic crystal reciprocal lattice, are diffracted outside the device into the air. The extraction of guided modes depends on the type of lattice constant (e.g. hexagonal, square) and the propagation of the guided modes inside the device. As shown in (4.1), LED devices can typically support several tens of modes depending on the thickness of the device [17, 18]. In order to maximize

the extraction of as many guided modes as possible, the guided modes propagating in any direction in the (2D) plane interact with the photonic crystal. Therefore 2D-PhCs with a hexagonal lattice are preferred compared to square lattice PhCs, due to their high degree of periodicity, which can effectively increase the interaction of the slab modes with the PhC.

4.5 Simulation and Design of 2D PhC Array of Nanoholes

Figure 4.14 (a) illustrates the structural characteristics of the 2D PhC. The PhC lattice constant is defined by *α,* where *D* corresponds to the nanohole diameter. The refractive index for simulation purposes is 2.5, as illustrated in the contour map in Fig. 4.14(b).

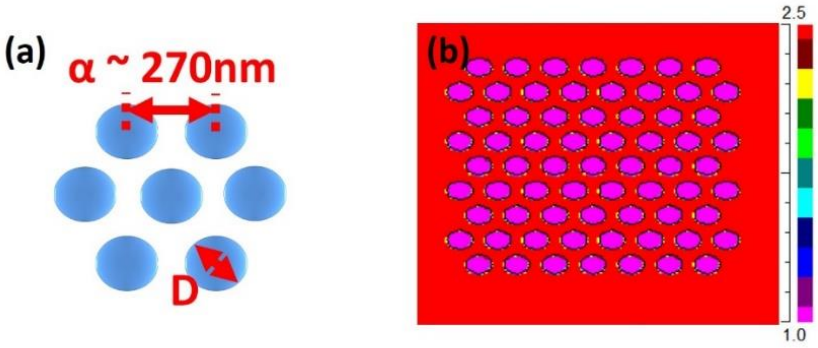

Figure 4.14 (a) Dimensions of the PhC array of nanoholes and (b) contour map presenting the refractive index variation across the 2D PhC array of nanoholes.

In Fig. 4.15(a) the photonic bandgap (PBG) map for the TE emission is plotted against the nanohole diameter. The red circles indicates the diameter of the nanoholes at which the spontaneous emission matched the photonic bandgap. The blue lines on the PBG map indicates the range of emission energies at which the photonic density of states is 0. A PBG is therefore induced for those energies.

The diameter of the nanoholes was varied from 50 up to 270 nm, in 10 nm steps, to find the spontaneous emission from the InGaN/GaN MQW sample that matched the induced photonic bandgap.

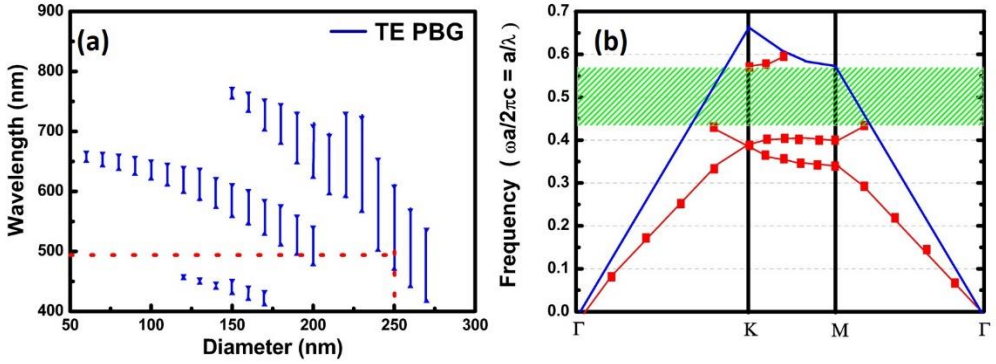

Figure 4.15 (a) Photonic bandgap as a function of the nanohole diameter; (b) photonic band structure of the 2D PhC structure with a 250nm nanohole diameter.

To investigate the PhC effect four samples were fabricated with nanohole diameters of 150 nm, 190 nm, 220 nm and 250 nm. Only the emission from the sample with a 250 nm nanohole diameter lies within the photonic bandgap, and also covers a wide range of PBG from 482 nm to 613 nm. The simulated photonic band structure is plotted in Fig. 4.15(b) for nanoholes with a 250 nm diameter. This figure indicates there is a clear photonic bandgap, corresponding to the frequencies between 0.44 and 0.56 (α/λ), namely, between 482 and 613 nm in terms of wavelengths. Figure 4.15(a) also manifests that the 500 nm emission wavelength requested for the InGaN/GaN MQW sample lies outside the PBGs of the 2D PhC structures with nanohole diameters of 150, 190 and 220 nm.

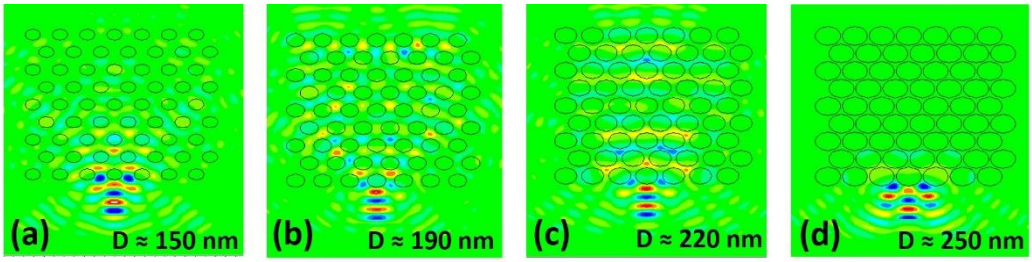

Figure 4.16 FDTD simulation of the light propagating in the xy-plane for nanoholes with diameter (a) 150 nm, (b) 190 nm, (c) 220 nm and (d) 250 nm.

Finite-difference time–domain (FDTD) simulations were carried out in order to examine the propagation of the light as it travels in the xy-plane of the PhC. Figure 4.16 (a)-(d), shows the propagation of the light as it travels in the xy-plane for nanoholes with diameters 150, 190, 220 and 250 nm respectively. A dipole emitting at 500 nm was 1 µm from the 2D PhC arrays. It can be seen that for nanoholes with a diameter of 150, 190 and 220 nm the light propagates through the PhC. In the case of the 250 nm nanohole diameter the photonic bandgap introduced by the PhC prevents any propagation of the light through it. This phenomenon is caused by the matched photonic bandgap to the dipole emission.

4.6 Optical Investigation of the PhC Nanohole Arrays

Figure 4.17(a)-(d) top-view SEM images of the fabricated samples are presented, with nanohole diameters of 150, 190, 220 and 250nm respectively. It can be seen hexagonal 2D PhC arrays were fabricated with a relatively high uniformity. Some slight variation in the size of the nanoholes arises due to a ±10% variation in the diameter of the nanospheres used.

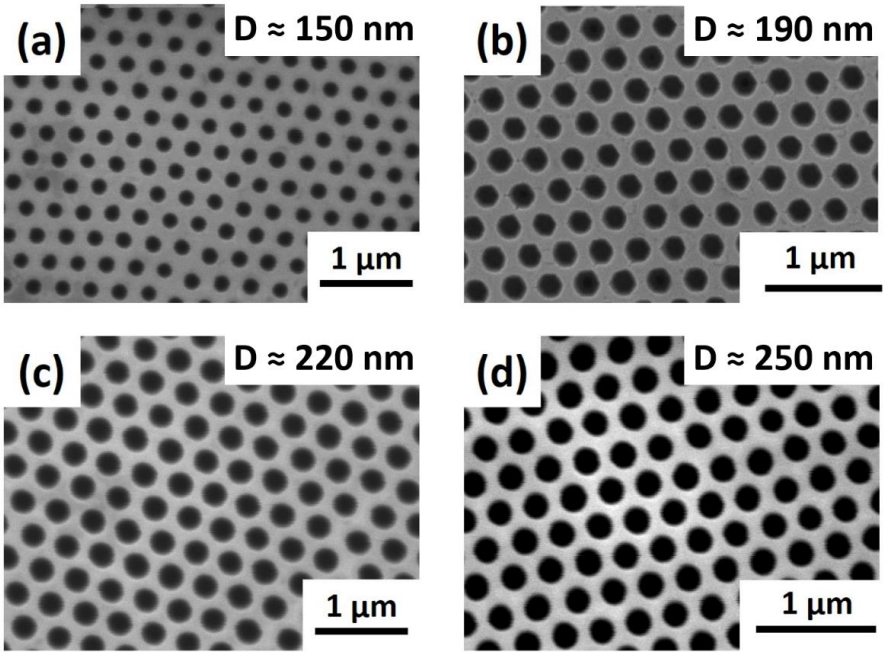

Figure 4.17 Top view SEM images of the fabricated samples with a 270 nm lattice constant and diameters of (a) 150 nm, (b) 190 nm (c) 220 nm and (d) 250 nm.

4.6.1 Photoluminescence Measurements of the 2D-PhC Samples

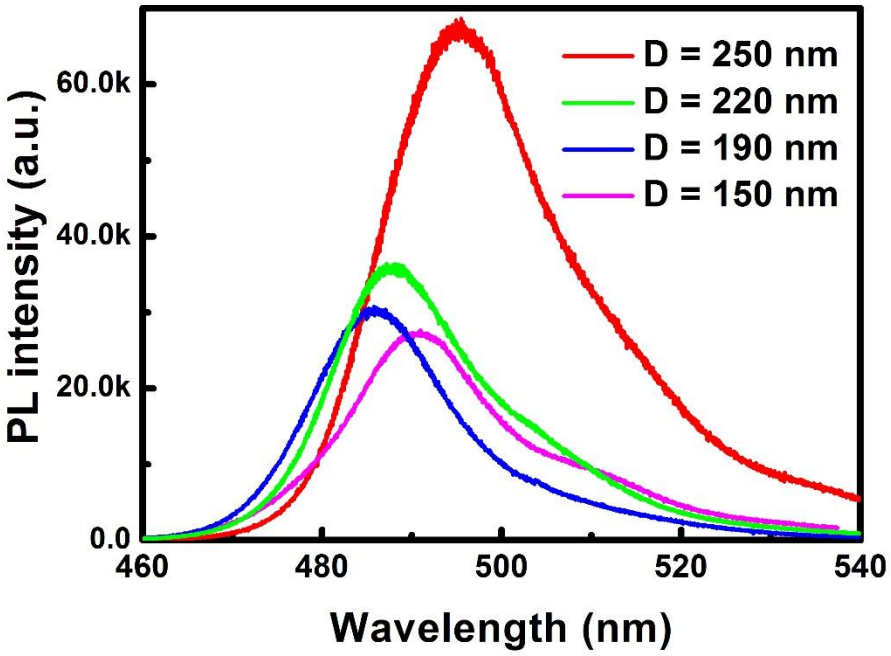

Figure 4.18 PL spectra of all of the 2D-PhC structures, measured at 12K.

Figure 4.18 shows the PL spectra of all the four 2D PhC structures with different nanohole-diameters, measured at 12 K. It is clear that the PL intensity of the 2D PhC structure with the 250 nm nanohole-diameter is enhanced by factor of ~2 compared with any other sample, which is due to the fact that the emission wavelength is within the PBG region, as stated in Fig. 4.14 (b). A slight variation in PL emission wavelength is due to small difference in strain relaxation as a result of fabrication of nanoholes with different diameters [21, 22].

4.6.2 Time-Resolved PL Measurements

In order to confirm the PhC effect TRPL measurements were performed on all 2D PhC samples, at 12 K, using a time-correlated single photon counting (TCSPC) system and a 375 nm pulsed diode laser, with a pulse width of 83 ps, as an excitation source (see Chapter 3 for further details of this system).

Figure 4.19(a) shows the TRPL traces for all 2D PhC structures. A standard bi-exponential component model is used to study the excitonic dynamics, and thus the TRPL traces [I(t)] can all be described by (4.5) [22, 23].

$$I(t) = A_1 e^{\left(-\frac{t}{\tau_1}\right)} + A_2 e^{\left(-\frac{t}{\tau_2}\right)} \qquad (4.5)$$

Where A_1 and τ_1 are the fast component and A_2 and τ_2 are the slow component. As the non-radiative recombination can be safely ignored at such low temperatures since non-radiative recombination centers are almost frozen, the spontaneous emission lifetime τ_{PL} is simply equal to the fast decay time τ_1, which can be obtained from the fittings based on (4.5).

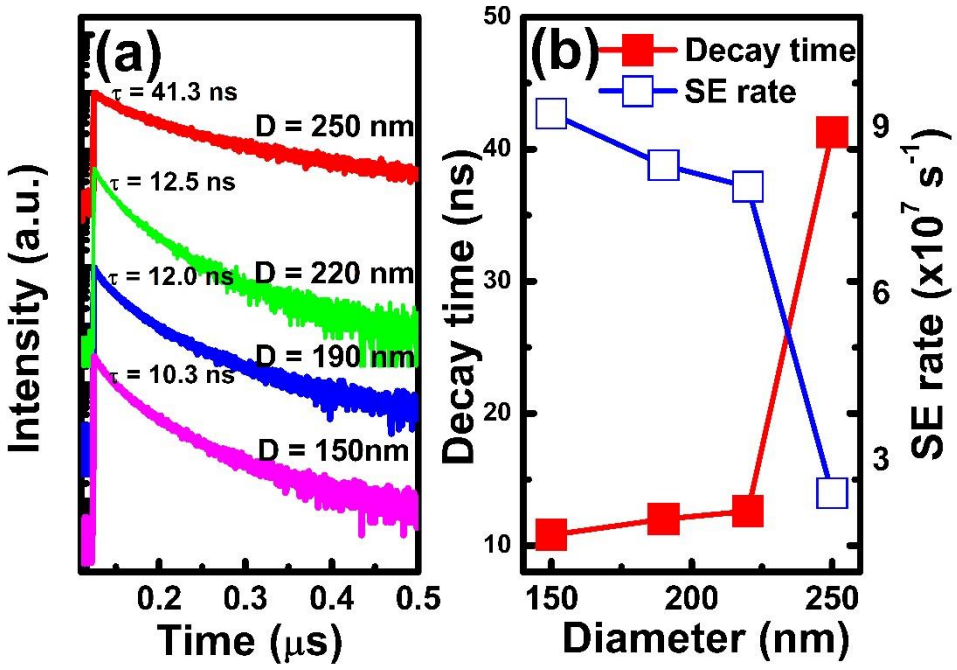

Figure 4.19 (a) TRPL traces of all the four 2D PhC structures, recorded at 12 K; (b) spontaneous emission decay time and rate against nanohole diameter.

The spontaneous emission lifetimes (τ_{PL}) of 10.3, 12, 12.5, and 41.3 ns have been obtained, and are for the 2D PhC structures with a nanohole diameter of 150, 190, 220, and 250 nm, respectively. Figure 4.18(b) shows the spontaneous emission lifetime and also the spontaneous emission rate (i.e., $1/\tau_{PL}$) as a function of the

nanohole-diameter, indicating that the spontaneous emission lifetime of the 2D PhC with the 250 nm nanohole-diameter increases suddenly to 41.3 ns from around 10 - 12 ns. In terms of the spontaneous emission rate, the 2D PhC with the 250 nm nanohole-diameter exhibits a reduction with a factor of 4 compared with the other structures.

This is due to the inhibition of the spontaneous emission along all 2D slab-plane directions (i.e. slab modes) as the emission wavelength is within the PBG region. According to the slab waveguide model suggested by Noda, et al. [14], the optical modes can be divided into slab modes and vertical modes. The former leads to the light propagation within the 2D slab-plane and thus prevents the light being extracted out of a device, and the latter allows light to be emitted out of a device. Therefore, the overall spontaneous emission rate (R_{spon}) can be expressed as a sum of the spontaneous emission rate for slab modes (R_{slab}) and the spontaneous emission rate for vertical modes ($R_{vertical}$) as given below [14],

$$R_{spon} = R_{slab} + R_{vertical} \qquad (4.6)$$

For a standard planar device, $R_{slab} >> R_{vertical}$ due to the waveguide effect discussed above. If a 2D PhC structure is introduced, the conditions for the formation of slab modes disappear. Therefore, the propagation of the light emission light along 2D slab-plane direction is inhibited, and the light is redistricted along vertical direction simultaneously. In that case, R_{slab} is significantly reduced, while $R_{vertical}$ is supposed to remain unchanged. As a result, the spontaneous emission rate is strongly reduced and the lifetime increases. It is worth highlighting that if the emission wavelength is outside the photonic band gap, the light can still propagate along the 2D slab-plane directions and the spontaneous emission rate will remain unchanged.

Therefore, the PhC structure with the 250 nm nano-hole diameter exhibits a considerably reduced spontaneous emission rate, while all the others remain approximately unchanged, as shown in Fig. 4.19 (b).

4.6.3 Angular Dependent Measurements of the 2D-PhC Nanohole Arrays

Angular dependent PL measurements have been performed in order to further investigate the behaviours of the PhC structures. The emission patterns of the PhC structures are shown in Fig. 4.20(a)–(d). Figures 4.19(b), 4.20(c), and 4.20(d), correspond to the PhC structures with a nano-hole diameter of 220, 190, and 150 nm, respectively. These show a relatively uniform PL intensity across the whole angle range as a result of the allowed propagation in slab modes. In contrast, Fig. 4.20(a) which gives the emission pattern of the PhC structure with a 250 nm nanohole diameter shows a concentrated distribution of the PL intensity along a vertical direction (normal to the sample surface) due to the inhibition of slab modes, leading to the energy redistribution into the vertical direction. This confirms the photonic crystal effect. [25].

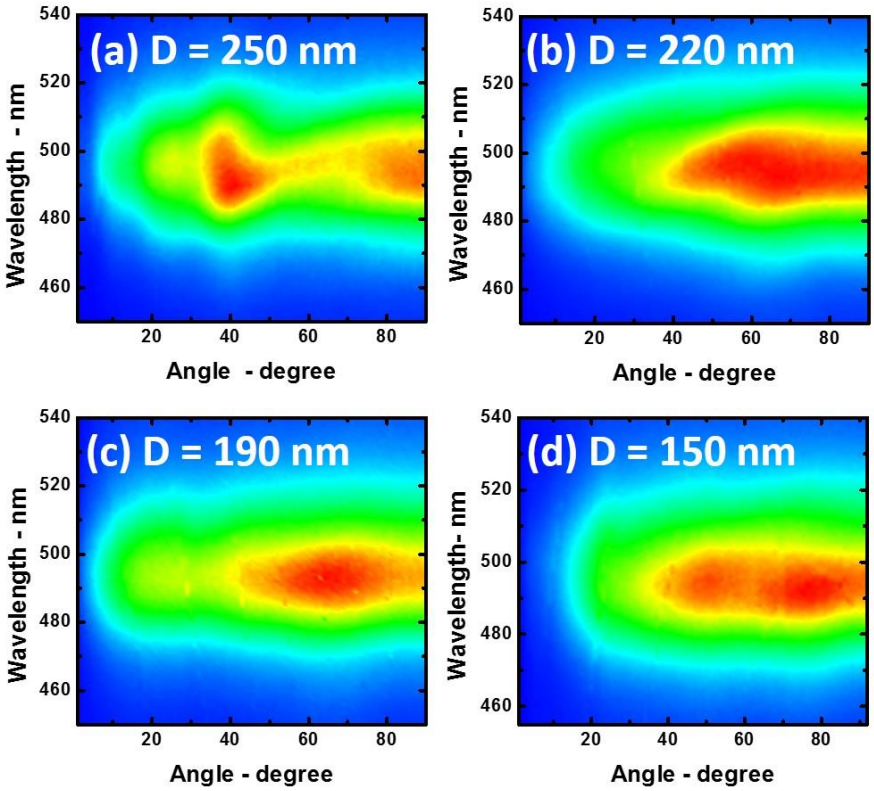

Figure 4.20 Angular emission patterns for the 2D PhC structures with nanohole diameters of (a) 250nm, (b) 220nm, (c) 190nm and (d) 150nm.

4.6.4 Internal Quantum Efficiency of the 2D PhC Nanohole Arrays

In order to further confirm that the enhanced PL intensity of the PhC structure with the 250 nm nano-hole diameter is due to an increase in extraction efficiency instead of IQE, temperature-dependent PL measurements have been performed on all the samples under identical conditions. The integrated PL intensity as a function of temperature has been widely used to estimate IQE.

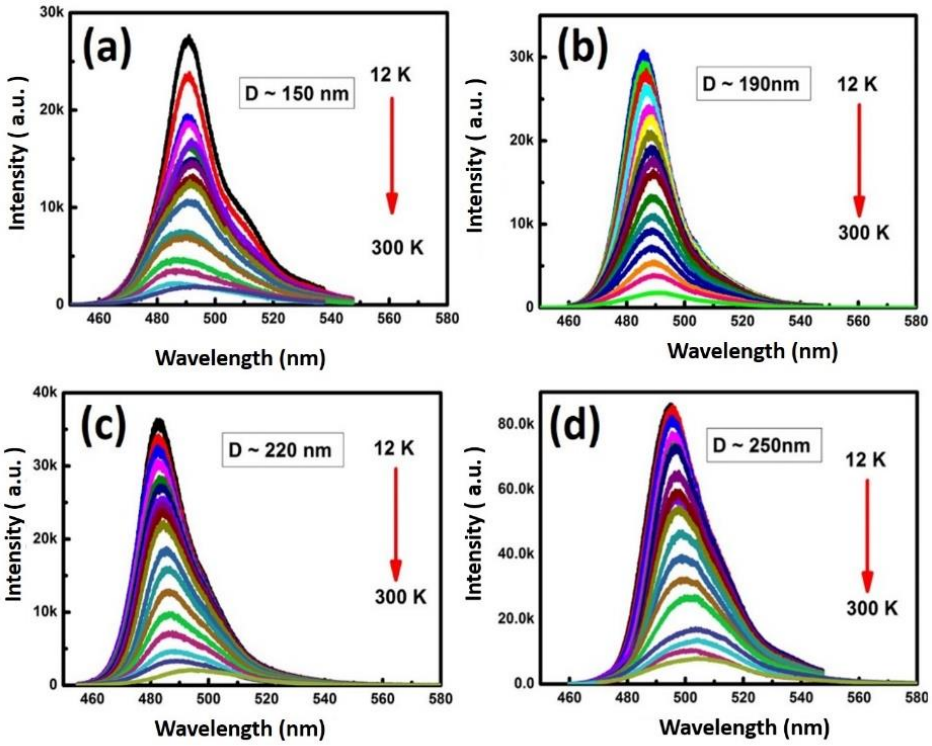

Figure 4.21 Temperature-dependent PL measurements of the 2D-PhC nanohole arrays with diameter of (a) 150 nm, (b) 190 nm, (c) 220 nm and (d) 250 nm.

Figure 4.21 (a)–(d), shows the PL intensities of the samples with 150, 190, 220 and 250 nm diameters as a function of temperature, respectively. In order to estimate the IQE of the samples the assumption is made that all the non-radiative centers at 12 K are frozen. The IQE for the samples was calculated by using (4.7).

$$\eta_{IQE} = \frac{I(T)}{I\,(12\,K\,)} \qquad (4.7)$$

Where I (T) is the integrated PL intensity at specified temperature and I (12K) is the integrated PL intensity at 12 K.

Figure 4.22 clearly demonstrates that all the samples exhibit similar IQE. Therefore, we can attribute the increase in PL intensity to the inhibition of the formation slab modes and their redistribution in the vertical direction, confirming the 2D PhC effect of the nanohole arrays with a 250 nm diameter once again.

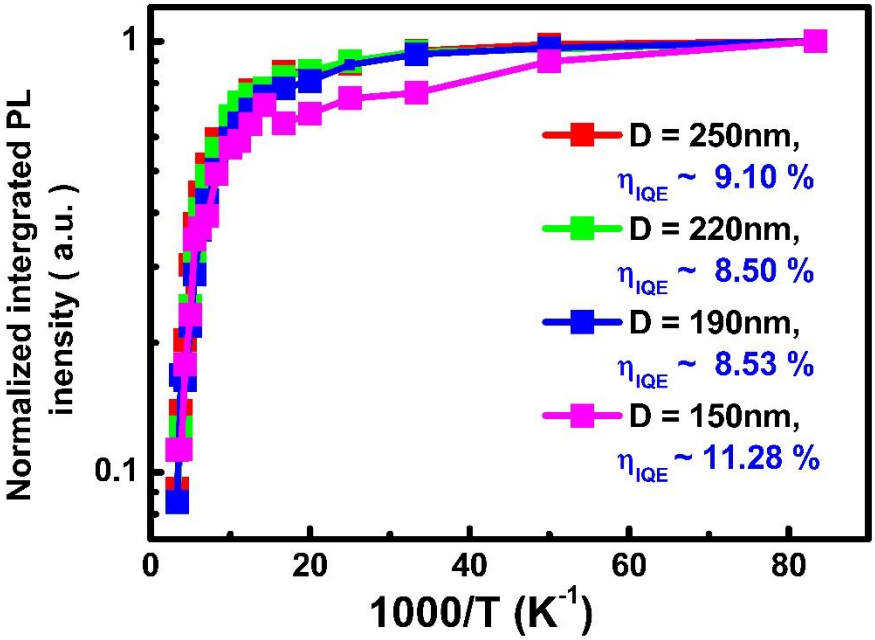

Figure 4.22 Normalized integrated PL Intensity of all of the samples as a function of temperature.

4.7 Summary

In summary, a very cost-effective approach has been developed in the fabrication of 2D PhC structures in InGaN/GaN MQW samples. The PL intensity has been observed to have been enhanced by a factor of 2. This was due to an increased extraction efficiency compared to other 2D PhC structures whose emission wavelength exists outside the PBG. Finally, the inhibition of the slab modes in the 2D slab-plane direction and redistribution of the light in the vertical direction was observed and confirmed by time-resolved PL measurements. This agrees with a well-established model for the inhibition and redistribution of spontaneous emission due to the 2D PhC effect.

References

[1] T. Ogi, L. B. Modesto-Lopez, F. Iskandar, and K. Okuyama, *Colloids Surf.* vol. **A297**, p. 71 (2007).

[2] K. H. Li and H. W. Choi, *J. Appl. Phys.* vol. **109**, p. 023107 (2011).

[3] K. H. Li and H. W. Choi, *Phys. Status Solidi (C)* vol. **8**, p. 2351 (2011).

[4] K. H. Li, Z. Ma, and H. W. Choi, *Appl. Phys. Lett.* vol. **100**, p. 141101 (2012).

[5] M. Athanasiou, T. K. Kim, B. Liu, R. Smith and T. Wang, , *Appl. Phys. Lett.* vol. **102**, p. 191108, (2013).

[6] C. Kao, J. Chu, H. Kuo, S. Wang and C. Yu, *IEEE Photonics Technol. Lett.* vol. **17**, p. 983 (2005).

[7] W. C. Peng and Y. S. Wu, *Appl. Phys. Lett.* vol. **88**, p. 181117 (2006).

[8] S. M. Pan *et al., IEEE Photonics Technol.Lett.* vol. **15**, p. 649 (2003).

[9] E. H. Park, I. T. Ferguson, S. K. Jeon, J. S. Park and T. K. Yoo, *Appl. Phys. Lett.* vol. **89,** p. 251106 (2006).

[10] M. R. Krames *et al., Appl. Phys. Lett.* vol. **75**, p. 2365 (1999).

[11] K. McGroddy *et al., Appl. Phys. Lett.* vol. **93**, p. 103502 (2008).

[12] S. Fan, P. R. Villeneuve, J. D. Joannopoulos and E. F. Schubert, *Phys. Rev. Lett.* vol. **78**, p. 3294 (1997).

[13] E. Yablonovitch, *Phys. Rev. Lett.* vol. **58**, p. 2059 (1987).

[14] M. Fujita, S. Takahashi, Y. Tanaka, T. Asanao and S. Noda, *Science* vol. **308**, p. 1296 (2005).

[15] B. S. Cheng *et al.*, *Semicond. Sci. Technol.* vol. **23**, p. 055002 (2008).

[16] J. Bai, T. Wang, P. Parbrook and A. G. Cullis, *Appl. Phys. Lett.* vol. **89**, p. 131925 (2006).

[17] B. Baur *et al*. , *Appl. Phys. Lett.* vol. **87**, p. 263901 (2005).

[18] J. J. Wierer, A. David and M. M. Megens, *Nat. Phot.* vol. **3**, p. 163 (2009).

[19] A. David, H. Benisty and C. Weisbuch, *J. Displ. Technol.* vol. **3**, p. 133 (2007).

[20] C. J. Lewins *et al., J. Displ. Technol.* vol. **9**, p. 333 (2013).

[21] B. Liu, R. Smith, J. Bai, Y. Gong and T. Wang, *Appl. Phys Lett.* vol. **103**, p. 101108 (2013).

[22] J. Bai, Q. Wang and T. Wang, *J. Appl. Phys.* vol. **111**, p. 113103 (2012).

[23] J. H. Na *et al.* , *Appl. Psys. Lett.* vol. **89**, p. 253120 (2006).

[24] S. F. Chichibu *et al., J. Appl. Phys.* vol. **111**, p. 103518 (2012).

[25] Y. Cheng, S. Wang, Y. Yin, L. Su and J. Huang, *Optic. Lett.* vol. **36**, p. 1611 (2011).

[26] M. D. Tyona, *Adv. Mater. Res.* vol. **2,** p. 195 (2013).

[27] J. Kim et al., *Opt. Express* vol. **22**, p. A857 (2014)

Chapter 5

Coherent Nanocavity Structures for Enhancement in Internal Quantum Efficiency of III-Nitride Multiple Quantum Wells

5.1 Introduction

One of the greatest challenges in the field of III-nitride optoelectronics is referred to as the "green gap" [1] (see Chapter 1). This refers to effect where the internal quantum efficiency (IQE) of an InGaN based emitter significantly reduces as the emission wavelength moves towards the green spectral region. This reduction in IQE is a result of higher indium concentrations. One of the major causes for this is the strong piezoelectric fields induced by the large lattice mismatch between GaN and InGaN.

This would result in a reduction in the overlap of the electron-wave functions, which decreases the radiative recombination. To overcome this problem several different approaches have been employed, such as the growth of InGaN/GaN MQWs in non-polar or semi-polar orientations [2, 3]. Growth in these orientations can either eliminate or reduce the piezoelectric field induced in the heterostructures. Another method employed involves the post fabrication of nanostructures, which has the effect applying strain relaxation across the InGaN/GaN MQWs [4, 5].

The spontaneous emission (SE) rate needs to be increased in order to enhance the IQE of green InGaN/GaN emitters. It has been predicted that an atom in an optical

cavity can radiate much faster than in free space [6]. The SE of an optical field strongly depends on its surrounding electromagnetic vacuum fields, namely the photonic density of states (DoS) or optical modes. As a result, it is possible to achieve an enhanced SE rate by manipulating optical modes [7-10]. The enhancement factor (cavity Purcell factor), F, is defined as the ratio of an emission rate in a system with an optical cavity to one without an optical cavity, as described by (5.1) [11].

$$F_p = \frac{\Gamma_{cav}}{\Gamma_0} = \frac{3Q\lambda^3}{4\pi^2 V_{mod}} \qquad (5.1)$$

Where Γ_{cav} and Γ_0 are the emission rates of a system with and without an optical cavity respectively, Q is the cavity quality factor, and V_{mod} is the cavity mode volume.

When a spontaneous emission wavelength matches the resonance wavelength of the cavity mode, an enhanced spontaneous emission rate can be achieved. Over the last decade a number of pioneering works have been performed on a micro-pillar cavity or a micro-disk in semiconductors [8, 10, 12 - 17], as it can lead to a reduction in cavity mode volume and thus an increase in Purcell factor. It is expected that a further enhancement in Purcell factor can be obtained through further reducing the cavity mode volume, by using a nanocavity or nanodisk instead of a microcavity or microsdisk

Fabrication of InGaN/GaN based emitters on a nanometer scale is presently particularly important for green InGaN/GaN emitters. Recently a significant reduction in the strain induced piezoelectric field has been achieved by fabrication of the device using an InGaN/GaN nanorod structure with a diameter less than 300 nm [28, 29].This has led to an increase in SE rate and thus an enhancement in IQE, which has shown particularly effective for InGaN/GaN based light emitting diodes (LEDs) in the green spectral region. It is expected that the introduction of the nanocavity effect into InGaN/GaN based nanorod LEDs allows to achieve a new kind of LED with a further enhanced IQE.

In the present study, "coherent" nanocavity effect is demonstrated, using two dimensional (2D) InGaN/GaN nanodisk arrays with a diameter below 300 nm in a well-ordered manner. This coherent nanocavity effect can generate an extra cavity mode with a resonance wavelength in the green spectral region compared with a single nanodisk with the resonance wavelength of the cavity mode exclusively in the UV spectral region. The 2D well-ordered InGaN/GaN nanodisk array structures are fabricated by means of a very cost-effective nanosphere lithography technique. Time resolved photoluminescence (TRPL) measurements have shown a clear enhancement in SE rate due to the coherent nanocavity effect. Temperature-dependent photoluminescence (PL) measurements have shown an amazing improvement in IQE with a factor of 88, compared with the as-grown sample. Such an array structure is particularly important for fabrication of a green LED with an ultra-high output power, which cannot be achieved using a single nanodisk.

5.2 Characterisation of the As-Grown Sample

5.2.1 Structural Characterisation

For the fabrication of periodic nanodisk arrays, the InGaN/GaN MQW sample used was grown on a c-plane sapphire substrate with a high temperature AlN buffer layer grown using a low pressure metalorganic chemical vapour deposition (MOCVD) system, as detailed description in Chapter 4 [18, 19].

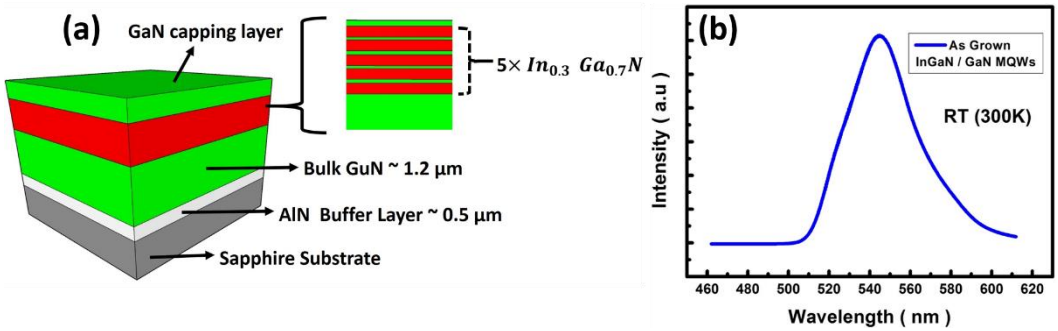

Figure 5.1 (a) Structure of the as-grown sample (b) room temperature PL of the as-grown sample.

Figure 5.1(a) shows the heterostructure of the sample used. Figure 4.1(b) shows the PL of the as-grown sample with a peak emission at 545nm. The surface morphology was also examined using atomic force microscopy (AFM) as shown in Fig. 5.2.

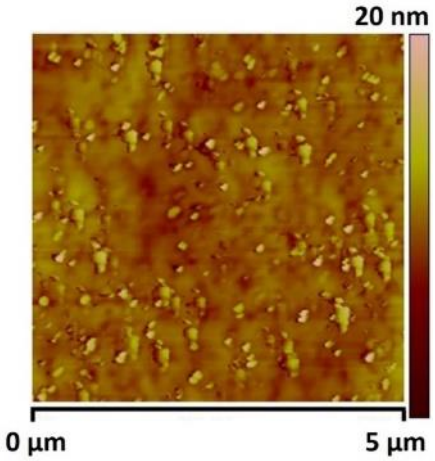

Figure 5.2 AFM images of the as-grown InGaN/GaN MQWs sample.

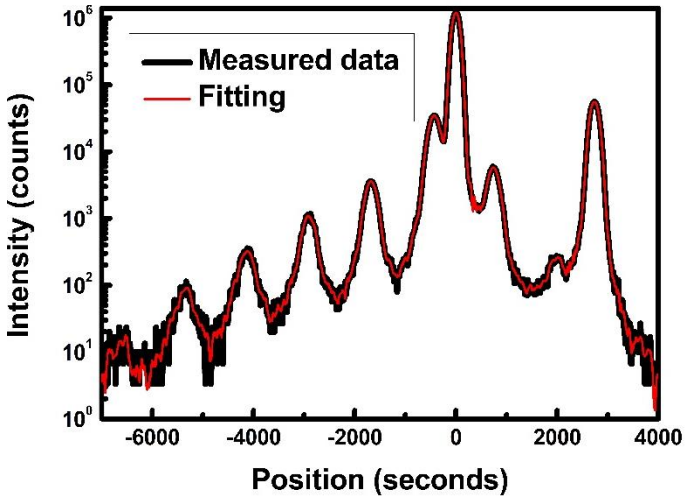

Figure 5.3 XRD spectrum scanned in a ω - 2Θ scan. Black line is the measured data and red line is the fitted data.

Material	InN mole fraction	Thickness (nm)	Period
InGaN Quantum Well	30 %	2	5
GaN Quantum barrier	0	9	5

Table 5.1 Simulation data used to model XRD ω – 2θ scan.

X-ray diffraction measurements show 30% of the indium composition for the quantum wells the thicknesses of the InGaN quantum wells and GaN barriers are 2nm and 9nm, respectively.

5.3 2D-Nanodisk Array Fabrication Optimisation

For the fabrication of nanodisk arrays, nanosphere lithography was used. Fig. 5.4 presents a schematic diagram illustrating a detailed fabrication procedure. The samples were first cleaned sequentially using n-butyl acetate, acetone and IPA in order to degrease and remove any unwanted dust particles. An 80 nm silicon dioxide layer was then deposited using plasma-enhanced chemical vapour deposition (PECVD). The samples with the silicon dioxide layer were subjected to a 3 minute RIE oxygen (O_2) plasma cleaning in order to make the silicon dioxide surface hydrophilic [21], which facilitate silica nanospheres solution to be spread across its surface.

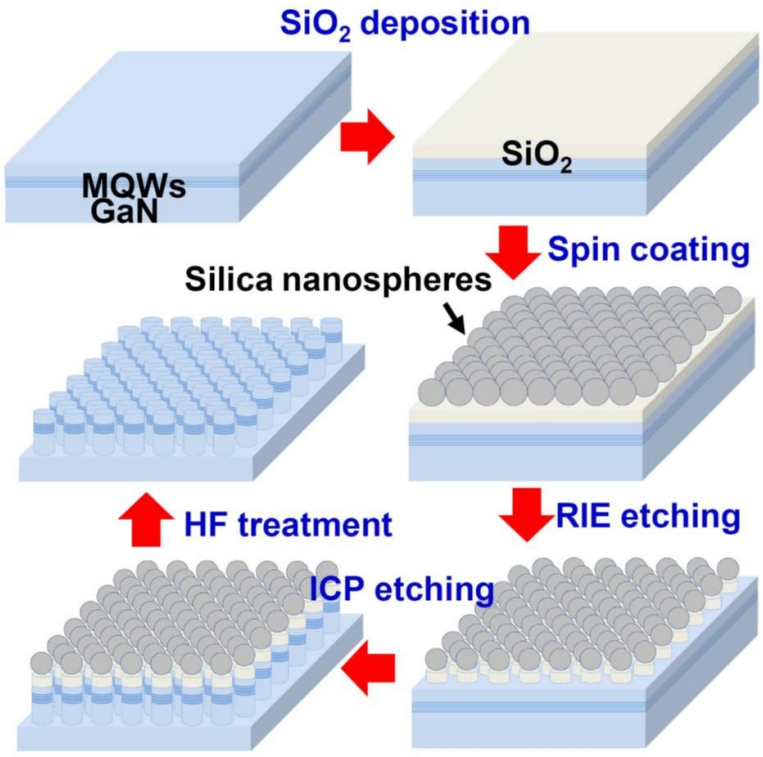

Figure 5.4 Schematic diagram of the procedure used to fabricate nanodisk array structures.

Silica nanosphere particles with a diameter of 274nm diluted in de-ionised (DI) water with a 10% concentration was then mixed in a 1:100 volume concentration with SDS surfactant, preventing aggregation of the nanospheres. This solution was then dropped on the samples surface and spin coated for 45 seconds at 2300 rpm, as detailed description in Chapter 4.A selective RIE etching process was then performed on the nanospheres to set their diameter. The nanospheres will then serve as the mask for etching through the InGaN MQWs. During the etching process the SiO_2 layer exposed around the nanospheres is etched away simultaneously. Finally a Cl_2 based inductively coupled plasma etching was used to etch the InGaN/GaN MQW sample into a well-ordered 2D nanodisk array structure with a height of 350 nm.

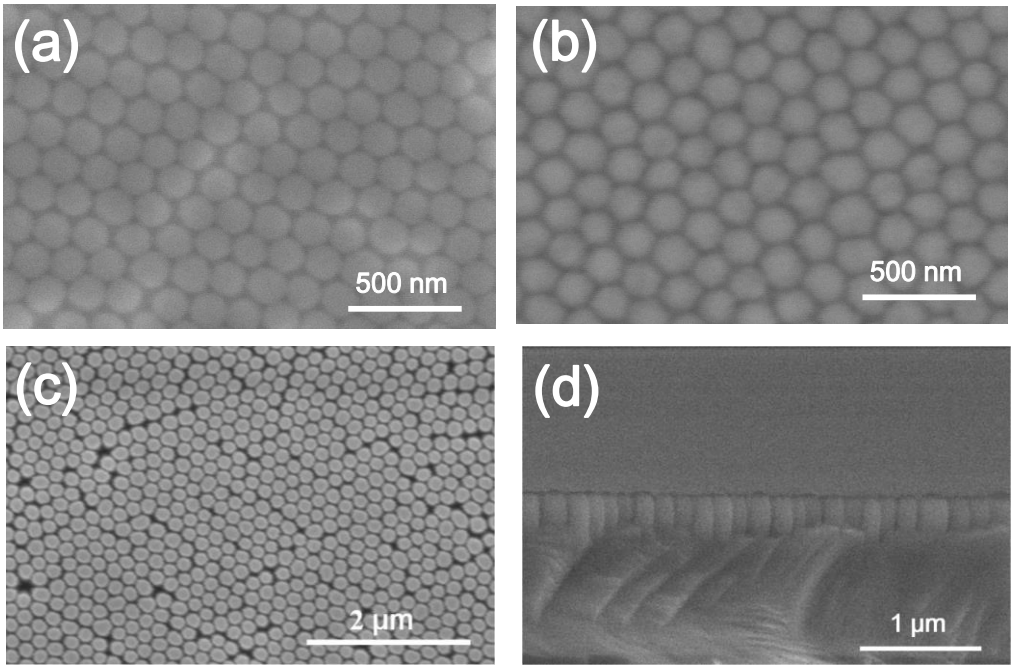

Figure 5.5 (a)-(d) SEM images of each of the steps completed in the fabrication procedure.

Figure 5.5 SEM images show each step during the fabrication procedure, in order to monitor and control the quality of each sample. Figure 5.5(a) shows the nanospheres deposited on the sample by spin coating, forming a close-packed hexagonal array. Figure 5.5(b) shows the nanospheres after tuning of their

diameter via RIE. The 2D hexagonal array of nanodisks were then transferred into the InGaN/GaN MQWs using ICP dry etching technique. A cross-sectional SEM image of the nanodisks arrays with a height of 350 nm is presented in Fig. 5.5 (d) with straight sidewalls.

5.3.1 SiO_2 Layer Purpose

The deposition of silica nanosphere particles was made directly onto a silicon dioxide layer instead of the InGaN/GaN MQWs surface as in Chapter 4. Due to their small size the distribution of the silica nanospheres is sensitive to the surface morphology. This effect could result in disordered arrays and a limited area coverage of close-packed monolayers. Therefore the nanospheres were spin coated onto an atomically flat silicon dioxide surface instead of the rough surface of the InGaN/GaN MQWs, where typical "v" pits appear as discussed in Chapter 4.

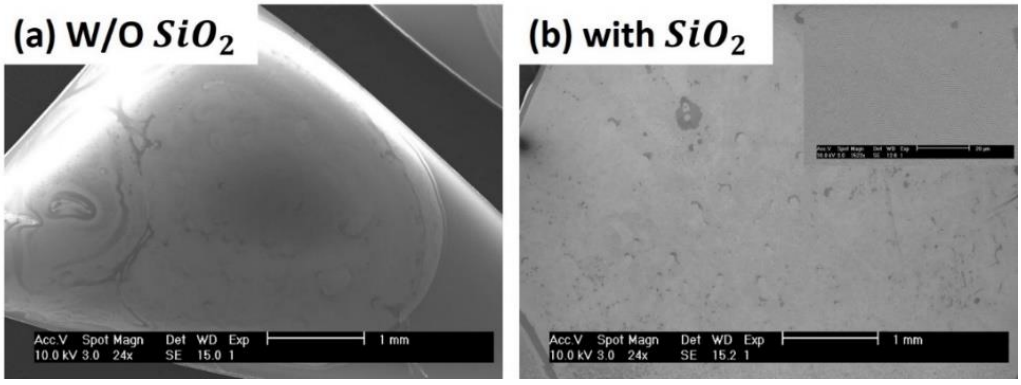

Figure 5.6 Large scale top view SEM images showing silica nanosphere coverage on GaN/InGaN MQWs (a) without SiO2 layer and (b) with SiO2 layer. Low magnification top view SEM images, which present the formation of a close-packed 2D array of nanodisks.

Figure 5.6 (a) and (b) show the top view SEM images of the deposited silica nanospheres on a large scale on a silicon dioxide layer and directly on the surface of an InGaN/GaN sample, respectively. A significant improvement in the monolayer nanospheres coverage is observed on the sample prepared with the SiO_2. Additionally the edge effects were almost eliminated for the sample with the

silicon dioxide layer. Figure 5.5 (b) shows a higher magnification image of a defect-free close-packed array of nanodisks. Additionally, the silicon dioxide layer also provides an extra protection layer during the ICP dry etching for the masked region underlying it.

5.3.2 ICP Dry Etching Optimisation

After the RIE etching to select the nanodisk size (see Chapter 4), the nanodisk mask is transferred into the InGaN/GaN MQWs for further etching using an ICP dry etching technique. In contrast with nanohole arrays fabricated in Chapter 4, the ICP dry etching conditions were optimised to achieve straight sidewalls for the nanodisks.

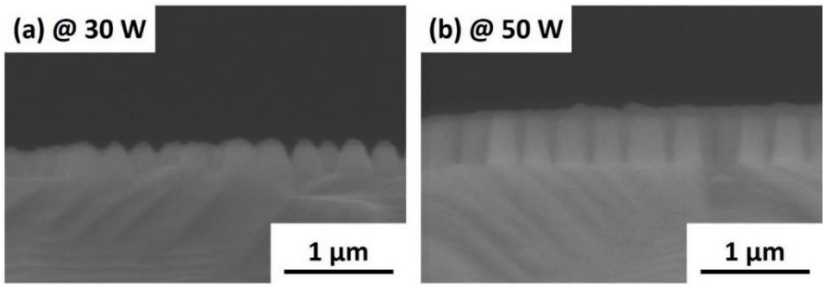

Figure 5.7 Cross sectional images of the nanodisk arrays with (a) 30 W ICP RF power and (b) 50 W ICP RF power.

In the fabrication of nanohole arrays in Chapter 4, using an ICP RF power of 30 W resulted in an inclined sidewall, as seen in the cross section SEM image of Figure 5.7 (a). Increasing the ICP RF power to 50 W resulted in straight sidewalls.

5.4 FDTD Simulation Results

Finite difference time domain (FDTD) were performed using a commercially available software from Lumerical computational solutions. At this point I would like to thank the support team of Lumerical for their help optimizing the simulation conditions for our structures.

Three-dimensional FDTD simulations were performed to examine the nanodisk arrays, as Fig. 5.8 shows. The nanodisk diameter was fixed at 205nm (as discussed

later in Section 5.5), and the resonance wavelength of the cavity modes position were simulated for an InGaN/GaN nanodisk array structure as a function of the centre-to-centre separation.

When separation is greater than or equal to 600 nm the simulation results of the nanodisk array structure are identical to those of a single nanodisk. This demonstrates that only a single cavity mode with its resonance wavelength in the UV spectral region is obtained. As the separation is reduced more cavity modes are observed with their resonance wavelengths are longer than for the single cavity mode case. Reducing the separation to 300 nm or less, yields a cavity mode with a resonance wavelength at 510 nm, which is within the green spectral region. The appearance of more cavity modes is due to a strong interaction among the optical fields of the well-ordered nanodisks, resulting from a small separation, thus generating a "coherent" nanocavity effect.

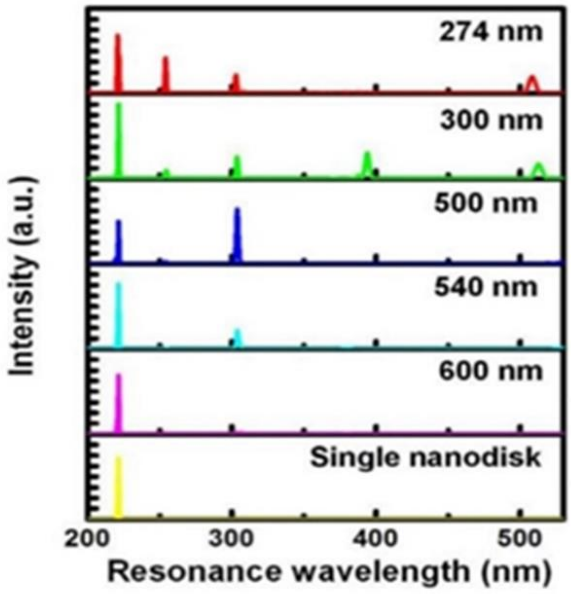

`

Figure 5.8 Simulated results of nanodisk arrays and a single nanodisk, with a fixed 205nm nanodisk diameter. Resonance wavelength spectra of nanodisk array structures as a function of the centre-to-centre separation between nanodisks from 274, 300, 500, 540 and 600 nm; and the resonance wavelength spectra of a single nanodisk provided for comparison.

The FDTD simulation indicates that a single InGaN/GaN MQW nanorod or nanodisk (with a diameter of 300 nm or less) exhibits resonance wavelengths of the cavity modes, which exclusively dominate the ultraviolet (UV) spectral region, as shown in Fig. 5.9(a). In order to seek out any extremely weak modes, Fig. 5.9(a) is plotted on a log scale. This allows observation of a very weak mode at 775 nm (the fundamental mode) and another at 532 nm. It is clear that both modes, which are extremely weak, will not be able to enhance optical performance of green wavelength emitters. Furthermore, all previous studies of the nanocavity effects are limited to a single nanodisk or nanocavity [23-27] and are fabricated using an electron beam lithography (EBL) technique.

Figure 5.9(b) shows the simulated results for the resonance wavelengths of the cavity modes for the nanodisk arrays with the centre-to-centre separation of 274nm between the nanodisks. The nanodisk diameter is fixed at 205nm (explained in Section 5.5). As the nanodisk separation is reduced the cavity modes appears at longer wavelengths becomes gradually stronger. When the separation is reduced to 274 nm a strong cavity mode appearing at 510 nm, evolving from the mode at 532 nm in the case of the single nanodisk, as shown in Fig. 5.9(a). This mode shifting will be discussed shortly.

In addition to the significant enhancement in mode intensity the resonance wavelength has shifted to 510 nm from its original 532 nm in the case of the single nanodisk. The significant enhancement of the cavity mode in the green spectral range is due to a strong interaction among the optical fields of the well-ordered nanodisks, resulting from a close separation, and thus generating a "coherent" nanocavity effect.

Due to a strong interaction among the optical fields of the nanodisks, which results from a close separation (i.e. nanocavity coherent effect), emission from the InGaN/GaN MQW in one nanodisk can pass through other coupled nanodisks, as well as the initial nanodisk itself. It is therefore simply the equivalent to an increase in the diameter of the nanodisks. Due to an evanescent nature the interactions or coupling between adjacent nanodisks can only take place as these

nanodisks approach each other. Consequently, as the separation is reduced the interactions become stronger, thus the “effective diameter” increases. This means that strong cavity modes with resonance at longer wavelengths can be generated. For instance, the nanodisk arrays, with a 205 nm nanodisk diameter, with centre-to-centre separation of 274 nm show a significantly enhanced mode at 510 nm, as depicted in Fig. 5.9(b).

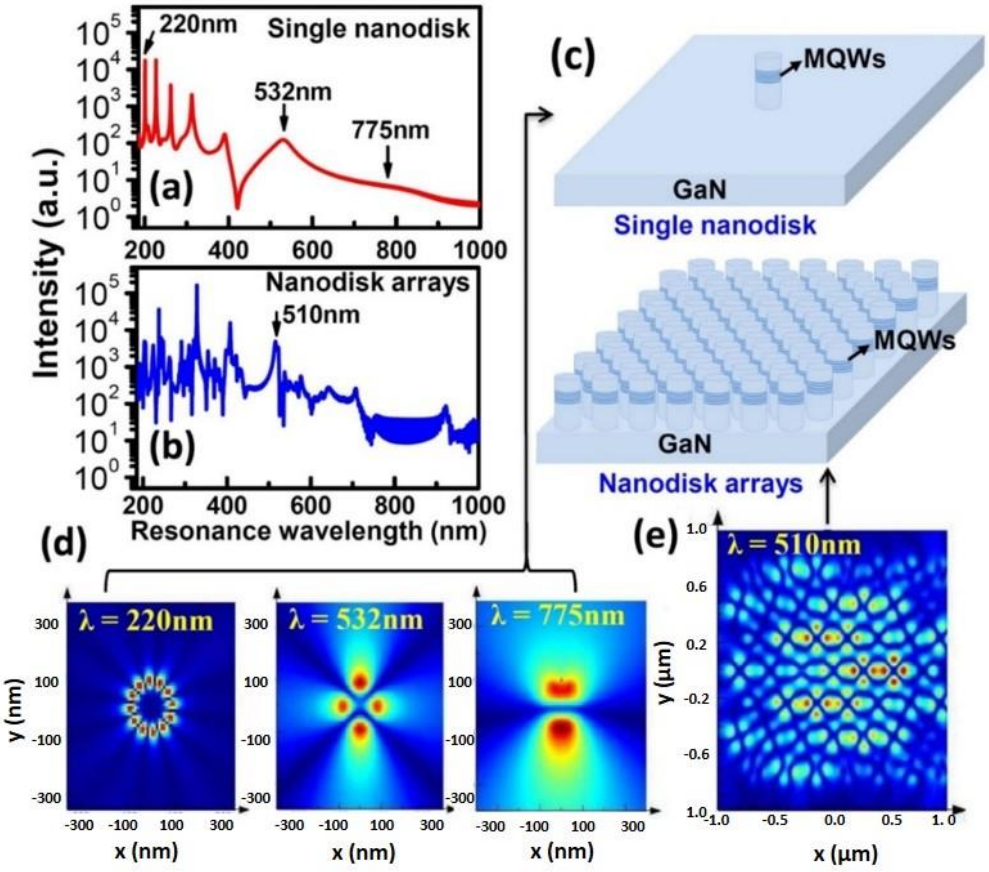

Figure 5.9 Resonance wavelength spectra of a single nanodisk with a 205 nm diameter; (b) resonance wavelength spectra of nanodisk arrays with a centre-to-centre separation of 274 nm and 205 nm diameter; (c) schematic diagram of a single nanodisk with a series of five InGaN/GaN QWs used in the FDTD nanodisk array simulations; (d) electric field distribution profile of the three modes at 220, 532 and 775 nm for a single 205 nm diameter nanodisk; and (e) electric field distribution profile of the nanodisk arrays, monitored at a 510 nm resonance wavelength.

In order to make a comparison between the single nanodisk and the nanodisk arrays the mode profiles in both cases was calculated. Figure 5.9(d) depicts the electric field distribution profile of the three representative modes at 220, 532 and 775 nm in the case of a single 205 nm diameter nanodisk. The mode at 220 nm shows an electrical field distribution with a twelve-fold rotational symmetry; whereas the mode at 532 nm shows only a four-fold symmetry. The mode at 775 nm shows a dipole distribution, which is a finger-print of the fundamental mode.

Figure 5.9(e) depicts the electric field distribution at 510 nm (using a 7 by 7 nanodisk array), which shows a stronger coupling amongst adjacent nanodisks. Further examining the electric field distribution in an individual nanodisk, in Fig. 5.9(c), shows the electrical field distribution has a tetragonal (four-fold) symmetry, similar to the mode at 532 nm in Fig. 5.10(d) for a single nanodisk. This is confirmation that the mode at 510 nm evolves from the mode at 532 nm in the case of the single nanodisk.

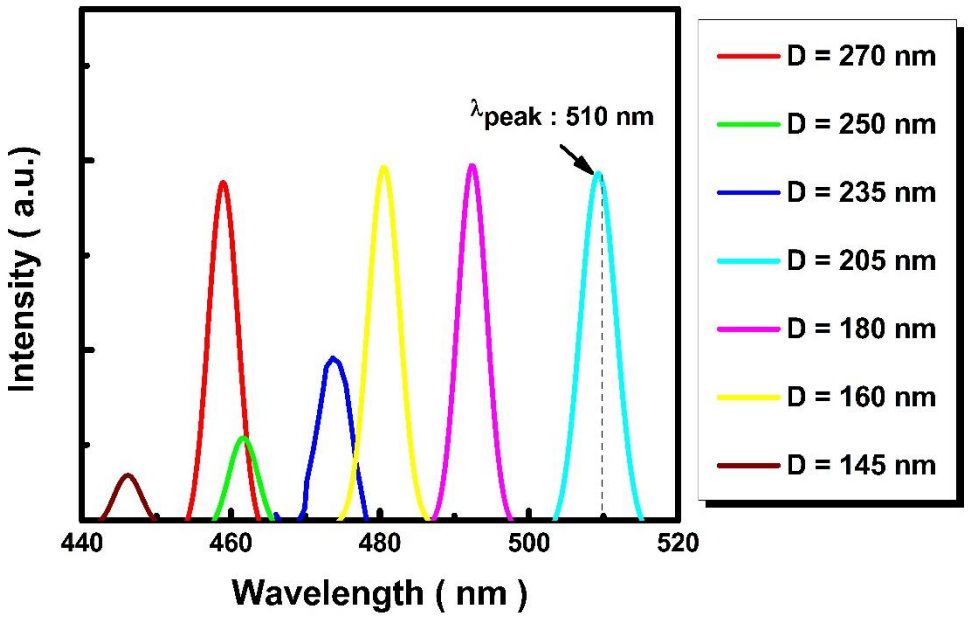

Figure 5.10 Resonance wavelength spectra of the nanodisk array structures with a nanodisk diameter of 145, 160, 180, 205, and 270 nm, where the centre-to-centre separation is fixed to 274 nm.

Figure 5.10 shows the simulated resonance wavelength of the cavity modes as a function of the nanodisk diameter (270, 250, 235, 205, 180, 160 and 145 nm), with a fixed centre-to-centre nanodisk separation of 274nm. The simulated results show that the nanodisk array structure with a 205nm nanodisk diameter exhibits a cavity mode at a 510nm resonance wavelength, the wavelength of interest in this study.

5.5 Optical Investigation of the 2D Nanodisk Arrays

Figure 5.11(a)–(e) shows SEM images of the fabricated nanodisk arrays at a 30^{o} tilt angle. The well-ordered 2D nanodisk array structures, with a series of 5 InGaN/GaN QWs, have an emission wavelength in the green spectral region. The samples were fabricated using the nanodisk fabrication technique presented in Fig. 5.4 above. In each case the typical height of the nanodisks is approximately 350 nm, with nanodisk separation of 274 nm. The diameter of the nanodisks is then varied from 270, 250, 235, 205, 180, 160, and 145 nm.

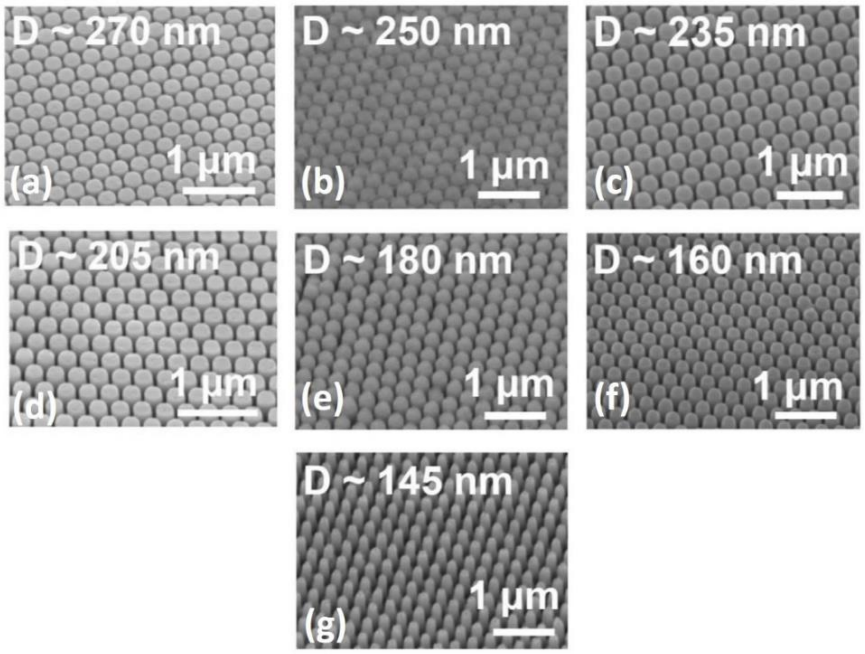

Figure 5.11 SEM images of the nanodisk array structures with a nanodisk diameter of approximately (a) 270 nm, (b) 250 nm, (c) 235 nm, (d) 205 nm, (e) 180 nm, (f) 160 nm and (g) 145 nm.

5.5.1 Photoluminescence Measurements of the 2D Nanodisk Arrays

In order to examine the optical performance of the 2D nanodisk arrays the samples PL was measured with a 375 nm CW laser excitation source at room temperature.

Figure 5.12 (a) clearly indicates a sharp jump in PL intensity for the 2D nanodisks with a diameter of 205 nm, meaning that the PL intensity drops significantly when the nanodisk diameter deviates from 205 nm. Our 3D FDTD simulation as shown in Fig. 5.10 indicates that the resonance wavelength of the cavity mode for the 2D nanodisks with a diameter of 205 nm is at 510 nm, matching the emission wavelength. This demonstrates a significant enhancement in optical efficiency due to the coherent nanocavity effect. The inset in Fig. 5.12 (a) also gives the PL spectra of the as-grown InGaN/GaN sample, showing an emission peak at 545 nm. For the blue-shift in the emission peak of the nanodisk, is attributed to the strain relaxation, resulting from the nanostructures fabrication [4, 28, 29].

IQE labelled as η, can be typically obtained by means of temperature dependent PL measurements using the ratio of an integrated intensity at room temperature to that at a low temperature, such as 12 K in the present study. Figure 5.12(b) shows the integrated PL intensities of all the 2D nanodisk structures as a function of temperature. For reference, the data from the as-grown sample are also provided. Using the as-grown sample as a reference, we can plot the IQE enhancement factor (defined as the ratio of the IQE of each nanodisk sample to that of the as-grown sample) as a function of nanodisk diameter, which is given in the inset of Fig. 5.12(b), where a sharp jump with an IQE enhancement factor of 88 has been achieved for the 2D nanodisk array structure with a nanodisk diameter of 205 nm. This also confirms the existence of the coherent nanocavity effect. Regarding the IQE enhancements observed on the rest samples, where the resonance wavelengths of the cavity modes do not match the emission wavelength, this is simply due to the strain relaxation as a result of being

fabricated into nanodisk structures, which has been confirmed by our previous studies [28, 29].

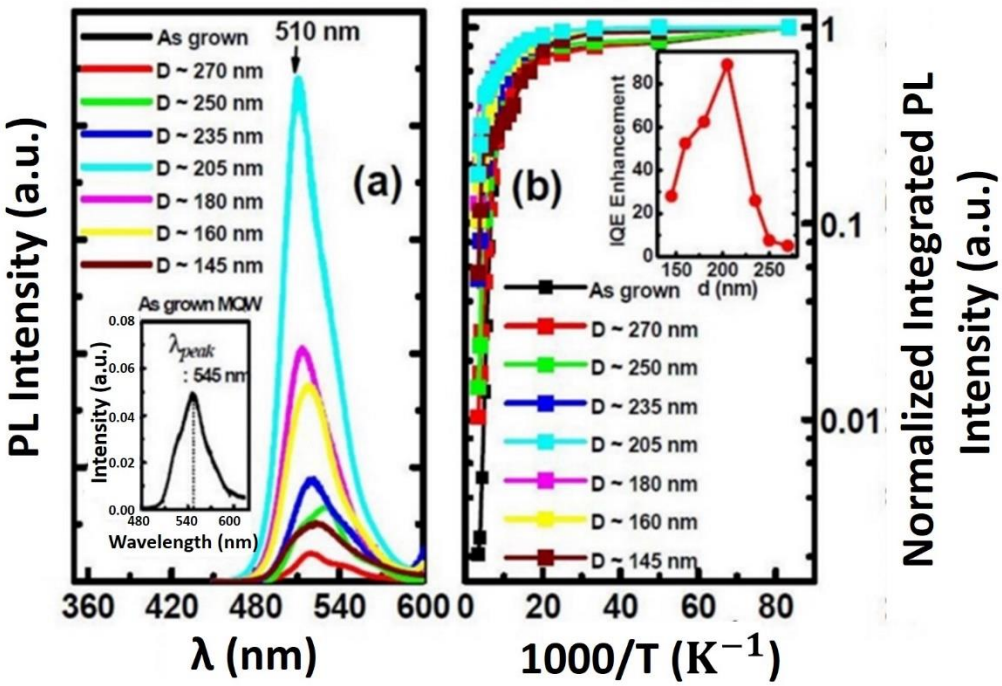

Figure 5.12 (a) PL spectra of the 2D nanodisk array structures at room temperature, inset is the PL spectrum of the as-grown InGaN/GaN MQW sample at room temperature; and (b) Arrhenius plots of the normalized integrated PL intensity as a function of temperature, inset is the IQE enhancement factor as a function of the nanodisk diameter. IQE enhancement is the ratio of the IQE of each nanodisk array structure to the as-grown sample.

The inset of Fig. 5.12(b) plots the IQE enhancement factor as a function of nanodisk diameter; where an increase in the IQE enhancement factor to 88 has been achieved for the 2D nanodisk array structure with a 205nm nanodisk diameter. This also confirms the existence of the coherent nanocavity effect. In regards to the IQE enhancement observed for the rest of the samples, where the resonance wavelengths of the cavity modes do not match the emission wavelength. This is due to the strain relaxation that results from the fabrication of the nanodisk structures, as has been confirmed by previous studies [28, 29].

5.5.2 Time-Resolved PL Measurements (TRPL).

To further investigate the recombination dynamics of the coherent nanocavity structures, time-resolved measurements were performed on the samples at low temperature (12 K), where non-radiative components can be safely ignored. TRPL measurements have been performed in a temperature range from 12 to 300 K, using a time-correlated single photon counting (TCSPC) system and a 375 nm pulsed diode laser, with a pulse width of 83 ps, as an excitation source. The average excitation power with a pulse repetition at 10 MHz is 0.1mW, and the system response-time is about 150 ps (see Chapter 3).

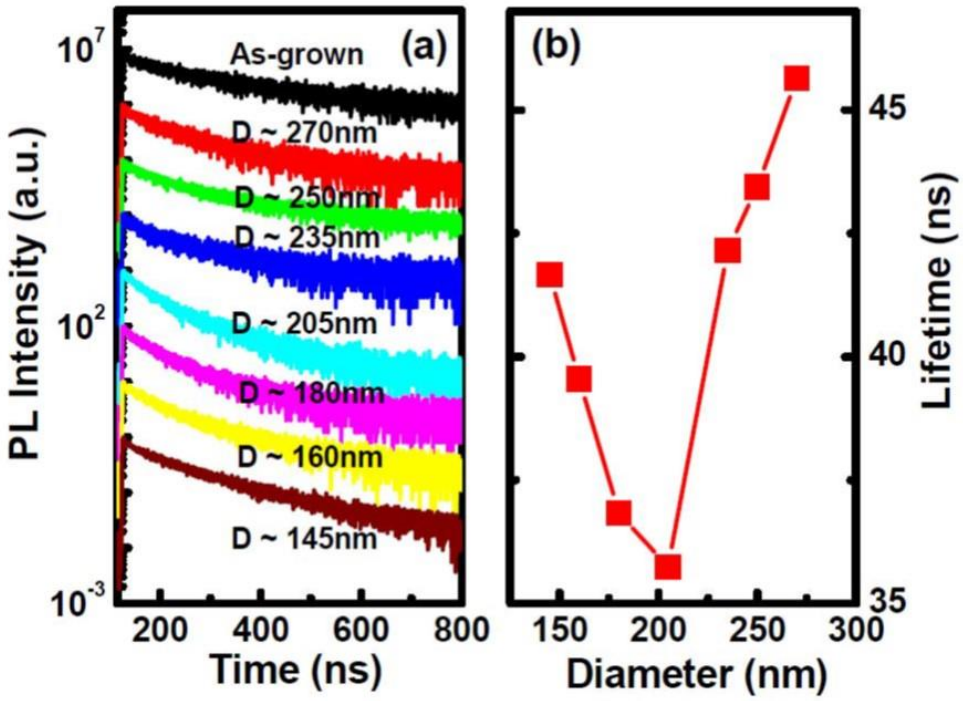

Figure 5.13 (a) TRPL traces of the nanodisk array structures, measured at 12K; and (b) lifetime of the InGaN MQW in the nanodisk array structures as a function of nanodisk diameter.

Figure 5.13 (a) shows the TRPL traces of all of the samples, recorded at a temperature of 12K. The SE lifetime can then be obtained through fitting the TRPL traces with a standard two exponential component model; TRPL traces [I(t)] can be described by (5.2) [30-32].

$$I(t) = A_1 e^{-\frac{t}{\tau_1}} + A_2 e^{-\frac{t}{\tau_2}} \quad (5.2)$$

Where A_1 and τ_1 (A_2 and τ_2) are for the fast (slow) decay component. As stated above the nonradiative recombination can be safely ignored, and thus the PL emission lifetime τ_{PL} is simply equal to the fast decay time τ_1, which can be obtained from the fittings based on (5.2). PL emission lifetime of the InGaN/GaN MQW is plotted as a function of the nanodisk diameter in Fig. 5.13 (b). This plot indicates that the nanodisk array structure with a 205 nm nanodisk diameter has the shortest PL emission lifetime, and therefore the highest SE rate. This improved SE rate when compared to the other samples confirms the existence of the coherent nanocavity effect in a 2D nanodisk array structure for nanodisk diameters of 205 nm.

5.6 Conclusion

To summarize, a well-ordered 2D InGaN/GaN nanodisk array structure has been designed, which generates a coherent nanocavity effect with a strong cavity mode in the green spectra region. The results were confirmed using 3D FDTD simulation, temperature dependent PL measurements and TRPL measurements of the 2D nanodisk arrays. Additionally the optimised fabrication of 2D nanodisk arrays using silica nanosphere lithography on InGaN/GaN MQW samples, emitting in the green spectrum region, was described. Finally, the coherent nanocavity effect has been shown to generate an anticipated enhanced SE rate. Therefore as a result this has provided a much improved IQE, by a factor of 88 when compared to the as-grown samples.

References

[1] H. Zhao *et al.*, *Opt. Express.* vol. **19**, p. A991 (2011).

[2] S. H. Park, A. Doyeol and S. L.Chuang, *IEEE J. Quantum Electron.* vol. **43**, p. 1175 (2007).

[3] R. M. Farrell *et al., Jpn. J. Appl. Phys.* vol. **46**, p. L761 (2007).

[4] J. Bai, Q. Wang and T. Wang, *J. Appl. Phys.* vol. **111**, p. 113103 (2012).

[5] B. Liu, R. Smith, J. Bai, Y. Gong and T. Wang, *Appl. Phys. Lett.* vol. **103**, p. 101108 (2013).

[6] M. Boroditsky *et al., J. Lightw. Technol.* vol. **17**, p. 2096 (1999).

[7] H. Iwase, D. Englund and J. Vučković, *Optic. Expr.* vol. **18**, p. 16547 (2010).

[8] K. Vahala, *Nature* vol. **424**, p. 839 (2003).

[9] S. Noda, M. Fujita and T. Asano, *Nature Phot.* vol. **1**, p. 4490 (2007).

[10] J. M. Gérard *et al., Phys. Rev. Lett.,* vol. **81**, p. 1110 (1998).

[11] R. G. Baets, D. Delbeke, R. Bockstaele and P. Bienstman, *Proc. of SPIE,* vol. **4996**, p. 74 (2003).

[12] T. Someya *et al., Science* vol. **17**, p. 1905 (1999).

[13] T. Tezuka, H. Yoshida and T. Noda, *Jpn. J. Appl. Phys.* vol. **32**, p. L54 (1993).

[14] A. Tamboli, E. D. Haberer, R. Sharma, K. H. Lee, S. Nakamura and E. Hu, *Nature Phot.* vol. **1**, p. 61 (2006).

[15] G. S. Solomon, M. Pelton and Y. Yamamoto, *Phys. Rev. Lett.* vol. **86**, p. 3903 (2001).

[16] E. Feltin, G. Christmann, R. Butté, J. F. Carlin, M. Mosca and N. Grandjean, *Appl. Phys. Lett.* vol. **89**, p. 071107 (2006).

[17] E. D. Haberer *et al., Appl. Phys. Lett.* vol. **85**, p. 5179 (2004).

[18] T. Wang, J. Bai, P. J. Parbrook, A. G. Cullis *Appl. Phys. Lett.* vol. **87**, p. 151906 (2005).

[19] S. C. Davies, D. J. Mowbray, Q. Wang, F. Ranalli and T. Wang, *Appl. Phys. Lett.* vol. **95**, p. 101909 (2009).

[20] J. Bai, T. Wang, P. J. Parbrook and A. G. Cullis, *Appl. Phys. Lett.* vol. **89**, p. 131925 (2006).

[21] T. Suni, K. Henttinen, I. Suni and J. Ma¨kinen, *J. Electrochem. Soc.* vol. **49**, p. G348 (2002).

[22] M. K. M. Kuttge, F. J. G. d. Abajo and F. Polman, *Nano. Lett.* vol. **10**, p. 1537 (2010).

[23] M. Hill *et al., Nat. Phot.* vol. **1**, p. 589 (2007).

[24] D. J. Gargas *et al.*, *ACS Nano.* vol. **4**, p. 3270 (2010).

[25] M. Khajavikhan *et al.*, *Nature* vol. **482**, p. 204 (2012).

[26] B. S. Song, S. Noda, T. Asano and Y. Akahane, *Nat. Materials.* vol. **4**, p. 207 (2005).

[27] Y. A. Liao *et al., Appl. Phys. Lett.* vol. **94**, p. 053101 (2009).

[28] J. Bai, Q. Wang and T. Wang, *Phys. Status Solidi (A)* vol. **209**, p. 477 (2012).

[29] Q. Wang, J. Bai, Y. P. Gong and T. Wang, *J. Phys. D: Appl. Phys.* vol. **44**, p. 395102 (2011).

[30] S. F.Chichibu *et al.*, *J. Appl. Phys.* vol. **111**, p. 103518 (2012).

[31] B. Liu, R. Smith, J. Bai, Y. Gong and T. Wang, *Appl. Phys. Lett.* vol. **103**, p. 101108 (2013).

[32] R. Smith *et al., Nano. Lett*. vol. **13**, p. 3042 (2013).

Chapter 6

Room Temperature Continuous-Wave Green Lasing from an InGaN Microdisk on Silicon

6.1 Introduction

The last four decade has seen the unparalleled impact of the semiconductor industry, driven by silicon technologies. Silicon based technology is extremely mature and cost-effective. However, it is well-known that silicon has an indirect band structure, which prohibits its use as an effective light emitter. The unification of III-V and silicon technologies would be the ideal way to integrate semiconductor based electronics and photonics. Therefore the fabrication of silicon compatible III-nitride optoelectronics, namely, III-nitride optoelectronics on silicon substrates would be a step in bridging this requirement.

This would be particularly significant to III-nitride based optoelectronics, because the required device fabrication techniques of III-nitrides are more complicated in comparison to other III-V semiconductors. This would not only eliminate their individual fundamental limits, but also draw together the major advantages of the two types of semiconductors. However, there exist a number of great challenges in the epitaxial growth of III-nitrides on a silicon substrate. These challenges are caused by the large lattice-mismatch and large difference in thermal expansion coefficients of silicon and GaN. Consequently, this leads to a less competitive performance than devices grown on the more usual sapphire substrate. To date,

there are no reports of lasing from III-nitrides on silicon in the green spectral region.

Micro or nano-cavities, such as photonic crystal cavities [1, 2] and plasmonic waveguides [3-7], have been demonstrated in the fabrication of laser structures with excellent performance characteristics. In the last decade microdisk lasers have become increasingly popular due to their simple geometry and compact size [8-10]. Microdisk lasers can be used to provide high quality whispering gallery modes (WGMs), leading to a low lasing threshold. This property is particularly significant in III-nitride based lasers, as III-nitride laser diodes (LDs) exhibit intrinsically a much higher lasing threshold compared to other III-V semiconductor LDs. This is due in large part to an intrinsic limitation caused by the high carrier density of states, which results from the high effective mass associated with wide band gap materials [45]. Furthermore, a microdisk laser on a Si substrate can potentially be used to integrate electronics and photonics on the same wafer. This would meet the challenge of fabricating photonic-electronic integrated circuits for communication and computation technologies, overcoming their fundamental speed and bandwidth limits [11]. In this case, taking the extremely mature silicon technology into account, III-nitrides on silicon exhibit overwhelming advantages when compared to the current and widely used GaN on sapphire technology, in the fabrication of microdisk lasers. For instance the utilisation of silicon substrates leads to the formation of an undercut structure easily, which is necessary for microdisks, in order to enhance the light confinement in the disk region. The utilisation of silicon substrates makes the growth of extra sacrificial layers unnecessary, while sacrificial layers are otherwise necessary in fabricating GaN based microdisks on a sapphire substrate [9, 10], as it is extremely difficult to chemically etch sapphire. Additionally the growth of extra sacrificial layers can lead to degradation in the crystal quality, as is this the case with GaN on sapphire. Current GaN based microdisks suffer from serious fabrication problem, which includes inclined sidewalls and non-uniformity in circularity [13], both of which lead to major limits in optical performance. The situation for fabricating GaN

microdisks on sapphire becomes even worse, because extra sacrificial layers, are required to form an undercut structure or the even more complicated distributed Bragg reflector [9, 10, 14]. Both aim to enhance the optical confinement along the vertical direction to minimise the light leakage.

Optically pumped green lasing with an ultra-low threshold has been achieved using an InGaN/GaN based microdisk with an undercut structure on a silicon substrate. Microdisks of an approximate 1 μm diameter were fabricated using a combination of a cost-effective silica microsphere technique, dry-etching and subsequent chemical etching. The combination of these techniques minimises the sidewalls roughness of the microdisks and also produces an excellent circular geometry. Utilizing this fabrication process, lasing has been achieved at room temperature under optical pumping from a continuous-wave laser diode. The threshold for lasing was as low as 1 kW/cm^2. Time–resolved micro photoluminescence (PL) and confocal PL measurements have also been performed to further confirm the lasing action in WGMs, and to also investigate the excitonic recombination dynamics of the lasing.

6.2 III-Nitrides Microdisk Laser History

III-nitride microdisk lasers were first reported in 1997 [15], where an air gap was introduced under the microdisk in order to enhance vertical confinement through wet chemical etching of the aluminium nitride buffer layer. The main disadvantage of this method is due to the etching rate of the AlN buffer layer, mainly depending on the quality of the material. Faster etching rates are possible at the expense of decreasing the crystal quality of the AlN buffer layer. However, an AlN buffer with a high crystal quality is required in order to grow high quality heterostructures.

In 2004, Hu's group at Harvard reported the first microdisk laser fabricated by photo-electrochemical etching techniques [16, 17]. In this method a sacrificial layer was introduced prior to the microdisk region. The sacrificial layer consists of an InGaN/InGaN superlattice structure with a lower indium composition than in

the active region. The sacrificial layer was etched using hydrogen chloride (HCL) solution under an optical illumination with a proper wavelength for selective etching, meaning that the lower indium composition region is etched away. Growth of the sacrificial InGaN/InGaN SL is undesirable because it significantly lowers the quality of the overlying microdisk region.

Choi (2006) reported III-nitride based micro-disk on silicon [18], where an InGaN/GaN MQW structure was grown on top of a Si wafer. The disks were defined using optical lithography methods and then etched through the Si substrate. Silicon, a well-known and established technology for over 40 years, can be selectively wet chemical etched with hydrogen fluoride (HF) and nitric acid (HNO_3). An air gap can therefore be introduced under the disk region in order to achieve an enhanced optical confinement in the vertical direction.

The concept of a microdisk laser differs significantly from conventional Fabry-Perot lasers, as the modes formed in a microdisk laser are due to whispering gallery resonances which circulate the periphery of the disk.

6.3 Characterisation of the As-Grown Sample

6.3.1 Structural Characterisation

For the fabrication of microdisk lasers, a standard five period InGaN/GaN multiple quantum well grown (MQW) was grown on (111) silicon substrate by MOCVD. The high temperature AlN buffer layer, originally developed for the growth of GaN on sapphire, was modified before using it in the growth of GaN on Si [19-21]. The epiwafer consists of a 200 nm AlN buffer layer followed by a 500 nm GaN buffer layer, both of which are grown at high temperatures. Five periods of $In_{0.27}Ga_{0.83}N$/GaN MQWs were then grown with the thicknesses of the barrier and quantum well of 2.5 nm and 10 nm, respectively. This is then followed by a 10 nm GaN capping layer.

Figure 6.1(a) illustrates the structure of the as-grown used in the fabrication of the microdisk lasers; where Fig. 6.1(b) shows the room temperature PL emission of the as-grown sample with an emission peak at 543 nm.

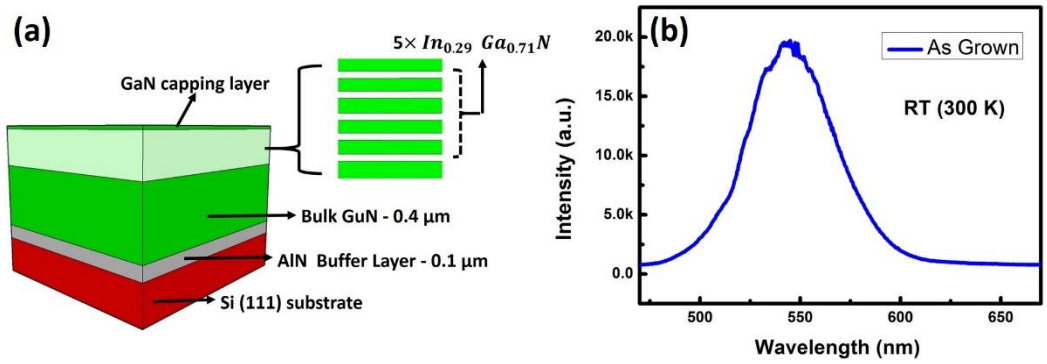

Figure 6.1 (a) Schematic diagram of the InGaN/GaN MQW epiwafer grown on a (111) silicon substrate via MOCVD; and (b) room temperature PL measurements of the as-grown epiwafer.

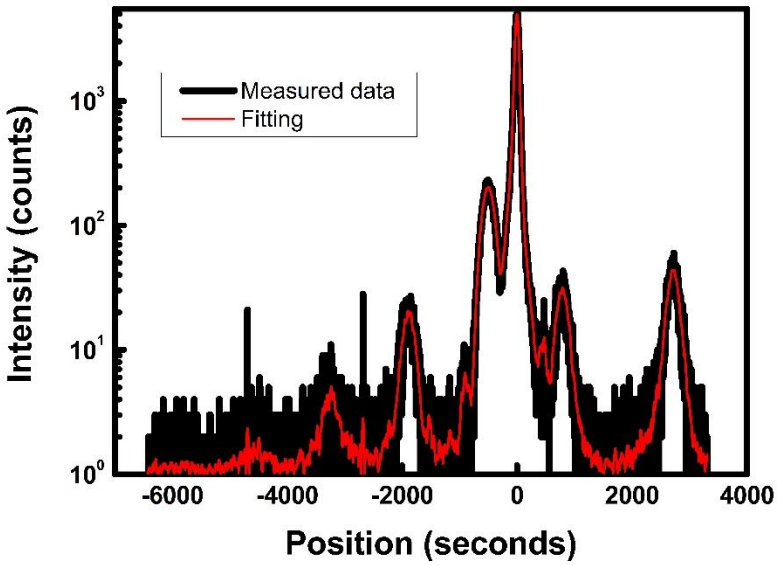

Figure 6.2 XRD spectrum scanned in a ω - 2Θ scan. Black line is the measured data and red line is the fitted data.

Material	InN mole fraction	Thickness (nm)	Period
InGaN Quantum Well	27 %	2	5
GaN Quantum barrier	0	10	5

Table 6.1 Simulation data used to model XRD ω – 2θ scan.

Figure 6.2 XRD spectrum scanned in a ω - 2Θ mode; where the black line is the measured data and the red line is the fitted data. The table shows indium composition and thicknesses of the InGaN quantum well and GaN barriers, respectively.

6.4 Fabrication of the Microdisk Laser

In the fabrication of the microdisk lasers a silica nanosphere lithography technique was used [22-23]. Figure 6.3 (a)-(d) illustrates the fabrication procedure schematically. The samples were initially cleaned sequentially using with n-butyl acetate, acetone and IPA in order to degrease and remove any unwanted dust particles on the sample. This was done by. The silica particles with a diameter of approximately 1 µm diluted in DI water with 1:50 concentration was then spin-coated on the sample surface at a high rotation speed, and the silica particles serve as micro-masks for subsequent dry etching. In contrast to the previous studies, where a monolayer of close-packed particles was required (see Chapters 4 & 5), microdisk laser fabrication requires a randomly dispersed monolayer of microspheres.

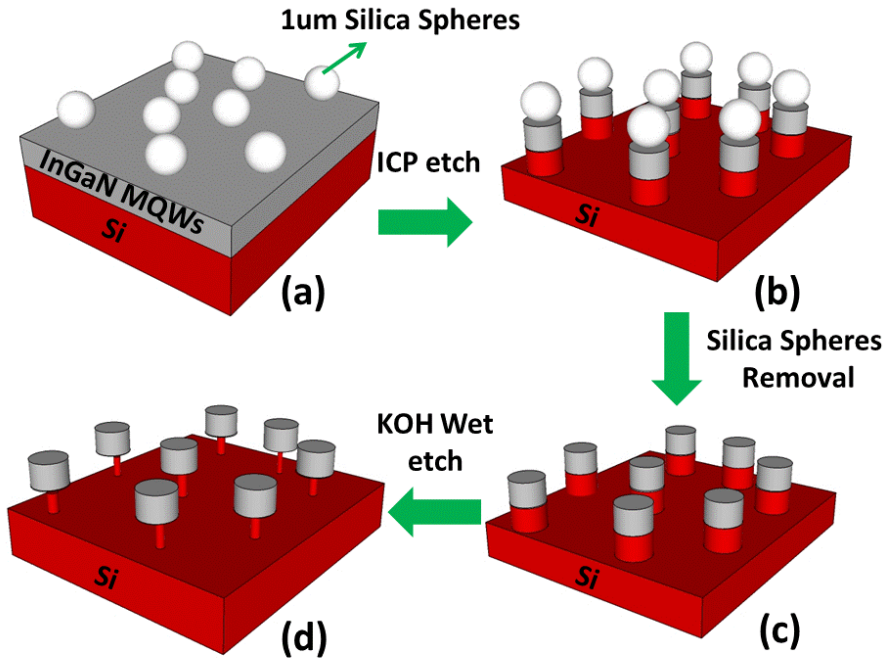

Figure 6.3 (a) - (d) Schematic diagram presenting the fabrication procedure of the microdisk lasers using a microsphere lithography technique.

Increasing the rotation speed to 7000 rpm leads to larger centrifugal forces applied to the silica microspheres, which results in a dispersed monolayer. A standard inductively coupled plasma (ICP) technique was used to etch the InGaN/GaN epi-wafer in order to form sparsely distributed micro pillars. Silica microspheres were then removed from the top of the pillars simply by using an ultrasonic bath. Finally, a KOH wet etching method was then employed to form an undercut structure through introducing an air gap, which isolates the micro-disk region from the silicon substrate. Consequently, a large air-gap (1.2 µm) with a very small post remaining to mechanically support the micro-disk was formed under the micro-disk region, significantly enhancing the optical confinement along the vertical direction and thus minimising any optical losses to the silicon substrate. A further surface treatment involving the utilisation of hot nitric acid has been employed in order to remove the residual etchants and the damage generated during the ICP dry etching process.

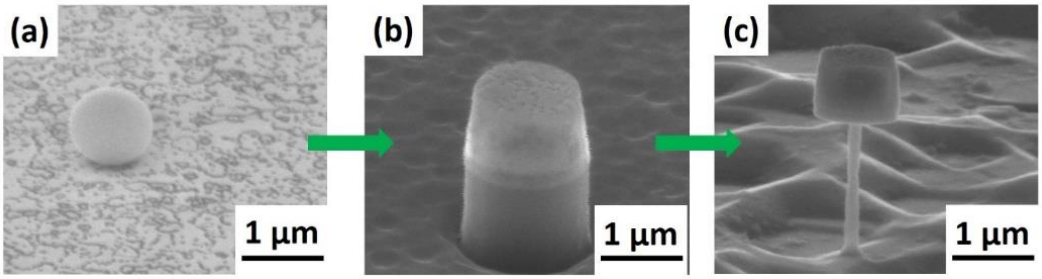

Figure 6.4 (a)-(c) shows the SEM images recorded at each step of the fabrication procedure, which were used to monitor the fabrication procedure.

6.4.1 Undercut Microdisks with KOH

In order to form an undercut structure by introducing an air gap under the microdisk in the silicon substrate, a potassium hydroxide (KOH) wet chemical etching of a 30% concentration at 40^{o}C was employed.

Undercutting the microdisk is the most difficult part of the fabrication process and must be controlled precisely. Therefore an optimisation of the etching time was performed, as Fig. 6.5 (a)–(e) shows, where the etching time is varied from 20 to 100 seconds. In the case of an etching time from 20 to 60 seconds the microdisks were not fully undercut.

Figure 6.5(d) shows a microdisk after an 80 second wet chemical etching that left behind a Si post of approximately 150nm thick, which will mechanically support and isolate the disk region. If the etching time was further increased to 100 seconds, as shown in Fig. 6.5(e) the microdisks fall over on the etched silicon surface. Our optimised etching time is 80 seconds, with an estimated etching rate of approximately 9 nm/second. In addition to undercutting the micro disk the KOH etching also slightly polishes the sidewalls of the microdisk.

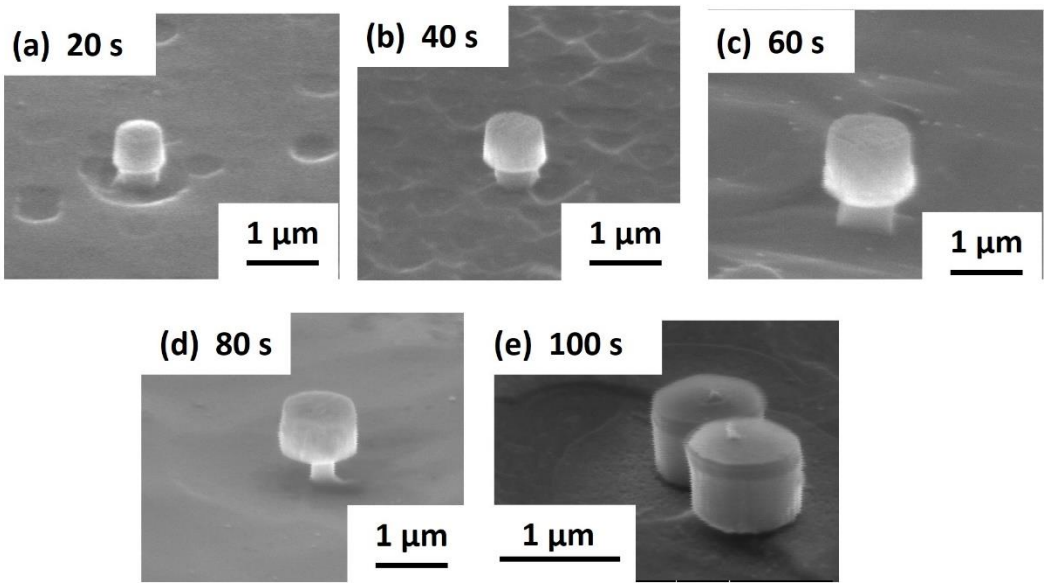

Figure 6.5 (a)-(e) Wet chemical etching times of (a) 20 seconds, (b) 40 seconds, (c) 60 seconds, (d) 80 seconds and (e) 100 seconds.

6.5 Optical Investigation of Microdisk Lasers

6.5.1 Optical Pumping of a Single Microdisk Laser

The optical investigation is completed on the sparsely distributed microdisks, as shown in Fig. 6.6(a)-(c), fabricated using procedure detailed above. The side-view SEM image of Fig. 6.6(a) shows the final structure of a microdisk with a large air gap, introduced during wet chemical etching. The air-gap below the micro-disk is approximately 1.2 µm height, which is much larger than that obtained in the micro-disks fabricated based on GaN-on sapphire, where the extra sacrificial layer with a total thickness of 200 nm is used [9, 10]. The very large air gap is expected to minimise optical losses to the silicon substrate, and thus is expected to significantly enhance optical confinement in the vertical direction [24].

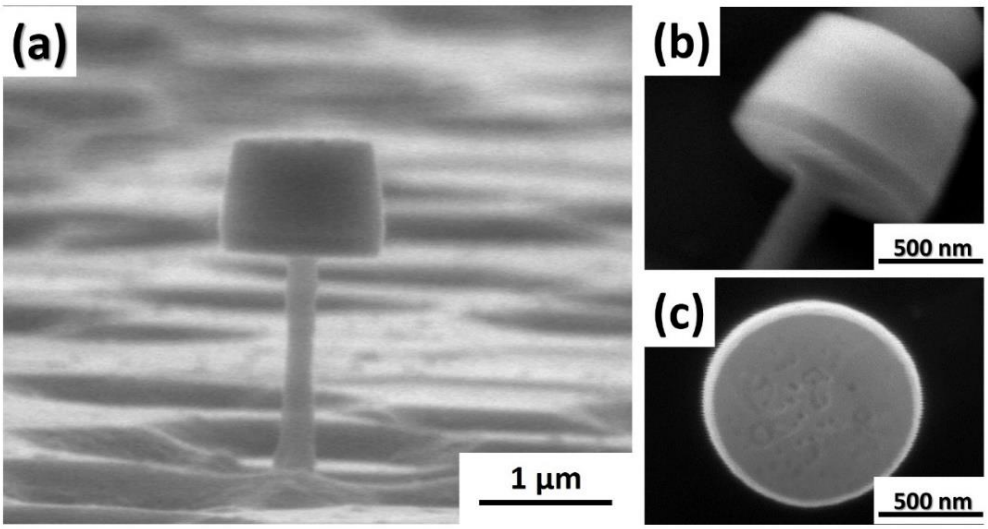

Figure 6.6 (a) side-view SEM image of a single microdisk on a Si substrate; (b) high magnification SEM image revealing smooth sidewalls; and (c) top-view SEM image showing the circular geometry of the cavity.

Figure 6.6(b) shows a SEM image with a high magnification, which shows smooth sidewalls. Smooth sidewalls are crucial to achieving microdisk lasers with excellent performance [9]. Roughness in a microdisks sidewalls results in a leakage of the optical modes, leading to an increase in lasing threshold. To minimise any potential damage or defects (non-radiative recombination centres) generated during the dry etching process a surface treatment process was completed. The process employed involves the use of hot nitric acid for 10 minutes set at 160^{o}C [7]. The purpose of this process is to restore the damage on the InGaN/GaN QWs, which was caused by Ar ion bombardment during the dry etching process. Finally, the top-view SEM image provided in Fig. 6.6(c) shows the excellent circular geometry of the microdisk, with a diameter of around 1 µm.

Figure 6.7(a) shows the typical lasing spectra of our micro-disk laser measured at room temperature as a function of optical pumping power density from 79 W/cm^2 to 25 kW/cm^2, excited using a 375 nm cw diode laser in a micro-PL system.

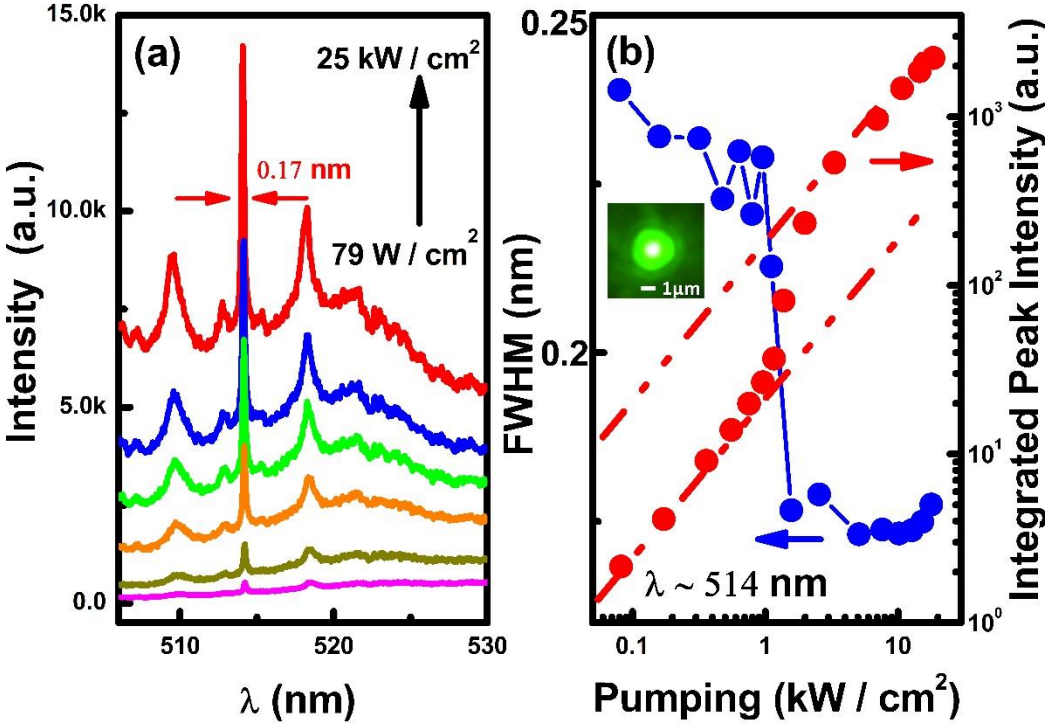

Figure 6.7 (a) Lasing spectra of the microdisk laser recorded as a function of the optical pumping power density at room temperature; (b) light-light curve (on a log-log scale) and FWHM plotted as a function of the optical pumping power density. The inset shows the lasing image of the microdisk, captured above the lasing threshold; and the red dashed-lines are a visual guide only.

This system is equipped with a high resolution camera and a sub-micron resolution positioner, allowing us to identify and address single micro-disks accurately. Under low excitation power, a few weak emission peaks (different WGMs) have been observed. However, when the optical pumping power density is above 1 kW/cm^2, a very sharp and strong emission peak at 514 nm has been observed. The intensity increases dramatically along with a significant reduction in full width at half maximum (FWHM) with further increase in optical pumping power density. The thickness of the microdisk is greater than λ/2n (approximately 600nm), which gives the potential for some weak vertical or hybrid modes, thus other peaks in Fig. 6.7 (a) are observed, which do not indicate of a lasing.

Figure 6.7 (b) shows a light-light (L-L) plot of the lasing mode at 514 nm on a log-log Scale. The L-L curve exhibits an ‘‘s’’ shaped behaviour, a typical fingerprint for lasing [4-7, 25, 26]. The threshold for lasing can be determined from the L-L plot, and is found to be approximately 1 kW/cm^2. Figure 6.7(b) also shows the FWHM of the emission peak as function of the optical pumping power density. This plot exhibits a dramatic reduction in the FWHM with increasing optical pumping power density starting from 1 kW/cm^2, the lasing threshold. The FWHM drops to 0.17 nm from 0.24 nm with an increasing optical pumping power density, and is due to the temporal coherence of the cavity. The quality factor (Q factor) of the cavity is given by (6.1) below.

$$\mathrm{Q} = \frac{\lambda}{\Delta\lambda} \qquad (6.1)$$

Where λ and Δλ is the central emission wavelength and FWHM respectively, below the lasing threshold the Q factor is approximately 2150. The high Q factor achieved could be partially attributed to the enhancement in optical confinement in the vertical direction [10, 20]. This enhancement is a result of the smoothed cavity sidewalls and the improved air gap obtained underneath the microdisk, one of the major benefits to using silicon substrates. This also leads to enhancement in the coupling between the cavity mode and the green emission from the InGaN/GaN MQWs. The inset image of Fig. 6.7(b) shows an image of the lasing from the micro-disk as captured by a CCD camera, where the optical pumping is above the threshold. Further characterisation of the microdisk laser allows the β factor to be determined, which is defined as the fraction of spontaneous emission coupled into the lasing mode. It can be evaluated based on the ratio of the integrated intensity below and above lasing threshold from the L-L curve of Fig. 6.7(b) [20]. The β factor can be obtained by fitting a standard rate equation analysis [27, 28].

$$\mathrm{I(p)} = \mathrm{A} \times \left[\frac{p}{1+p}(1+\zeta)(1+\beta p) - \zeta\beta p\right] \qquad (6.2)$$

$$\mathrm{A} = \frac{\hbar\omega\gamma}{\delta\beta} \qquad (6.3)$$

$$\zeta = \frac{\mathrm{N_0}\beta\mathrm{V}}{\gamma\tau_{\mathrm{sp}}} \qquad (6.4)$$

Where p and I are the photon number and excitation intensity respectively. The scale factor A is given by (6.3), where ω is the mode frequency, γ is the cavity decay rate and δ is the photon conversion efficiency. The dimensionless parameter ζ is given by (6.4), where N_0 is the transparency carrier density of the material, V is the volume of the active region and τ_{sp} is the spontaneous emission lifetime. The rate equation uses the assumption that there is only one mode lasing overlapping with the gain region. Since material parameters like γ and N_0 are unknown, we treat β, ζ and A as fitting parameters, where β and ζ define the overall shape of I (p) and A is the magnitude [25, 26].

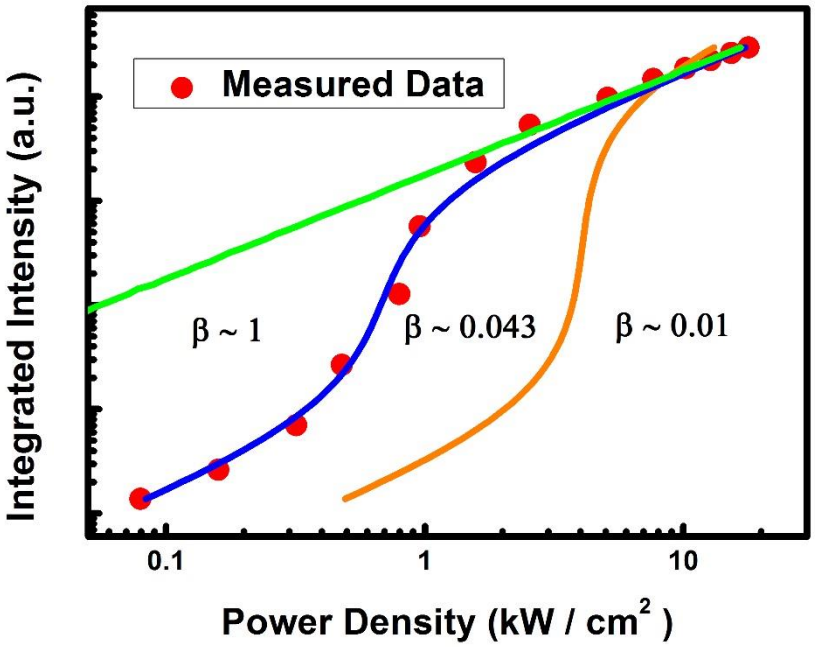

Figure 6.8 Integrated peak intensity against excitation power density; solid lines are the fitting curves based on the rate equation for β equal 0.01, 0.043 and 1.

The characteristic 's-shape' of the curve in the L-L plot defines the three regimes of operation in a laser from spontaneous emission, amplified spontaneous emission and then lasing oscillation. Figure 6.8 shows the fitting which results from using the rate (6.2). It can be seen that for low β values a more pronounced

kink and a higher threshold is observed. As the spontaneous emission factor increases, thresholdless lasers can be achieved, where all of the spontaneous emission is coupled into the lasing mode (green line). For this microdisk laser the β factor was estimated to approximately 0.043 by fitting the experimental results to the rate (6.3).

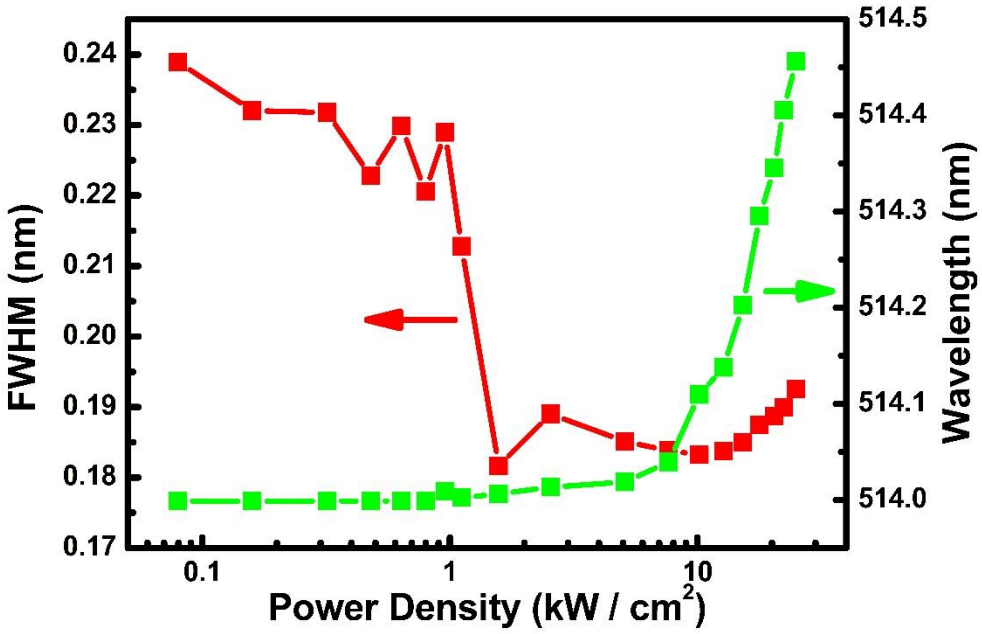

Figure 6.9 Measured peak wavelength and FWHM as a function of optical pumping power density.

Unfortunately, further investigation of the lasing peak reveals that as the excitation power increases above 10 kW/cm^2, a redshift of the lasing peak starts to occur. The reason for this is attributed to the thermal effects of the microdisk region under high excitation power densities. The excitation power density was limited to a maximum 25 kW/cm^2 in order to avoid permanently damaging the microdisk laser.

6.5.2 Recombination Dynamics Investigation

In order to further investigate the lasing oscillation of the microdisk room temperature micro time-resolved PL (μ-TRPL) measurements have been performed. A single microdisk was pumped with a 375 nm pulsed diode laser with a pulse width of 50 ps excitation source. Figure 6.10 shows the μ-TRPL decay traces measured below threshold (0.9 kW/cm^2) and above threshold (4.7 kW/cm^2) to demonstrate the major difference between them. Above the lasing threshold shows the additional and ultra-fast decay component. The initial fast decay component observed in PL decay trace of the microdisk is believed to be a result of a lasing operation.

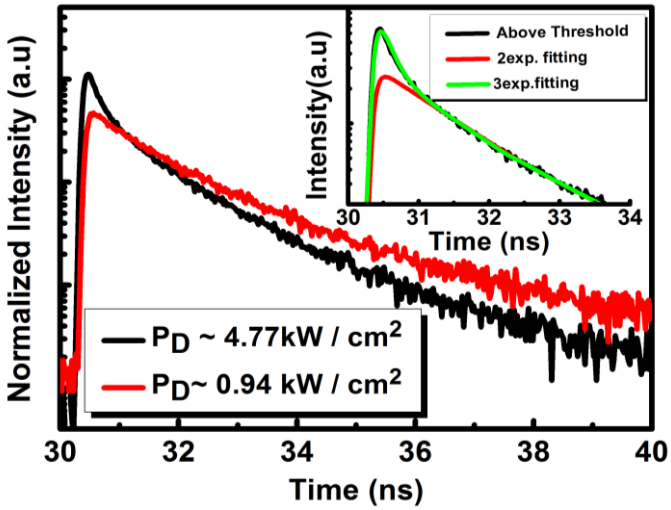

Figure 6.10 (a) room temperature μ-TRPL decay traces of the microdisk laser recoded above and below the threshold; inset plot shows the data-fitting using a bi-exponential and tri-exponential model to aid comparison.

A standard bi-exponential model was used to fit the TRPL decay trace below the threshold [29-31], these TRPL traces [I (t)] can be described by equation 6.5 below.

$$I(t) = A_1 e^{-t/\tau_1} + A_2 e^{-t/\tau_2} \qquad (6.5)$$

Where A_1 and τ_1 are the fast component and A_2 and τ_2 are the slow component. The obtained lifetime of the fast and slow decay components is around 1.0 ns and 2.7ns, respectively.

Remarkably, the bi-exponential model no longer works for the μ-TRPL traces obtained above lasing threshold (4.7 kW/cm^2 as an example for Fig. 6.10). In that case, an extra decay component is required to fit the TRPL trace, adding an extra term (6.5) to give (6.6).

$$I(t) = A_1 e^{-t/\tau_1} + A_2 e^{-t/\tau_2} + A_3 e^{-t/\tau_3} \qquad (6.6)$$

Where A_1 and τ_1 (A_2 and τ_2) remain unchanged from above, and the last term represents the additional ultra-fast component due to the laser action [32, 33]. For comparison, the fitting based on both the bi-exponential model and tri-exponential model have been performed, and are shown in the inset of Figure 6.10. A good fit is obtained using the tri-exponential model (green line), while the bi-exponential model (red line) no longer works. The extra component (τ_3) is extremely fast at approximately 150 ps, which approaches the systems response-time. The lifetimes of τ_1 and τ_2 remain almost completely unchanged and are set at 1.10 ns and 2.72ns respectively. The ultra-fast decay component is due to lasing action [28, 29], providing solid evidence for lasing in the microdisk laser.

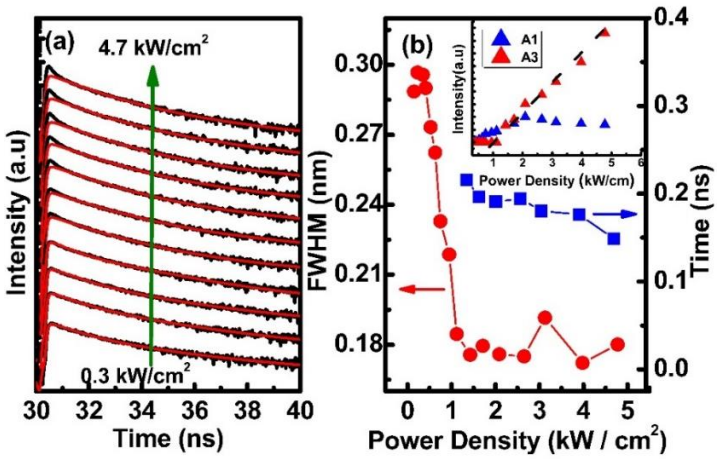

Figure 6.11 (a) dependence of the μ-TRPL decay traces of the microdisk laser on the optical pumping power density, showing evolution from spontaneous emission to lasing; and (b) FWHM of the lasing peak and lifetime of the ultra-fast decay component as a function of optical pumping power density, inset plot shows A_1 and A_3 coefficients as a function of optical pumping power density.

Figure 6.11(a) shows the μ-TRPL traces of the microdisk laser recorded as a function of optical pumping power density from 0.3 kW/cm^2 to 4.7 kW/cm^2. This plot allows observation of the evolution from spontaneous emission to lasing, lasing threshold can also be determined. Figure 6.11(a) clearly shows that the ultra-fast component only appears when the optical pumping power density is above 1 kW/cm^2, the same value obtained from Fig. 6.7(b). In Fig. 6.11(a) the bi-exponential model was deliberately used to fit the TRPL traces (red lines); as it highlights the appearance of the ultra-fast component clearly as it passes the lasing threshold. When the optical pumping power density is below 1 kW/cm^2, the bi-exponential model fits μ-TRPL decay is well, while the ultra-fast component starts to appear and then becomes dominant when the optical pump power density is above 1 kW/cm^2. It becomes even more clear if we plot the FWHM of the lasing peak at 514 nm and the lifetime of the ultra-fast decay component (i.e. τ_3) as a function of optical pumping power density in a same figure, which is Fig. 6.11(b). It is clear that the sudden reduction in the FWHM and the appearance of the ultra-fast component take place simultaneously.

It should be noted that the optical pumping power density dependent FWHM plot shown in Fig. 6.11(b) was obtained using a 375nm pulsed laser optical source. This leads to less significant thermal effects when compared to the use of a 375nm CW diode laser as an optical pumping source as in Fig. 6.7(b). As a result Fig. 6.11(b) is slightly different from the data shown in Fig. 6.7 (b).

The inset of Fig. 6.11(b) provides comparison of the ultra-fast decay component (i.e. lasing part described as A_3 in (6.6) and the standard fast decay component (i.e. spontaneous part described as A_1 in (6.5). As the optical pumping power density exceeds the threshold (1 kW/cm^2), A_3 increases very quickly, supressing A_1. This means that the lasing effects dominate the emission when the optical pumping power density is above the threshold. Please note that for simplicity A_3 is labelled zero below the threshold, as this component does not appear below the threshold.

6.5.3 Spatially-Resolved PL Measurements

Spatially-resolved PL measurements were performed at room temperature using a commercially available confocal PL system, in order to further investigate the microdisk laser. The spatial resolution of the system is approximately 160nm, where a 375nm CW diode laser was used as an excitation source. Figure 6.12(a) shows the lasing spectrum above threshold, where the highlighted areas labelled with blue and red colour represent the on-resonance (i.e. lasing peaks at 514nm) and off-resonance regions, respectively. Figure 6.14(b) shows a typical confocal PL mapped image of the microdisk in off-resonance (i.e. red coloured area), where the boundaries of the microdisks are defined by the white dashed circles. In the case of the off-resonance emission, light is mainly due to spontaneous emission and therefore has random phase.

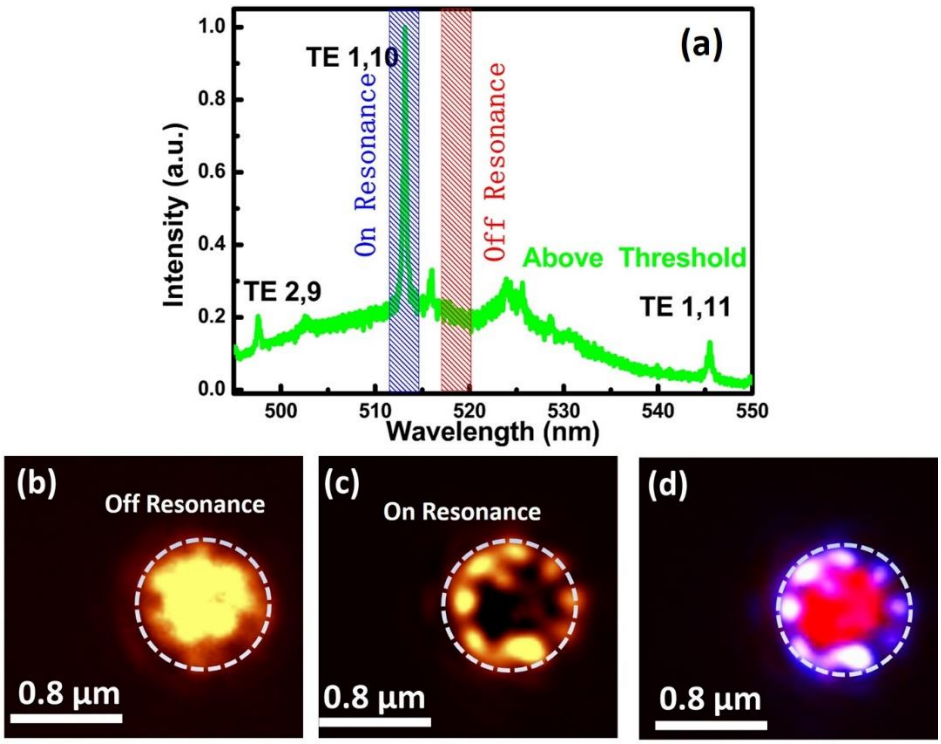

Figure 6.12 (a) Lasing spectrum of the microdisk laser above lasing threshold, blue and red coloured areas respectively highlight regions of on-resonance and off-resonance; (b) typical confocal PL image in off-resonance; (c) typical confocal PL image in on-resonanc e; and (d) overlaid confocal PL maps of on-resonance and off-resonance.

Figure 6.12(c), shows a typical confocal PL image in the on-resonance case, demonstrating that the coherent light circulates the periphery of the microdisk to form clear WGMs [34-38].

The confocal PL images of the off-resonance and on-resonance integrated areas in Fig. 6.12(b) and (c), were overlaid in Fig. 6.12(d). The blue colour shows the on-resonance emission circulating the periphery and the off-resonance emission is coloured red. Off-resonance originates from the spontaneous emission of the QWs at the centre of the microdisk, and is not coupled into the lasing mode. Standard finite-difference time-domain (FDTD) simulations have also been performed to confirm the WGM at 514 nm, agreeing with the observed spectrum of the microdisk. The modes are labelled in Fig. 6.12(a).

6.5.4 Finite-Difference Time-Domain (FDTD) Microdisk Simulation

In order to numerically investigate the microdisk laser and locate and identify the cavity modes, a FDTD simulation was completed, a more detailed discussion is provided in Section 5.4. The simulations were carried out using FDTD Lumerical solutions software.

Figure 6.13(a) shows the experimentally measured microdisk laser spectrum above the lasing threshold (green line) and the simulated FDTD mode spectrum (red line), which are well-matched. This also indicates that there exist three resonance modes at 498 nm, 514 nm and 546 nm. Some variation in the WGMs position can be attributed to a slight variation in the actual microdisk size, where the silica particles size uniformity is ±10%. A diameter of 1 μm and refractive index for GaN of 2.5 are used for our simulation.

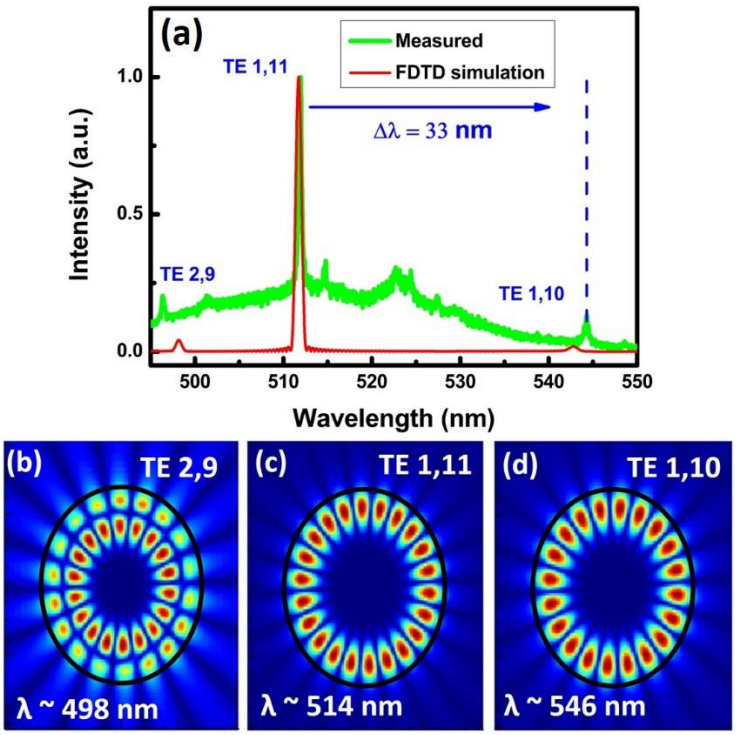

Figure 6.13 (a) Experimental results and simulated FDTD WGM position; TE WGMs profiles are shown in Figures (b)-(d).

From Fig. 6.13(a) the experimental WGM spacing measured is approximately 33nm. The separation of the modes can be calculated using (6.7) below.

$$\Delta\lambda_{WG} = \frac{\lambda_{cav}^2}{2\pi R n_{GaN}} \qquad (6.7)$$

Where λ_{cav} is the WGM wavelength, R the microdisk radius (approximately 500 nm) and η_{GaN} is the refractive index of GaN (2.5). The experimentally observed and theoretically calculated WGM spacing shows a good match at approximately 33 nm. The transverse electric (TE) WGM profiles for the modes at 498 nm, 514 nm and 546 nm are all illustrated in Fig. 6.13 (b)–(d). The red and blue regions represent the highest and the lowest field intensities respectively, where the microdisk boundaries are defined by the black line. According to the FDTD simulations the peak at 498 nm is a second-order mode (n=2) with mode number (m) 9; whereas the peaks at 514 nm and 549 nm belong to a first-order mode family (n=1) with mode numbers of 11 and 10

respectively. Second-order modes circulate nearer to the centre of the disk, consequently they tend to suffer from leakage due to the location of the Si post.

6.5.5 Lasing Threshold Investigation

In the previous sections lasing from an InGaN/GaN MQW microdisk laser in the green spectral region has been presented, with a lasing threshold of approximately 1 kW/cm^2. A large indium mole fraction (29%) was used to achieve lasing in the green spectral region, which resulted in lower quality QWs, due to an increase of the spontaneous piezoelectric fields pulling apart the electron-hole wave functions. Additionally, high indium compositions is obtained by reducing the growth of InGaN/GaN MQWs at a low temperature, increasing number of non-radiative centres for green emitters [39 - 41].

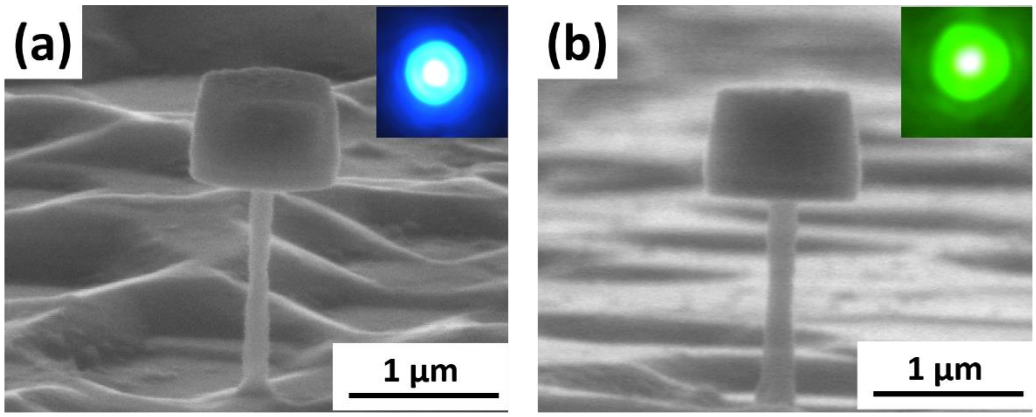

Figure 6.14 (a) Microdisk emitting at 480nm; and (b) Microdisk emitting at 514nm.

Similar to the fabrication of the microdisk lasing in the green spectra region detailed earlier in this chapter, microdisk were fabricated in order to achieve a blue lasing at 480 nm. Figure 6.14(a)-(b) shows the SEM images of the fabricated microdisks for both blue and green lasing. The insets show the images of the emission from the microdisk under optical pumping during lasing oscillation, captured using a CCD image camera.

The lasing threshold for the blue lasing is approximately 300 W/cm^2, as shown in Fig. 6.15, while the threshold for the green at 514nm is 1 kW/cm^2.

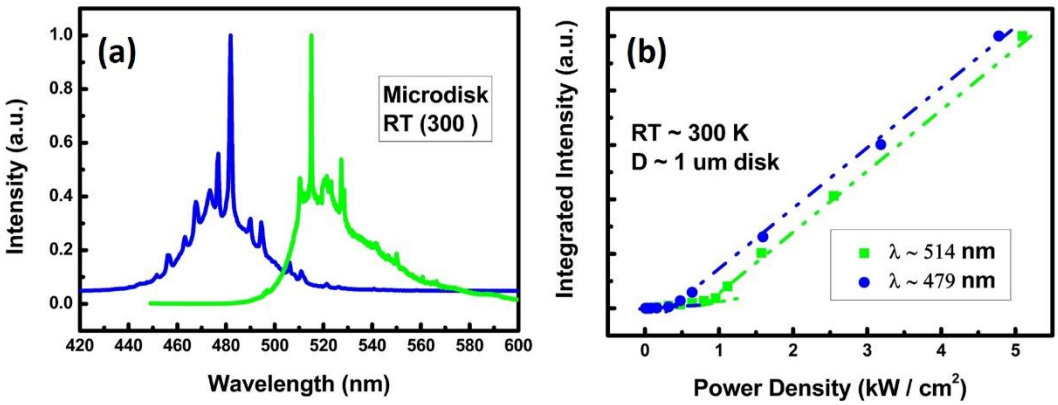

Figure 6.15 (a) PL emission of the microdisk lasers at different emission wavelengths, operating above lasing threshold; and (b) integrated Pl intensity plotted as a function of optical pumping power density on a linear scale.

6.6 Conclusion

In summary, room temperature green lasing has been achieved, with an ultra-low lasing threshold, from InGaN/GaN MQW microdisk lasers with an undercut structure using a silicon substrate. The devices were fabricated by means of a cost-effective microsphere lithography approach with subsequent dry and chemical etching steps. The optically pumped lasing at 514 nm has been achieved using a CW diode laser source, where the lasing threshold has been found to be as low as approximately 1kW/cm^2. Optical pumping power dependent measurements have confirmed this lasing action. Further evidence includes micro time-resolved PL measurements, which demonstrate an ultrafast decay component with a lifetime of approximately 150 ps, due to the lasing action when the optical pumping power density is above the threshold. This result is in agreement with the optical pumping power dependent measurements. Confocal PL mapping measurements have also been performed, which demonstrate a clear coupling of the coherent light with the WGM.

Furthermore, the dependence of the lasing threshold with the indium mole fraction for the InGaN/GaN MQWs was investigated. A reduction in lasing threshold operation at 480 nm with a 300 W/cm^2 lasing threshold was found. The

lasing operation for both microdisk lasers, at 480 nm and 514 nm were confirmed via power dependent and time-resolved measurements. The reduction of the lasing threshold with reducing indium mole fraction is a result of the decrease in the current density required to reach transparency conditions and also the potentially lower inhomogeneity of the InGaN QWs.

References

[1] G. Shambat *et.al., Nat. Commun.* vol. **2**, p. 539 (2011).

[2] Y. K. Jeong *et.al., Nat. Commun.* vol. **4**, p. 2822 (2013).

[3] M. Noginov *et.al., Nature,* vol. **460**, p. 1110 (2009).

[4] R. F. Oulton *et al., Nature,* vol. **461**, p. 629 (2009).

[5] R. M. Ma *et.al, Nat. Mater.* vol. **10**, p. 110 (2011).

[6] Y. J. Lu *et al., Science* vol. **337**, p. 450 (2012).

[7] Y. Hou, P. Renwick, B. Liu, J. Bai and T. Wang, *Sci.Rep.* vol. **4**, p. 5014 (2014).

[8] Y. H. Kim, *Nature,* vol. **3**, p. 1123 (2012).

[9] C. Adele *et.al., Nat. Photon.* vol. **1**, p. 61 (2007).

[10] I. Aharonovich *et al., Appl. Phys.Lett.* vol. **103**, p. 021112 (2013).

[11] K. J. Vahal, *Natrure* vol. **424**, p. 839 (2003).

[12] H. W. Choi *et al., Appl. Phys. Lett.* vol. **89**, p. 211101 (2006).

[13] K. Lee *et al., Phys. Stat. Sol. (c)* vol. **5**, p. 2063 (2008).

[14] K. Biswas and S. Kal, *Microelectron. J.* vol. **37**, p. 519 (2006).

[15] J. Zavada *et al.,Solid State Electron.* vol. **41**, p. 353 (1997).

[16] E. D. Haberer *et al., Appl. Phys. Lett.* vol. **85**, p. 5179 (2004).

[17] H. W. Choi *et al., Appl. Phys. Lett.* vol. **89**, p. 211101 (2006).

[18] Y. Zhang, Z. Ma, X. Zhang, T. Wang and H. W. Choi, *Appl. Phys. Lett.* vol. **104**, p. 221106 (2014).

[19] J. Bai, T. Wang, P. J. Parbrook and A. G. Cullis, *Appl. Phys. Lett.* vol. **89**, p. 131925 (2006).

[20] T. Wang, J. Bai, P. J. Parbrook and A. G. Cullis, *Appl. Phys. Lett.* vol. **87**, p. 151906 (2005).

[21] J. Bai, T. Wang, P. Comming, P. J. Parbrook, J. P. R. David and A. G. Cullis, *J. Appl. Phys.* vol. **99**, p. 023513 (2006).

[22] M. Athanasiou, T. K. Kim, R. Smith and T. Wang, *Appl. Phys. Lett.* vol. **102**, p. 191108 (2013).

[23] T. Kim, B. Liu, R. Smith, M. Athanasiou, Y. Gong and T. Wang, *Appl. Phys. Lett.* vol. **104**, p. 161108 (2014).

[24] C. F. Wang *et al., Appl. Phys. Lett.* vol. **90**, p. 08110 (2007).

[25] X. Liu *et al., Appl. Phys. Lett.* vol. **84**, p. 2488 (2004).

[26] S. Reitzenstein *et al., Appl. Phys. Lett.* vol. **89**, p. 051107 (2006).

[27] W. H. Wang *et al., Phys. Rev. (B)* vol. **71**, p. 155306 (2005).

[28] S. Reitzenstein *et al., Appl. Phys. Lett.* vol. **89**, p. 051107 (2006).

[29] S. Chichibu *et al., Phys. Stat. Sol. (b)* vol. **234**, p. 746 (2002).

[30] B. Liu, R. Smith, J. Bai, Y. Gong and T. Wang, *Appl. Phys. Lett.* vol. **103**, p. 101108 (2013).

[31] R. Smith, B. Liu, J. Bai and T. Wang, *Nano. Lett.* vol. **13**, p. 3042 (2013).

[32] S. Christopoulos *et al., Phys. Rev. Lett.* vol. **98**, p. 126405 (2007).

[33] K. J. Luo *et al., Appl. Phys. Lett.* vol. **77**, p. 2304 (2000).

[34] V. Zwiller *et al., J. Appl. Phys.* vol. **93**, p. 2307 (2003).

[35] A. W. Schell *et al., Sci. Rep.* vol. **3**, p. 1577 (2013).

[36] S. S. Kim, Y. J. Kim, G. C. Yi and H. Cheong, *Appl. Phys. Lett.* vol. **106**, p. 094310 (2009).

[37] S. Imamura, R. Watahiki, R. Miura, T. Shimada and Y. K. Kato, *Appl.Phys. Lett.* vol. **102**, p. 161102 (2013).

[38] T. J. Kippenberg, A. L. Tchebotareva, J. Kalkman, A. Polman and K. J. Vahala, *Phys. Rev. Lett.* vol. **103**, p. 027406 (2009).

[39] J. W. Raring *et al., Appl. Phys. Expr.* vol. **3**, p. 112101 (2010).

[40] H. Morkoç, *Handbook of Nitride Semiconductors and Devices, GaN-based Optical and Electronic Devices,* 1st ed. (John Willey & Sons, 2009).

[41] J. Zhang and N. Tansu, *IEEE Photon. J.* vol. **5**, p. 2600111 (2013).

[42] Y. Zhang, Z. Ma, X. Zhang, T. Wang and H. W. Choi, *Appl. Phys. Lett.* vol. **104**, p. 221106 (2014).

[43] T. Y. Seong, J. Han, H. Amano and H. Morkoc, *III-Nitride Based Light Emitting Diodes and Applications* (Springer Science & Business Media, 2013).

[44] Q. Wang and T. P. Lee, *Proc. SPIE,* vol. **4580**, p. 179 (2001).

[45] M. Zhang, A. Banerjee, C. S. Lee, J. M. Hinckley and P. Bhattacharya, *Appl. Phys. Lett.* vol. **98**, p. 221104 (2011).

Chapter 7

Conclusions and Future Work

7.1 Conclusion

This thesis presents work on controlling optical interactions in InGaN based MQWs heterostructures, by the post fabrication of nano- and micro- structures. A nanospheres lithography technique was optimised and used for the fabrication of these structures. Nanostructures can enhance the optical performance of the devices, leading to new physics concepts and development of fabrication technologies for future advanced III-nitride optoelectronics.

7.1.1 Fabrication of two-dimensional InGaN/GaN photonic crystal structure using a modified nanosphere lithography technique

Fabrication of two-dimensional photonic crystal structures of nanoholes arrays has been achieved, by means of combining a cost effective nanosphere lithography technique and a novel lift off process. The suppression of the spontaneous emission by the inhibition of propagation in the slab modes was observed through an introduction of photonic crystal structure, leading to significant enhancement in quantum efficiency. The excitonic recombination dynamics were investigated by time-resolved measurements, showing a reduction in spontaneous emission rate as a result of the photonic crystal effect. Angular dependent measurements were performed, showing a clear redirection

of the emission along the vertical direction, further confirming the photonic crystal effect.

7.1.2 Coherent nanocavity structures for enhancement in internal quantum efficiency of III-nitride multiple quantum wells

A significant enhancement in optical performance has been achieved through the introduction of a nanocavity effect based on an InGaN / GaN MQWs emitting in the green spectral region. Three dimensional FDTD simulations have been used to design the nanocavity structure. A series of samples were fabricated by a nanosphere lithography technique based on the designs. PL measurements showed sudden increase the PL intensity for the nano array disk with a diameter of 205 nm. The increase in spontaneous emission rate was also confirmed. Additionally, a significant enhancement of the internal quantum efficiency of the sample with a diameter 205 nm.

7.1.3 Room temperature continuous-wave green lasing from an InGaN microdisk on silicon

A room temperature lasing in the green spectral region was achieved by the fabrication of a micro-disk on an InGaN / GaN MQWs sample grown on Si substrate. A clear lasing at 514 nm has been observed with a lasing threshold of approximately 1 kW/cm^2, with a Q-factor of 2150. Excition power density dependent time-resolved PL measurements show an appearance of ultrafast component above the threshold. Spatially resolved measurements were performed on a single micro-disk, further confirming the lasing operation of our microdisk laser.

7.2 Future Work

7.2.1 Fabrication of Hybrid LEDs for white light emission and for ultrafast communication purposes

Hybrid III-nitrides/organic devices, drawing together the major advantages from the two kinds of semiconductors, are becoming more interesting recently. Guha et al. (1997) reported the first hybrid organic–inorganic emitter, where a blue InGaN led device, emitting at 460 nm was used to pump the DCM dye [4], resulting in colour conversion with high CRI.

The coupling mechanism between organic and inorganic semiconductors is due to the non-radiative Föster resonant transfer (FRET). In such a dipole-dipole interaction which consists of a donor (InGaN QWs) and an acceptor dipole (inorganic semiconductor) the distance between the two dipoles and the absorption spectrum overlap of the organic and inorganic semiconductor are the parameters that affect the energy transfer efficiency [5]. Due to the nature of near field effect, the critical separation between dipole needs to be less than 10 nm in order to achieve the non-radiative energy transfer efficiently. For a standard InGaN based LED structure, a thick 200 nm p-type layer is required to grown on top of the QWs, thus restricting any energy transfer due to the large separation between the two dipoles.

A novel approach, has been developed at Sheffield leading to successful fabrication of a hybrid III-nitride nanostructure/organic structure efficient, where InGaN based nanorods fabricated by the self-organised nickel mask approach was surrounded by an yellow F8BT polymer [6]. The F8BT polymer was chosen to be as the acceptor dipole, as its absorption spectrum overlaps with the emission spectrum of the donor dipole (InGaN QWs) and has a broad emission spectrum with the peak at 560 nm. Mixture of the emission from the two materials could result in white light emission with high CRI due to broad spectrum of the F8BT polymer. The use of nanorod structures enables the high non-radiative energy

transfer efficiency, as the distance between the donor and acceptor dipoles is minimized. By using a structure directly injected hybrid devices may be fabricated. Furthermore, fabrication of a nano-rod structure would result in high efficiency InGaN quantum wells due to strain relaxation [7] and an increase of the extraction efficiency due to wave guiding effects [8].

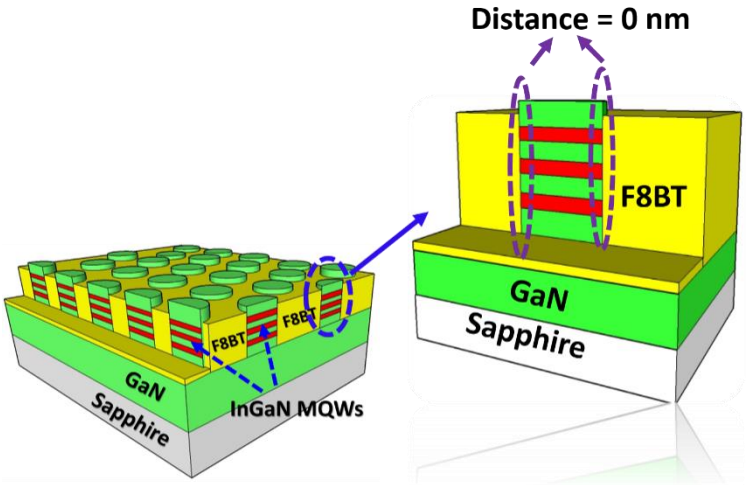

Figure 7.1 Schematic diagram of a nano-rod Hybrid LED fabricated by nanosphere lithography with F8BT polymer deposited in-between.

Fabrication of periodic arrays of nanorods by using the nanosphere lithography technique as schematically illustrated in Fig. 7.1 could result in the accurate control of nanorods size and so the DoS can be enhanced through a proper design. The combination of a nanorod array with a photonic crystal effect and the F8BT polymer is expected to result in the fabrication of high efficiency white light emitters, with ultra-fast response for communication purposes.

7.2.2 Photonic crystal cavity

The enhancement of spontaneous emission can be significantly increased by decreasing the mode volume because as the Purcell enhancement is directly proportional to the ratio of Q-factor to mode volume ($\propto \frac{Q}{V_{mod}}$). A schematic fabrication procedure for a PhC cavity laser is illustrated in Fig. 7.2 (a) – (h).

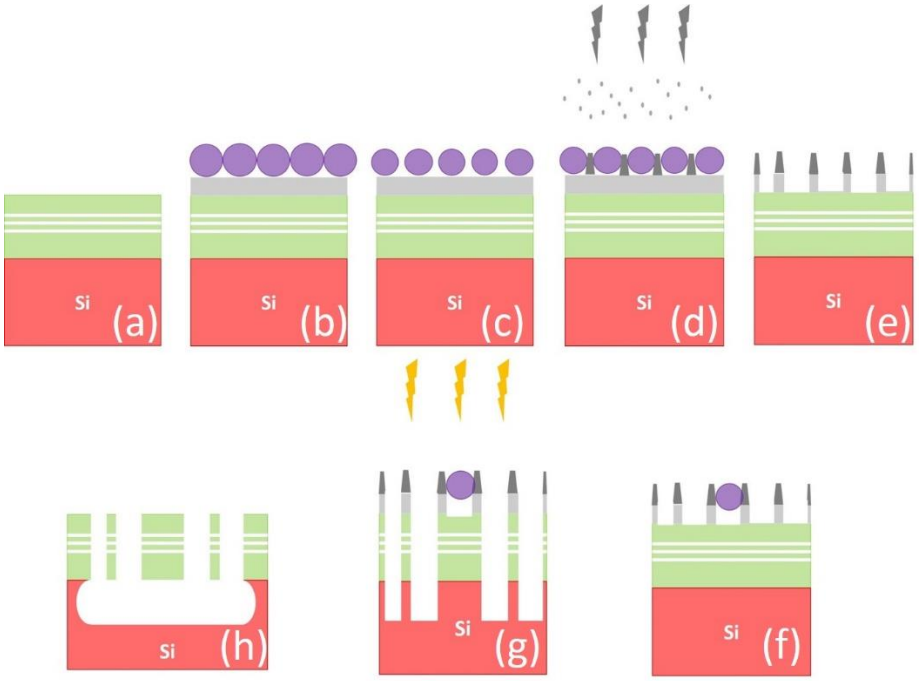

Figure 7.2 Schematic fabrication procedure for PhC cavity laser on Si substrate.

In order to fabricate the PhC cavity, a silicon dioxide layer is deposited prior the silica nanosphere deposition. The size of the spheres can then be refined by RIE etching and a Ni metal mask can be deposited on top of the spheres. The RIE dry etching can then etch through the silicon dioxide and reach the InGaN /GaN MQWs surface. A second deposition of a diluted silica particles will be then deposited on top of the silicon dioxide nanohole mask in order to form randomly spaced defect particles. The randomly spaced particles will be then used to form a cavity and protect the area underneath it. Inductively coupled plasma etching will be employed to etch through the InGaN /GaN QWs and Si substrate. Finally, the membrane can be released by immersing the sample into a tank of hydrofluoric acid (HF).

References

[1] M. Athanasiou, T. K. Kim, B. Liu, R. Smith and T. Wang, *Appl. Phys. Lett.* vol. **102,** p. 191108 (2013).

[2] T. Kim, B. Liu, R. Smith, M. Athanasiou, Y. Gong and T. Wang, *Appl. Phys. Lett.* vol. **104**, p. 161108 (2014).

[3] M. Athanasiou, R. Smith, B. Liu and T. Wang, *Sci. Rep.* vol. **4**, p. 7250 (2014).

[4] S. Guha, R. A. Haight, N. A. Bojarczuk and D. W. Kisker, *J. Appl. Phys.* vol. **82**, p. 4126 (1997).

[5] G. Heliotis *et al., Adv. Matt.* vol. **18**, p. 334 (2006).

[6] R. Smith, B. Liu, J. Bai and T. Wang, *Nano. Lett.* vol. **13**, p. 3042 (2013).

[7] Q. Wang, J. Bai, Y. P. Gong and T. Wang, *J. Phys D: App. Phys.* vol. **44**, p. 395102 (2011).

[8] S. H.Kim *et.al., Opt. Expr.* vol. **21**, p. 7125 (2013).